H_3^+ in the Jovian planets.

Monitoring the Jovian Ionosphere Using H_3^+ Emission as a Probe.

by

Hoanh An Lam

A thesis submitted to the

UNIVERSITY OF LONDON

for the degree of

DOCTOR OF PHILOSOPHY

University College London 14th August 1995

ProQuest Number: 10017792

All rights reserved

INFORMATION TO ALL USERS
The quality of this reproduction is dependent upon the quality of the copy submitted.

In the unlikely event that the author did not send a complete manuscript
and there are missing pages, these will be noted. Also, if material had to be removed,
a note will indicate the deletion.

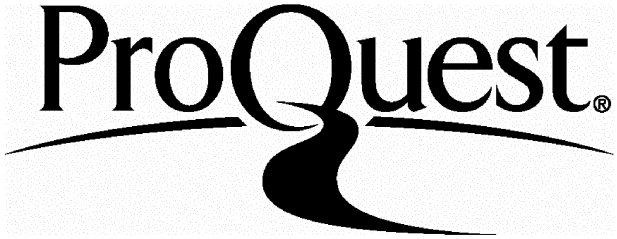

ProQuest 10017792

Published by ProQuest LLC(2016). Copyright of the Dissertation is held by the Author.

All rights reserved.
This work is protected against unauthorized copying under Title 17, United States Code.
Microform Edition © ProQuest LLC.

ProQuest LLC
789 East Eisenhower Parkway
P.O. Box 1346
Ann Arbor, MI 48106-1346

Abstract

Jupiter has long been a subject of fascination and curiosity. Recently it has become the focus of numerous studies first with ground-based telescopes and then of unmaned spacecraft, notably the **Pioneers** and **Voyagers** series. The discovery of the ionic species H_3^+ on Jupiter presented the scientific community with an important tool for probing and studying the jovian ionosphere. Earth based observations have answered some questions but raised a number of others concerning the production and maintenance of the jovian ionosphere.

Infrared images of Jupiter were taken and analysed for morphology and distribution of H_3^+. Auroral emission was discovered to have a well defined structure and found to be fairly stable over a long period of time. The main area of emission was found to be located at the footprints of high L-shells, possibly above L-shell = 30 (Connerney's O_6 magnetic field model 1991, 1993). The northern H_3^+ emission appears to occur in a large patch around $\lambda_{III} = 150^o$ and in a series of bright spots forming a possible oval. In the south the emission seems more diffuse with none of the bright spots similar to those observed in the north. The emission appears to come from an oval, but due to the geometry of the southern aurora it is hard to say whether this is true or not.

Spectra of Jupiter taken at wavelengths sensitive to H_3^+ emissions are presented in this study. Results of fitting a theoretical H_3^+ spectrum to the data are reported. H_3^+ emission was found to originate from the whole disk of Jupiter on the dayside. Mapping the H_3^+ emission onto a longitude, latitude grid shows that the results agrees with the imaging work. The low latitude emission is found to correlate closely with the magnetic field dip angles as predicted by Connerney's O_6 model (1991, 1993).

Contents

List of Figures

List of Tables

Acknowledgements

I would like to begin by thanking my supervisors, Steven Miller and Jonathan Tennyson, who have given me encouragement and support throughout my time with the group. Their readings and discussions have made my thesis far better than I can accomplish alone.

My thanks also to all the people in group C for their help and encouragements, especially Nicholas Achilleos for his advice and discussions. They have given me a better understanding of the concepts and processes involved in the subject.

I would like to express my thanks to Gilda Ballester, Bob Joseph, Tom Geballe, Jack McConnel and Renée Prangé whose advice on a number of topics have been very welcomed indeed.

I'm grateful to SERC/PPARC for a studentship and grants to attend conferences and go observing as part of my studies.

For most of the time during my study Tina Rehm gave me her whole support and encouragement for which I'm forever indebted. I'm sorry that things did not turn out the way she expected.

I'm enormously grateful to my parents who have supported me both financially and with their encouragements when I most needed them.

Finally, I would like to thank the Linden Gardens Mob and the Clanricarde Trio for putting up with me when no one else would, Maurette Cahill for putting a bit of light chaos into the project and Vito Graffagnino who not only understands the words "dress" and "sense" in that order, but whose inane banter has kept me from going insane all these years.

Chapter 1

Introduction

1.1 Laboratory Measurements of H_3^+

In his "Further Experiment on Positive Rays" J. J. Thomson (1912) reported discovering an ion with a mass to charge ratio of 3:1. After considering other possibilities he concluded that the molecule formed from three hydrogen atoms. But theory at the time could not account for such a system being chemically bound and Thomson was consequently persuaded that the ion was a deuterated hydrogen molecule. The existence of H_3^+ was only accepted when Hirschfelder (1938) finally showed that the molecule was stable and strongly bound.

H_3^+ is the simplest, stable polyatomic system. Its equilateral triangle configuration at equilibrium means that it does not have a pure rotational spectrum. Theoretical considerations also showed that H_3^+ does not have any stable excited electronic state (apart from a triplet state close to its second dissociation limit). Thus, H_3^+ spectrum would only be observed spectroscopically in the infrared (I.R.), through its doubly degenerate ν_2 bending mode (the ν_1 symmetric stretch mode is Raman active only).

The search for the infrared spectrum of H_3^+ was initiated by Herzberg in 1967 but its discovery in 1980 by Oka had to wait for the high sensitivity of laser spectroscopy. Although many more lines have since been recorded and assigned, progress has been relatively slow due to the "floppy" nature of the molecule. This "floppiness" means that

the spectral lines of H_3^+ are spaced unevenly, making it difficult to predict new transitions from the positions of known lines.

Right from the start, the detection and interpretation of the H_3^+ spectrum was made possible by basic theoretical calculations, beginning with the remarkable work of Hirschfelder (1938). The introduction of computers (Christoffersen *et al* 1964) into the process was a great step forward. Calculations by Carney and Porter (1974, 1976) resulted in the first relatively accurate prediction of the ro-vibrational spectrum of the ion. The electronic surfaces calculated by Meyer, Botschwina and Burton (1986) were used in spectroscopic calculations to achieve very high accuracy (Miller and Tennyson 1989, 1988). This led directly to the identification of the molecule outside of the laboratory. The latest theoretical calculations demonstrate the remarkable advances made in this field, now showing that the largest error in the calculation of transition frequencies is due to the Born–Oppenheimer approximation (Dinelli *et al* 1994, and review by Tennyson 1995).

In astrophysics H_3^+ has a key role in interstellar chemistry. It is formed through the ionisation of molecular hydrogen and then the rapid reaction:

$$H_2^+ + H_2 \longrightarrow H_3^+ + H \tag{1.1}$$

Normally very reactive the molecule is destroyed in the interstellar medium through dissociative recombination:

$$\begin{aligned} H_3^+ + e &\longrightarrow H_2 + H \\ &\longrightarrow H + H + H \end{aligned} \tag{1.2}$$

and the reaction:

$$H_3^+ + X \longrightarrow HX^+ + H_2 \tag{1.3}$$

which is extremely efficient for chemical species whose proton affinities are greater than those of H_2 (Flower 1990).

H_3^+ has a major role in the gas phase interstellar chemistry as well as hydrogen plasma (Lequeux and Roueff 1991). In the cold, hostile environment of the interstellar medium, H_3^+ acts as a protonating agent, via reaction 1.3, explaining the observed abundances of molecular species.

Prior to 1988 attempts to detect H_3^+ concentrated solely on the interstellar medium, in particular the Orion and Taurus molecular clouds where H_3^+ is believed to occupy a key role in the gas chemistry. Because of the low temperature in the interstellar environment, efforts were focussed wholly on searching for the H_3^+ absorption spectrum. To date, however, no positive identification of the ion has been made (Oka 1981, Geballe and Oka 1989, Black *et al* 1990).

1.1.1 Extra–Terrestrial Detection of H_3^+

The ionosphere of Jupiter had been considered by numerous workers as a possible source of the ion (Atreya *et al* 1974, Hunten 1969). Atreya and Donahue (1976) proposed a model of the jovian atmosphere where concentrations of H_3^+ reached 10^3 cm^{-3} in a thin layer (<50 km) close to the homopause.

The Low Energy Charged Particle experiment on board Voyager did detect an ion with a mass to charge ration of 3:1 in the jovian magnetosphere (Hamilton *et al* 1980). These authors suggested that the jovian ionosphere could be a significant source of the H_3^+molecule. McConnell and Majeed (1987) modelled the jovian ionosphere controlled by solar EUV and found H_3^+ concentration as high as 10^4 cm^{-3} around 1000 km above the ammonia cloud tops.

The first remote identification of H_3^+ outside the laboratory was made by Drossart *et al* in 1989. They were attempting to observe the quadrupole spectrum of molecular hydrogen on Jupiter. These transitions, occurring around 2μm, are intrinsically weak; H_2 Einstein A_{if} values are typically 10^{-7} s^{-1}. However column densities of H_2 in Jupiter are about 10^{21}—10^{22} cm^{-2}; large enough to make spectroscopic observations feasible. The attempt was successful. But Drossart *et al* (1989) also found a number of lines which were even more intense than the quadrupole transitions they were looking for. Trafton *et al* (1989) had earlier reported the same unassigned lines, although at much lower resolution.

The eventual identification of the lines as the overtone ($2\nu_2(l = 2) \rightarrow 0$) transitions of H_3^+ owed at least as much to highly accurate quantum calculations (Miller and Tennyson 1989) as it did to laboratory spectroscopy and the development of high resolution

instruments in astronomy.

1.2 Jupiter

1.2.1 Planetary Structure

The largest planetary body in the solar system is composed mainly of hydrogen and helium in solar proportion (He/H$\sim$0.11). Gravitational soundings, observing the orbits of Jupiter's moons and spacecraft trajectories have enabled theorist to construct a model of the planet.

According to Smoluchowski (1976), the center of the planet may be a rocky core of heavy material about the size of the Earth. Surrounding the core is a mantle of hydrogen and helium mixture, which is either solid or liquid at the base and gaseous at the top. The helium may be distributed to provide the non–homogeneity required in order to account for the observed gravitational field. Motions of satellites are strongly affected by the density gradient in the outside few percent of the planet's radius, consequently the structure in this region is better known than deeper in.

Heat balance indicates that Jupiter is emitting more than twice the energy it receives from the Sun. This implies a high central temperature of 20000 K or more and the planet being nearly all liquid or fluid. Internal heat transport is therefore, dominated by convection.

High conductivity and low viscosity associated with the metallic interior enables the operation of a hydromagnetic dynamo to take place. This is driven by planetary rotation and thermal convection which in turn, generates the huge magnetic field observed around Jupiter.

1.2.2 Atmosphere

Jupiter's atmosphere is fascinating in terms of visual appearance and dynamics. Consequently, a large body of work already exists on the subject. For a comprehensive view of the topic the reader is referred to various chapters in "Jupiter" edited by Gehrels (1976).

Here, we will give a brief summary of the compositions and temperature profiles of the atmosphere and ionosphere.

Jupiter's visual appearance is dominated by clouds and their motions. Quantitative description is difficult however and their compositions is usually determined through theory (Atreya 1986, Chamberlain and Hunten 1987). The atmosphere is mostly H_2 with about 10% He. The visible cloud layer is composed of solid NH_3, with additional NH_4SH and H_2O layers at pressures of 3 and 5-7 bars respectively. There is evidence for the existence of CO, PH_3, GeH_4 and HCN (Drossart *et al* 1982, Lellouch *et al* 1984). The colouring material of the clouds have been much speculated about and ranges from organic matters to red phosphorus, but as yet there is still no observational identification of the colourants.

The atmospheric thermal profile can be seen in figure 1.1 (taken from Hunten 1976). At the 1 bar pressure level the temperature is 170 K and decreases going up through the troposphere to a minimum of 100 K at the tropopause (0.1 bar). The temperature then increases throughout the stratosphere, leveling out at the stratopause. Temperature remains constant in the mesosphere up to the mesopause, conventionally defined as the base of the thermosphere. From here on the temperature increases rapidly to 850 K at pressure of 10^{-3} μbar.

Height measurements of atmospheric structures are made with respect to some arbitrary level since Jupiter has no surface. The usual practice is to either locate the feature on a pressure scale or to specify the height with respect to some pressure level such as the H_2O cloud base (5-7 bar), ammonia cloud tops (1 bar), 1 mbar and 1 μbar.

Results from Pioneer 10 and 11 radio occultation measurements showed that the electron density profile in Jupiter's ionosphere has up to seven peaks. A model by Atreya and Donahue (1976) indicated that the ionosphere is dominated by protons. However, in a thin layer (<50 km) close to the homopause, concentration of the H_3^+ ion can reach up to 10^3 cm^{-3} and become the dominant species.

Kim and Fox (1991) modelling the ionospheric E region, found two strong solar lines penetrating below the methane homopause to ionise the hydrocarbons (mostly C_2H_2). The ionised hydrocarbon peak concentration was found to be in excess of 10^4 cm^{-3} and

Figure 1.1: Thermal profile of Jupiter's atmosphere (taken from Hunten 1976). For levels deeper than 1 bar, the ideal-gas adiabat is represented by the formula shown.

located around 320 km above the ammonia cloud tops. Hydrocarbon ions are quickly converted to more complex species through reactions with CH_4, C_2H_2, C_2H_4 and C_2H_6.

The ionospheric temperature of Jupiter is high. Radio occultation data from the Pioneer 11 encounter indicated a plasma temperature of 850±100 K. Atreya (1986) proposed particle precipitation and Joule heating as the most likely mechanisms to account for the heat source. However, both particle precipitation and Joule heating are localised at the auroral regions. An efficient convection system is therefore needed to distribute the energy deposited at the aurorae to regions throughout the ionosphere.

The collision of the comet Shoemaker–Levy/9 with Jupiter in the summer of July 1994 presented a unique opportunity to witness an event of unparallel magnitude in the solar system. It prompted a huge international effort, both to observe and model the consequences that arise when a large comet or asteroid collide with a planetary body. An enormous amount of work was carried out to monitor the effects on Jupiter due to the impact. In particular, a modelling effort by Abouelainine, Mangeney and Drossart (1995) demonstrated that horizontal circulation combined with vertical convection can be very efficient at distributing the energy of the impact throughout the atmosphere. However, it is not known whether large scale vertical motions exist in the thermosphere and above. Nevertheless this gives a hint about the mechanism required for energy deposited in the auroral region to be transported to lower latitudes in the ionosphere.

1.2.3 Jovian Magnetosphere

The first clue to the existence of a magnetic field on Jupiter came with the detection of low-frequency radio emission by Burke and Franklin (1955). At the time Jupiter was considered to be a giant sphere of gas surrounded only by space. Ground–base monitoring of non–thermal radio emissions yielded basic characteristics of the magnetic field such as southward polarity, approximate tilt angle of the magnetic dipole axis with respect to the rotational axis and crude estimates for the dipole moment and surface field intensity. A comprehensive discussion about the observations and interpretations of jovian radio emissions can be found in a review by Carr, Desch and Alexander (1983).

The Pioneer encounters in the early 1970's and the Voyager fly–bys in 1979 added a wealth of information about the magnetic field and magnetosphere of Jupiter. In particular, the spacecraft provided *in–situ* measurements of the magnetic field and plasma environment, and maps of the ultraviolet(U.V.) and I.R. emissions associated with magnetospheric processes. The discovery of a plasma torus surrounding the planet at about 6 R_J revealed a strong electrodynamic interaction between Jupiter and its moon, Io (Kupo, Mekler and Eviatar 1976).

Jupiter possesses the largest planetary magnetic moment in the solar system. Its enormous magnetosphere extends out to 50–100 jovian radii from the planet. When discussing the jovian magnetosphere, it is customary to consider the three following regions.

Inner Magnetosphere

This region of the jovian magnetosphere begins at the "surface" of Jupiter and extends out to 6 R_J. The magnetic field in this region is predominantly due to currents in the planetary interior (Acuña *et al* 1983). The effects of the magnetotail and the azimuthal current are unimportant. The widely held view is that the magnetic field is generated by a thermal convection–driven dynamo in the electrically conducting region of the planetary interior. Field variations in magnitude and direction take place over long time scales. The field is smoothly varying when observed along spacecraft trajectories.

The inner magnetosphere contains a torus of cold plasma between 5.3 R_J and 5.6 R_J. The warm torus begins at the orbit of Io (6 R_J), extending to 7.5 R_J. The Io plasma torus is the major source of plasma for the entire magnetosphere. This is in contrast with the Earth, which lacks a significant internal plasma source (Strobel 1989).

Middle Magnetosphere

The magnetic field in this region is dominated by an equatorial current sheet (magnetodisc) beginning at the orbit of Io (6 R_J) and extending to 30–50 R_J. The internal magnetic field can be approximated by a dipole plus small contributions from the magnetopause and magnetotail currents. The azimuthal (eastward) currents in the magnetodisc contribute

radial components to the nearly dipolar internal field, leading to stretching of field lines in the radial direction, along the plane of the current sheet. The current sheet is tilted with respect to the rotational equator resulting in a 10 hour periodic "rocking" motion. The middle magnetospheric region is regarded as a transition stage between the ambient (almost dipolar) internal field and the magnetodisc geometry of the outer magnetosphere.

Outer Magnetosphere

From 30–50 R_J to the magnetopause ($\sim$100 R_J) the magnetic field is highly distorted due to the interaction with the solar wind. The field has a large southward component and shows large spatial and temporal variation as a direct response to the changing wind pressure. The region also includes the extensive magnetotail, which harbours charged particles streaming away from the planet in the anti-solar direction.

Because of the asymmetry of the outer magnetosphere, discussions always differentiate between the "sunwards side" and the "magnetic tail."

The magnetopause on the sunwards side is the region where streaming particles from the solar wind encounter the jovian magnetic field. It is a boundary layer separating the outside region where the magnetic field is determined by the motions of charged particles, from the region where the movements of charged particles are restricted by the internal field. Solar wind particles encountering this boundary are swept around the planet to eventually precipitate into the atmosphere through open field lines, or to end up in the planetary bow shock (a region in the solar wind shadow, on the anti-solar side of the planet).

The jovian magnetotail contains a large current sheet separating the northern and southern lobes of the local magnetic field. Across the current sheet the field reverses direction and field lines tend to lie parallel to the equatorial plane of Jupiter at increasingly large radial distances from the planet.

Magnetic Field Model

In terms of observing Jupiter's auroral emissions, a magnetic field model of the relevant region is essential to interpret the data. To this end a number of magnetic field models have been proposed, the most notable of which are the O_4 model of Acuña and Ness (1976), the P11(3,2)A model of Smith, Davis and Jones (1976) and most recently, the O_6 model by Connerney (1991,1993) which is derived by considering an explicit model of the magnetodisc.

Jupiter's magnetic field can be represented, to first order, by an offset tilted dipole model. However, measurements (Connerney *et al* 1982) indicated that contributions from higher order magnetic multipoles are non-negligible. All models mentioned above attempt to incorporate these higher order components so as to accurately reproduce spacecraft measurements. In addition, the models are used to make important predictions or to explain aspects of observations (made either from spacecraft or from ground–based observatories). The derivation of magnetic field models is outside the scope of this work. Detailed descriptions can be found elsewhere (Acuña and Ness 1976, Smith, Davis and Jones 1976, Atreya *et al* in Physics of the Jovian Magnetosphere (1981)). The paper by Connerney (1991) gives detailed accounts of the procedure used to derive the O_6 model. A brief description will be given of the theory required to reproduce (numerically) the O_6 model of Connerney.

Modelling the inner region of the magnetosphere begins with the assumption that there are no significant current sources in this region, i.e. current density $\mathbf{J} = \nabla \times \mathbf{B} \approx 0$. The field $\mathbf{B}$ can then be represented by a sum of scalar potentials

$$\mathbf{B} = -\nabla V = -\nabla(V^e + V^i) \tag{1.4}$$

where V^e and V^i represent sources external and internal to the region respectively. V can be expanded in terms of spherical harmonics (Chapman and Bartels 1940, Langel 1987) and is given by

$$V = a \sum_{n=1}^{\infty} \left\{ \left(\frac{r}{a}\right)^n T_n^e + \left(\frac{r}{a}\right)^{n+1} T_n^i \right\} \tag{1.5}$$

Here a is the equatorial planetary radius and r is the radial distance. T_n^e and T_n^i are series representing contributions from external and internal sources respectively. The two are expressible in terms of Schmidt–normalised associated Legendre functions

$$T_n^e = \sum_{m=0}^{n} \{P_n^m(cos\theta)\,[G_n^m cos(m\phi) + H_n^m sin(m\phi)]\} \tag{1.6}$$

$$T_n^i = \sum_{m=0}^{n} \{P_n^m(cos\theta)\,[g_n^m cos(m\phi) + h_n^m sin(m\phi)]\} \tag{1.7}$$

where θ and ϕ are the normal right handed spherical polar angles, θ (denoting colatitude) measured from the rotational axis and ϕ increasing in the direction of rotation. System III longitude is obtained by taking $360 - \phi$. G_n^m, H_n^m, g_n^m and h_n^m are the external and internal Schmidt coefficients respectively.

In practice, given the sparseness of the observations, the series is usually truncated at some order $n = N_{max}$, where N_{max} is taken to be large enough to accurately represent the measurements but not so large so as to introduce more free parameters than can be determined by observations. The O_4 model of Acuña and Ness (1976) incorporates terms up to and including n=3 for the internal coefficients but nothing for the external terms. The P11(3,2)A model of Smith, Davis and Jones (1976) incorporates terms up to and including n=3 for the internal coefficients but also has terms up to an including n=2 for the external ones.

The recent O_6 model of Connerney (1991, 1993) is an attempt to make improvements on the O_4 model (Acuña and Ness 1976). It is essentially a partial solution, consisting of the first three orders of a six–order expansion of the source function. Like the O_4 model of Acuña and Ness (1976), the O_6 (Connerney 1991, 1993) model only incorporates internal coefficients for terms up to and including n=3. Unlike the O_4 (Acuña and Ness 1976) model however, the O_6 model (Connerney 1991, 1993) provides for the possibility of contributions to the field by components of orders greater than n=3.

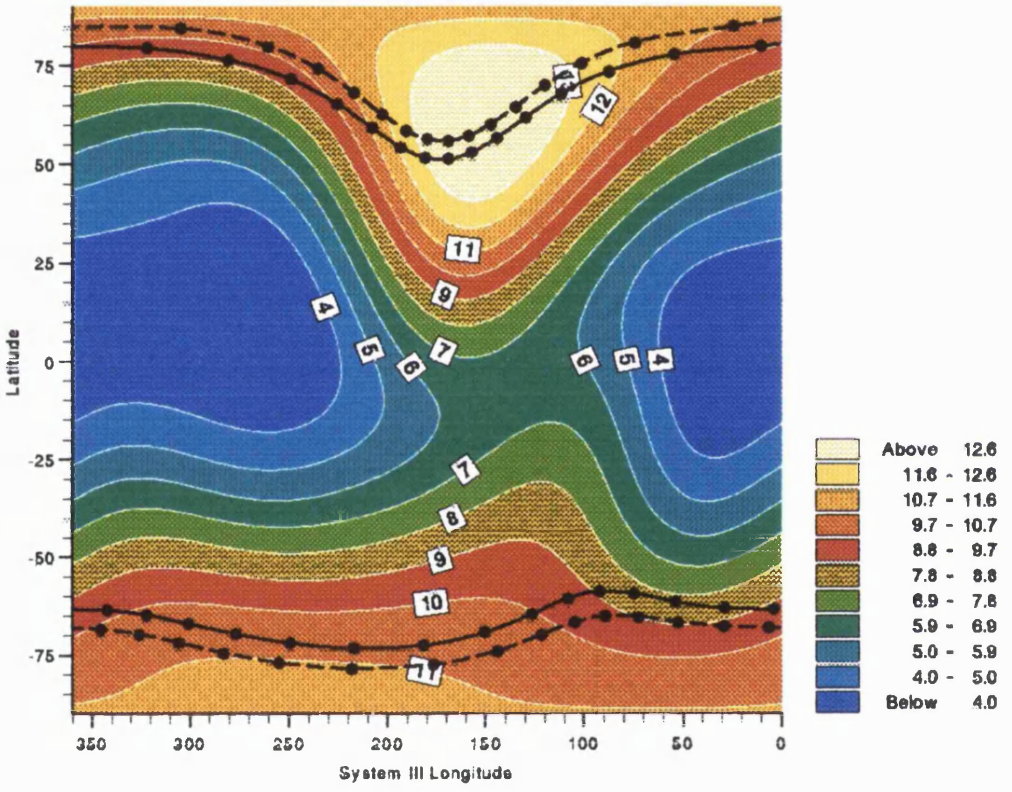

Figure 1.2: A shaded contour map of estimated surface field strength according to the O_6 magnetic field model of Connerney (1991, 1993). The field strength unit is given in Gauss. Plotted on top of the map are the Io Torus footprint (dots connected by a solid line) and the footprint of the Last Closed Field Line – field line 30 R_J (dots connected by a dashed line).

A shaded isocontour map of total surface field intensity as predicted by the O_6 (Connerney 1991, 1993) model can be seen in figure 1.2. This shows that the magnetic field is highly asymmetric. The maximum surface field strength is about 14 G in the north and about 10 G in the south. In addition the high field strength is concentrated in a smaller region in the north than in the south. The model is also used to map footprints of constant magnetic shells on to the surface of the planet. This is invaluable in predicting ionospheric and atmospheric signatures of processes taking place in the magnetosphere. Important examples are the precipitation into the atmosphere of charged particles from the Io plasma torus, and observations of emissions from the foot of the Io flux tube.

The term Last Closed Field Line (LCFL) is used here to denote the field line crossing the equator at a distance of 30 R_J from the centre of the planet. This has been widely employed to mean the boundary between closed field lines and field lines connecting to the interplanetary medium, its footprints on the surface of the planet indicating the auroral boundaries beyond which particle precipitation is thought to occur on open field lines. It should be noted that this boundary is highly variable, indeed U.V. observations (Prangé, private communication) show that north and south auroral emissions may be conjugated indicating closed field lines in that region. Only emissions at the poles may, therefore, be attributed with confidence to open field lines.

1.2.4 The Influence of Io

Io Flux Tube

Strong control of the decametric emissions by the Galilean satellite, Io, was well established before the planetary missions, through the monitoring of jovian radio emissions (Bigg 1964, Desch *et al* 1975, Carr and Desch 1976, Goldstein and Eviatar 1979, Leblanc 1981)).

Explanations of this phenomenon were put forward by Piddington and Drake (1968) and Goldreich and Lynden–Bell (1969). The widely accepted hypothesis, based on a strong electrodymanic interaction between Io and the corotating jovian ionosphere, is given the term "unipolar inductor." Ions and electrons are accelerated by this unipolar generator to energies up to 0.5Mev and then precipitate into the jovian ionosphere. The result of this

is an emission hot spot whose area is restricted by the flux tube intercepting Io. Such a spot has been observed by Atreya *et al* (1977) and, recently, by Connerney *et al* (1993).

Extensive observations and discussions have been made on the nature of the Io flux tube, whose scope is beyond that of this work. Reviews in *Physics of the Jovian Magnetosphere* (A. J. Dessler, ed., 1983) and *Time-Variable Phenomena in the Jovian System* (Belton, West and Rahe, 1989) give more comprehensive discussions.

Io Plasma Torus

Brown (1974) reported optical observations of neutral sodium connected with Io just before the Pioneer 10 encounter. The subsequent discovery of a plasma torus at the orbit of Io was made by Kupo, Mekler and Eviatar (1976) when they observed optical emissions due to S^+ from a region just inside Io's orbit. This was interpreted by Brown as coming from a dense ring of cold plasma.

Because of its highly volcanic nature Io injects a great number of particles into the magnetosphere. Ablation of material from the surface of Io due to impacting particles also makes a substantial contribution.

According to Schardt and Goertz (1983) it is thought that plasma from the various sources (ionosphere, solar wind, etc.) initially diffuses outwards to the magnetotail under centrifugal and plasma pressure. In this region plasma is accelerated to high energies (MeV) and then diffuses back in towards the planet, due to pressure gradient instabilities, to eventually end up in the vicinity of Io. It is here that charged particles are lost to the magnetosphere due to various mechanisms, i.e. atmospheric precipitation, charge–exchange, etc.

The Io plasma torus is made up of two parts (Belcher 1983). The cold inner torus inside of 5.6 R_J, is confined to the centrifugal equator and has a scale height of $\sim$0.2 R_J (Kupo *et al* 1976). The warm outer torus extends from the orbit of Io (5.9 R_J) to about 7.5 R_J and has a scale height of about 1.0 R_J (Broadfoot *et al* 1979). This discovery prompted a substantial shift of focus away from the solar wind, to the Io torus as the main plasma source for the jovian magnetosphere.

1.2.5 Ionospheric Emissions

Emissions from the jovian auroral regions at UV and IR wavelengths have been observed both by spacecraft and ground–based observatories. In addition, low level emission, termed "electroglow," was observed by Voyager to emanate from all areas of the planet. The emissions arise from particle precipitation and Joule heating which, in turn, are linked to physical processes taking place in the magnetosphere. To interpret the emissions it is necessary to have some idea of these magnetospheric processes and their consequences for the atmosphere.

Magnetospheric Processes

According to Bryant (1993) a charged particle from the solar wind encountering Jupiter's magnetic field will either precipitate into the atmosphere or be deflected from its path. The outcome is dependent on the particle's momentum per unit charge (known as magnetic rigidity), P, and the strength of Jupiter's magnetic field, $\mathbf{B}$, where P is defined by:

$$P = \frac{\rho c}{Ze} = \frac{[E^2 + 2EE_0]^{1/2}}{Ze} \tag{1.8}$$

Ze is the particle's charge, ρ is the particle's momentum, E and E_o are its kinetic and rest energy in electron-volts, and c is the speed of light in a vacuum. P is in terms of volts. Reaching Jupiter's surface is possible only if P is $>> \int \mathbf{B} \times d\mathbf{l}$, where $d\mathbf{l}$ is an element of trajectory. The integral $\int \mathbf{B} \times d\mathbf{l}$ represents the impulse experienced by the particle on crossing the magnetic field lines. Therefore, for a given energy, a particle is much more likely to reach Jupiter's atmosphere if its approach is close to the polar regions, with its velocity is nearly parallel to the magnetic field, than if it approaches the planet near the equatorial plane, where its velocity is nearly perpendicular to the field lines.

For solar wind particles, precipitation will occur over the whole of the polar regions giving rise to diffuse auroral emissions.

For a charged particle injected inside Jupiter's magnetosphere, escape is difficult. The particle may either precipitate into the planetary atmosphere or become trapped in the magnetic field, depending on its pitch angle, α. This is the angle between the particle's

velocity vector, **v**, and **B** (the local magnetic field vector). If this angle is less than the half angle of the local loss cone, α_l, the particle cannot mirror (reverse its motion) above the atmospheric boundary and is therefore lost to the magnetosphere. The loss cone angle, α_l, is given by

$$sin^2\alpha_l = \frac{B}{B_s} \tag{1.9}$$

where B is the local field strength and B_s is the field strength at the point in the atmospheric boundary on the same field line as the particle. For pitch angles larger than the loss cone angle, the charged particle will 'bounce' between two mirror points, drifting slowly in longitude until it reaches a region where the surface magnetic field strength is low enough to place the mirror point below the boundary of the atmosphere. The particle will then enter the atmosphere and cease to follow adiabatic motion. Instead it will lose its energy through collisions with ambient atmospheric particles.

However, a particle can be scattered into the loss cone, through pitch angle diffusion. This is accomplished through collisions with other particles, or interaction with magnetospheric waves. The process is non-preferential (i.e. does not occur at a selected region) and therefore takes place over the whole of the magnetospheric region which maps down along field lines onto polar caps. The observable result is diffuse emission throughout the polar regions.

The outward radial diffusion of ions and electrons within Jupiter's magnetic field induces a persistent current in the plasma sheet. Sheet currents are also associated with the failure of the plasma to corotate with the planet beyond 20 R_J (Jovian radii). the latter are connected to Jupiter's ionospheric Pedersen current by Birkeland (magnetic-field-aligned) currents. The resulting 'circuit' draws angular momentum from the planetary ionosphere and transfers it to the plasma. Charged particles move into and out of the ionosphere via these field-aligned currents and deposit energy into the atmosphere during their precipitation through inelastic collisions with ambient atmospheric particles. Energy is also deposited through the electrical energy dissipation (Joule heating) associated with the ionospheric current itself. The resultant auroral emission appears as discrete structures along the 'magnetic footprint' of that part of the outer plasma sheet which carries the

associated currents. This regions of the sheet extends to the point where the transition from closed field lines to 'open' field lines connecting to the interplanetary medium occurs.

The different kinds of emissions therefore, give clues to the type of energy deposition taking place in the various parts of the aurorae. Joule heating affects the temperature of the ionosphere. It does not influence the population of the electrons occupying specific atomic and molecular energy levels. Joule heating affects only emissions in the I.R., whereas particle precipitation will excite individual bound electrons, ionise and heat the neutral gas. Particle precipitation will, therefore, also give rise to U.V. as well as I.R. emissions.

Jupiter's UltraViolet Auroral Emission

UV auroral emissions are mainly due to H_2 Lyman and Werner bands, and the H Lyman α line. The emissions are due solely to radiative de–excitation of collisionally excited atomic and molecular hydrogen. Excitation is by direct particle precipitation and secondary electrons (McConnell, Sandel and Broadfoot 1980). UV emissions are therefore perceived as the principal indicator of effects arising from atmospheric absorptions of particle precipitation flux (Atreya *et al* 1982, Shemansky 1984). Observationally, the UV lines suffer significantly from hydrocarbon and self absorption, which means that the result very much depends on the model atmosphere used and modifications to it because of precipitation (Clarke *et al* 1989). However, UV lines above 1400 Å are not affected at all by absorption and are therefore excellent tracer of energy input.

Broadfoot *et al* (1979) attempted to locate the northern UV auroral region using data from the Voyager UVS experiment. They concluded that the UV auroral emission is distributed along a closed region surrounding the pole, with a maximum around 180° longitude (system III). This oval does not appear to coincide with the Io torus footprint, or any of the magnetic shells footprints. The difference could be due to experimental uncertainties, inaccurate surface field prediction by the O_4 model and from particles not precipitating on constant magnetic shells.

During the course of this work remarkable advances have been made in the study of

jovian auroral UV emission using the Hubble Space Telescope. The latest UV images now clearly show that the UV auroral emission is located along the footprint of the last closed field line, as determined by the O_6 model, in a continuous oval with a region of diffuse emission, around longitude 150°, inside the oval itself (Dols *et al* 1992, Gérard *et al* 1994).

Infrared Auroral Emissions

Infrared auroral emissions have been attributed to a number of molecular species. Hydrocarbons such as methane (CH_4), acetylene (C_2H_2), ethylene (C_2H_4), ethane (C_2H_6) and benzene (C_6H_6) have all been identified on Jupiter (Ridgeway *et al* 1976, Atreya *et al* 1981, Kim *et al* 1985). Quadrupole H_2 transitions (De Bergh *et al* 1974) and most recently H_3^+ ro-vibrational transitions have been used to infer temperatures in the jovian atmosphere at the 1–2 μbar pressure level and above.

The I.R. emissions can come about through energy transfer with the thermosphere, collisional excitation (or ionisation of H_2 in the case of the formation of H_3^+) by charged particle precipitation and Joule heating by currents in the ionosphere.

Auroral emissions exhibit features termed "hot spots" in both the northern and southern polar regions. In the north, enhanced emissions have been observed around 180° longitude (system III) for methane (Caldwell *et al* 1980) and acetylene (Drossart *et al* 1986) and around 150° for H_3^+. Much less study has been made of the southern aurora and consequently less is known about the southern IR emission hot spots. Some have observed the southern hot spot to be between 0° and 90° longitude. However, others have also found the hot spot to drift in longitude.

Ionospheric H Lyman-α Emission and the H Lyman-α Bulge

H Lyman-α emission has also been observed from all parts of Jupiter. The monitoring of H Lyman-α shows an enhancement in the emission around 102° longitude and 8–12° latitude (H Lyman-α bulge) (Sandel *et al* 1980, Clarke *et al* 1981). Both the bulge and non-bulge brightnesses has been closely linked to solar activity over the past decade (McGrath 1991). Recent HST spectra at Lyman-α show evidence of broadening and of turbulent Doppler

shifted lines. Processes proposed to explain the emission include resonant scattering of solar H Lyman-α, charge particle collisional excitation of H and dissociative excitation of H_2. The current explanation of the H Lyman-α asymmetry is that the increased rightness is due to increased broadening of the line-width at bulge region over those in non-bulge (Clarke *et al* 1991), thereby increasing the range of wavelengths scattered by the H Lyman-α line.

1.3 H_3^+ on Jupiter

1.3.1 Detection

The detection of H_3^+ on Jupiter furnished astronomers with a potentially useful probe of the physical conditions of the jovian ionosphere (Drossart *et al* 1989). Since 1989 a number of questions have been answered about H_3^+ and its existence on Jupiter. The emission was found to originate around the 0.1 to 10^{-3} μbar level (Drossart *et al* 1989). The temperature ranges from around 600 K (Oka and Geballe 1991) to over 1000 K (Miller *et al* 1990, Maillard *et al* 1990. H_3^+ column density can be as high as 10^{13} cm^{-2}. Spectra (Miller *et al* 1991) and images of Jupiter at wavelength sensitive to H_3^+ emission showed that auroral H_3^+ emission is more closely associated with open magnetic field lines connecting to the magnetotail than the Io Plasma Torus (IPT)(Baron *et al* 1991, 1992, Satoh *et al* 1993). This would mean that the mechanism responsible for H_3^+ emission was different than the then accepted processes responsible for the U.V. and hydrocarbon emissions. With the new Hubble images, however, the U.V. aurorae have now come back into line with the I.R. data (Gérard *et al* 1994).

1.3.2 Spectroscopy

Normally extremely reactive, the survival of H_3^+ in the jovian ionosphere is due to the fact that formation occurs above the homopause where only helium and hydrogen exists in appreciable concentration. The only effective destruction mechanism on Jupiter, therefore, is dissociative recombination.

Drossart *et al*'s (1989) data remains, to date, the most spectrally extensive coverage of H_3^+ in the K window. A theoretical spectrum fitted to the data found temperature to be around 1100 K and column density to be 1.4×10^9 cm^{-2} in the $2\nu_2(l = 2)$ vibrational level. Drossart *et al* (1989) also raised a number of questions concerning the environment that H_3^+ formed in, such as spatial distribution, temporal variability and the effect this ion has on the energy balance of the jovian atmosphere.

Miller *et al* (1990) obtained medium resolution spectra using the CGAS instrument on NASA's IRTF. They reported that the fundamental spectrum fitted well to a 1000 K theoretical spectrum and that the ratio of the overtone to fundamental line intensities gave a temperature of 1099($\pm$100) K. The results suggested that the H_3^+ population is in (near) thermal equilibrium in the ionosphere of Jupiter. This was further confirmed by Drossart *et al* (1993) who managed to resolved the H_3^+ lines to obtain the intrinsic line profile. They found a translational temperature of 1150$\pm$60 K, close to their derived rotational temperature of 1250$\pm$70 K. Oka and Geballe in 1990 also presented their own H_3^+ spectral observations. They derived a temperature of only 640 K and were unable to detected the overtone spectrum. This showed that the nature of the H_3^+ population may be highly variable and changes would take place at least over time scales of several months.

Miller *et al* (1990) attempted to determine, spectroscopically, the spatial distribution of H_3^+ using NASA's IRTF. They obtained spectra by positioning the beam of the telescope on the limb of the planet, at selected latitudes. They found average temperature to be about 800 K and average column density to be a few $\times10^{12}$ cm^{-2}. No appreciable H_3^+ emission were detected at latitudes 60° or less in either hemisphere. In addition, Miller *et al* (1991) also showed that H_3^+ can play a significant role in the energy balance of the jovian atmosphere. UV measurements of the aurorae showed that peak energy input is of the order of 100 erg s^{-1} cm^{-2}, with increases by a factor of 10 during particular events. Calculations by Miller *et al* (1991) demonstrated that H_3^+ may re-radiate between 1.5 and 15% of this amount back into space.

Ballester *et al* (1994) were the first to show that H_3^+ emission can be detected right

across the planet. Using the CGS4 cooled grating spectrometer mounted on the United Kingdom Infrared Telescope (UKIRT) they obtained 3.45μm spectra along the central meridian longitude (CML). They reported intense H_3^+ emission lines around the poles as expected. However, they also found appreciable H_3^+ emission at lower latitudes.

In their analysis, Ballester *et al* (1994) divided the data into three regions: mid to high latitudes in the northern and southern hemisphere, and a low–latitude region encompassing the equator. Their fit to the data gave fairly low temperatures for the mid to high latitude regions (734 K and 813 K respectively for the north and south) and considerably higher temperature (1220 K) for the central region. The CML of their data, 102°, coincided with the maximum of the H Lyman-α bulge, prompting the suggestion that the elevated temperature may, some how, be connected with bulge activity.

In addition to the H_3^+ features the spectrum also showed two prominent emission lines at 3.517 and 3.522μm whose intensity was greatest just north of the equator. To date, no one has identified the species responsible for the doublet feature.

1.3.3 Images of the Jovian Aurorae

Baron and Owen (1990) first used the infrared camera, ProtoCam, mounted on the NASA IRTF to obtain images of Jupiter. They were trying to look at the jovian aurorae emission at the central wavelength of 4.0μm, specifically to observe the strong Q(3) fundamental H_3^+ emission complex. At this wavelength the absorption of incident solar radiation by the methane layer is incomplete and images of Jupiter show considerable structure, especially on the body of the planet. They did observed brightening around the polar regions, but could not comment on whether this was due mainly to H_3^+ or not.

In 1991 images of the Jovian aurorae at wavelengths 3.4μm and 3.533μm were obtained by Baron *et al* (1991) and Kim *et al* (1991). In this wavelength region there is an almost complete absorption of the incident solar radiation by the methane ν_3 band, making the disk of Jupiter nearly dark. H_3^+, originating from some way above this layer, shows up as very bright auroral emission.

To interpret the H_3^+ images Baron *et al* (1991) assembled mosaics of the planet and

fitted them to a disk which had been reliably calculated. The planet's oblate "surface" was then fitted to the individual auroral images by comparing each frame by eye to the full mosaic, making use of the low-level signal away from the main H_3^+ emission. Their results showed that the H_3^+ emission was fixed with respect to the magnetic poles, extending over the entire polar region but confined to latitudes above 60°. They also observed that in the north, there were bright spots around longitudes 145° and 230°, and a local minimum at longitude 180°. In the south, strong emissions were seen from 300° to 90° with a weak maximum around 260°. The conclusion arising from their analysis was that the main body of H_3^+ emission were coming from latitudes that mapped the open field lines connecting with the magnetotail.

Kim *et al* (1991) had a different interpretation of their I.R. auroral images. To determine the location of the features they preferred to use images of Jupiter taken at 2.0μm where H_3^+ emission is negligible compare with the polar haze emission (Kim *et al* 1992, Drossart *et al* 1992). The H_3^+ images were superimposed on the 2.0μm images and used the limb clearly visible in the 2.0μm image to fix the position of the H_3^+ emission. The results led them to conclude that the main H_3^+ emission was located at latitudes lower than those determined by Baron *et al* (1991) and that there were hot spots on either side of the central meridian.

This view was supported by Drossart *et al* (1992) who performed their limb fitting by using two white spots observed at other wavelengths, whose position is known, to locate the limb of the planet.

This difference of opinion had far more implication than just the positions of the auroral features. The latitudinal location of the H_3^+ emission peak can make a unique determination of the mechanism thought to be responsible for the main auroral processes (at least in this wavelength region).

If, according to Kim *et al* (1991) and Drossart *et al* (1992), the main H_3^+ emission peak was only just northward of the UV auroral ovals then the dominant particle source for the formation of H_3^+ would be the Io plasma torus, which, was also thought to be responsible for the UV auroral ovals. This would have confirmed the view many have held since the

Pioneer and Voyager fly–bys, that is, the Io plasma torus is the principle source of charged particles precipitating into the jovian atmosphere. The connecting of H_3^+ emission with U.V. and other I.R. auroral emitting species was interpreted as just more evidence of Io's effect on the planet.

This view was not shared by Baron *et al* (1991) however, who felt that a much more accurate fitting of the limb is made if the auroral features were located at somewhat higher latitudes. Their interpretation suggested that the auroral H_3^+ emission was driven by precipitating particles coming in on open field lines connecting with the magnetotail of Jupiter. This shifted the focus of attention away from Io and onto regions further out in the magnetosphere, requiring revision of ideas about the effects of the magnetosphere on the atmosphere.

To date the most impressive work on the I.R. imaging of the jovian aurorae has been carried out by Satoh, Baron and Connerney (1993). They took some hundred ProtoCam images and turned them into video sequences showing the structure of the auroral emission at all longitudes as the planet rotate. They showed that in the north the aurora consists of a bright oval offset from the rotational pole. Connecting with it was a more diffuse region around longitude 150°. According to Connerney's O6 (1993) magnetic field model this longitude coincides with region of highest surface magnetic field on Jupiter. Also the work conclusively demonstrated that the earlier analysis of Baron *et al* (1991) was correct.

In a follow up paper, Connerney *et al* (1994) showed that the signature footprint of Io itself is visible in some of their images as a spot quite separate from the main auroral body. This remarkable result served to fix the position of the field line crossing the equator at 5.9 R_J.

The most recent analysis of jovian H_3^+ images to be published are those of Kim *et al* (1994). The authors pointed out that their earlier work exhibited a puzzling feature that could not be readily explained. Their method of analysis highlighted a sharp decrease in emission intensity near the limb in non-auroral regions. There was also spherical aberration in the IRTF telescope which caused an extended limb in the 2.0μm images and of which they were not aware of at the time. They thus adopted a limb fitting method which made

use of non-auroral emission to determine the limb of the planet. Their results now show observed auroral emissions to be coming from ovals in both the north and the south polar region. The peak auroral emission features are now interpreted as located at the footprint of the 30 R_J magnetic shell and above, broadly in agreement with Baron *et al* (1991), Satoh, Baron and Connerney (1993) and Connerney *et al* (1994).

The work described above demonstrated that imaging Jupiter at wavelengths sensitive to H_3^+ emission is an invaluable tool with which to locate auroral emission features on the planet, thereby placing constraints on magnetic field models of Jupiter.

1.3.4 H_3^+ and the Comet Shoemaker-Levy/9 Impact

The impact of comet Shoemaker–Levy/9 with Jupiter in July 1994 was a unique event in the history of planetary astronomy. It created an opportunity to monitor changes in the disturbed ionosphere, using the knowledge gained from this study of H_3^+. To understand the changes caused by this event it is necessary to know the behaviour of the undisturbed atmosphere. This is important to see what effect, both long and short term, the impact has on Jupiter.

The impacts of the cometary fragments caused huge disturbances in the jovian atmosphere, dredging up material from lower down. The impact sites were still visible in the I.R. weeks after the initial collision.

Spectroscopic and imaging studies using H_3^+ emission showed a dramatic change in the jovian ionosphere. The northern auroral H_3^+ emission was observed to double in brightness while the southern aurora was seen to diminished considerably Dinelli *et al* (1995). The impacts themselves were observed to cause ionospheric brightenings at their northern counter points, within hours of the cometary fragments colliding with Jupiter (Schulz *et al* 1995). The results showed that charged particles were transported in large numbers, away from the impact sites to the northern hemisphere, along the magnetic field lines. The cometary impact was expected to induce changes in the ionosphere but the increase in brightness of the northern aurora corresponding to a decrease in brightness of the southern aurora was a surprise. Achilleos *et al* (1995) suggested that changes in

H_3^+ auroral intensities were due to changes in conductivity of the ionosphere, causing a preferential flow of charged particles to the north.

The programs developed in this work to study H_3^+ emission were adapted and used to study the methane spectra of Jupiter from the impact sites (Miller *et al* 1995). The results showed that, for one of the fragments, there were signs of pre and post main impact events.

1.4 The Aims of this Study

The focus of this study is to characterise the H_3^+ emission on Jupiter and its relationship with other ionospheric and magnetospheric processes. The principle reason for this is to determine the nature of the mechanism(s) causing the formation of H_3^+ and to what extent does it relate to the UV and other IR emissions.

In the auroral regions it is believed that particle precipitation is the prime mechanism responsible for the production of H_3^+. Whether the source of the particle flux is the Io Plasma Torus or regions in the magnetotail is still not completely determined. Examination of the relationship between H_3^+ emission and surface geometry of the jovian magnetic field should give some clue about the nature of the particle flux. Joule heating has been proposed as a significant energy source to the jovian atmosphere. Where this is taking place and how the energy is then distributed throughout the thermosphere is a question that is still troubling atmospheric modellers.

It has been shown that the energy radiated away by H_3^+ emission is not an insignificant fraction of the total energy input. Exactly how much and what role does this play in the energy balance is vital to understanding the dynamics of the atmosphere.

Taking the points above into account, we propose to perform the following:

1. At the present time, there exists no comprehensive mapping of H_3^+ over the entire jovian disk. We hope to establish a **baseline** study to assist with future works.

2. We set out to establish average temperature and column density values of H_3^+ as a function of latitude, thereby placing constraints on atmospheric models.

3. We also aim to investigate the longitudinal dependence of, particularly, the auroral H_3^+ emission.

4. The distribution of H_3^+ is important to understanding the nature of the mechanism causing its formation. We are, therefore, looking at the detailed morphology of the auroral regions through the use of images.

Taking the results of the above we hope to look for links between H_3^+ emission and other magnetically related phenomena. We also look at the contribution of H_3^+ to the energy balance of the planet.

Finally, it is hoped that the knowledge gained from observing H_3^+ on Jupiter may serve to further the search for H_3^+ in other astronomical environment.

Chapter 2

Data Collection and Analysis

Developments of astronomical instruments have made remarkable advances over the last decade. The charge couple device (CCD) revolutionised the way astronomy is being practiced, enabling astronomers to obtain more and better quality data within the available time period. Infrared instruments still lag behind their optical counter parts in terms of sensitivity and size of the detector array. However the gap is narrowing all the time.

The upgraded Hubble Space Telescope now gives unprecedented spatial resolution. Planetary astronomers can now resolve the jovian UV auroral emission into distinct oval, mapping it to footprints of magnetic shells. Unfortunately, it does not have an instrument capable of observing in the near infrared where H_3^+ emits strongly.

Ground-based telescopes have also undergone dramatic developments. Adaptive optics now means that large telescopes with mirror diameters of 8–10 m are already available and more are being constructed with the view of linking them up to achieve even higher angular resolution.

Older telescopes now have their usefulness being extended through the implementation of tip-tilt optics, giving them the ability to significantly cancel atmospheric seeing, a constant problem in infrared astronomy.

Infrared astronomy differs from other areas of astronomy in that the atmosphere presents a considerable barrier to astronomical fluxes. Absorption in the atmosphere by water and other molecules means that observations can only be made in a limited number

of wavelength ranges called infrared windows. The filters used to select these wavelength windows are designated "J H K L L′ M and N." Additional difficulty presents itself in the form of bright and fluctuating background due to thermal emission from the telescope and the atmosphere. This places severe constraints on observational parameters.

Although the use of CCD detectors meant easier data handling, the often noisy detectors (substantially more than the optical counterparts) require extra processing to get the most out of the data.

For monitoring jovian H_3^+ emission, the need is for instruments with high sensitivities and good spatial coverage so that data can be obtained relatively quickly and therefore more regions of Jupiter can be sampled within the time allocated. The two instruments used in this study are ProtoCam, mounted on NASA's InfraRed Telescope Facility (IRTF), for imaging work and CGS4, mounted on the United Kingdom InfraRed Telescope (UKIRT), for spectroscopic mapping, both of which are sited on Mauna Kea, Hawaii.

In the following sections we will give brief descriptions of the processes and techniques used in the acquisition and reduction of image and spectroscopic data, to be presented in later chapters.

2.1 Definitions of Some Basic Terms

The following are some basic data types that are typically collected during an observation run.

- Bias — A short blank observation to determine the minimum noise level ever present when using the detector.
- Dark — Blank observation with the same exposure time as an observation. Used to determine the contribution of the detector to the noise level.
- Flat — Observation of black-body calibration source, either of the sky or the illuminated dome. Used in the data reduction to remove the pixel to pixel variation in the signal.

- Object — Observation of the object.
- Sky — Observation of a blank part of the sky and used to remove atmospheric contribution to the **Object** frame.
- Standard — Observation of a standard star (divided by a black-body and used to flux calibrate the object spectrum).
- Arc — Observation of arc lamp lines to provide for wavelength calibration.
- Coadd — A frame formed from the mean of a number of images or spectra in order to improve the signal to noise.

2.2 ProtoCam Image Data

The ProtoCam instrument proved, for a number of astronomers, to be quite efficient at its task (Baron *et al* 1991, 1993, Connerney *et al* 1993, and also see previous chapter). The camera can operate at resolutions ranging from 0.35″ down to 0.135″. The detector is a 62×58 InSb array. This instrument was superseded in 1994 by the more sensitive NSFCAM with a much larger detector array (256×256).

In this section we describe the procedures used to analyse images of Jupiter taken on the nights of the 22nd and the 23rd of April 1993 using the ProtoCam infrared camera mounted on the IRTF.

The images were taken using circular variable filters (CVF) centered at 3.53 μm, 3.80 μm and 4.0 μm to select the required wavelengths. The filter band pass was about 0.05 μm in these three wavelength regions. Seeing for both nights was better than 1.0″.

Images were recorded with pixel size set at 0.25″. At the central wavelengths of 3.53 μm and 3.80 μm, ten coadds were used for each image with an integration time of 4 seconds for each coadd. The same amount of time was used for the sky observations. At 4.00 μm six coadds were used for each image, with a 1 second integration for each coadd.

The images were obtained at four coordinate settings relative to the center of the Jovian disk, in order to get complete coverage of the auroral regions (see figure 2.1). Images of

the standard star HD106965 were obtained throughout the night in the K and L windows and at the central CVF wavelength of 3.533 μm. Bias and Dark frames were obtained at the beginning of each night's observation. Dome and sky flat field frames were obtained half way through each night.

Since the ProtoCam field of view was about 15″, only a portion of the disk was seen at any one time. It was decided that in addition to the pairs of images of the aurorae, mosaics of the whole planet were to be obtained at 3.533 μm and 4.05 μm in order to make up composite pictures of Jupiter for analytical purposes. On the first night the images were taken in quick succession going, initially, clock-wise around the limb of the planet, starting on the east limb and then ending up taking images on the body of the planet to fill in the mosaics. On the second night mosaic images were obtained by taking exposures along lines parallel to the vertical axis of the telescope, in addition to those going clock-wise around the limb of the planet.

2.2.1 Data Reduction

Dark and bias current frames were first subtracted from all image frames before any other reduction steps are taken. A bad pixel mask was constructed using a flat field image and then applied to all other images. Flat fields frames were prepared by coadding five images taken of the inside of the illuminated dome. Five images of a blank part of the sky were also obtained and coadded together and the resultant subtracted from the dome flat field frame. A surface was fitted to the flat field and then divided back into it to obtain a normalised flat field frame.

All observations of the object were corrected for the intensity of the sky by subtracting with the associated sky frames. The flat field frame was then divided into the images to correct for pixel to pixel variations. Finally the images were corrected for bad pixels using a 3x3 pixel grid and replacing the value of the bad pixel by an average value of the surrounding good pixels.

At this stage we discovered a problem with the auroral images which was not apparent at the time of observation. Each pair of auroral images were affected by an unknown light

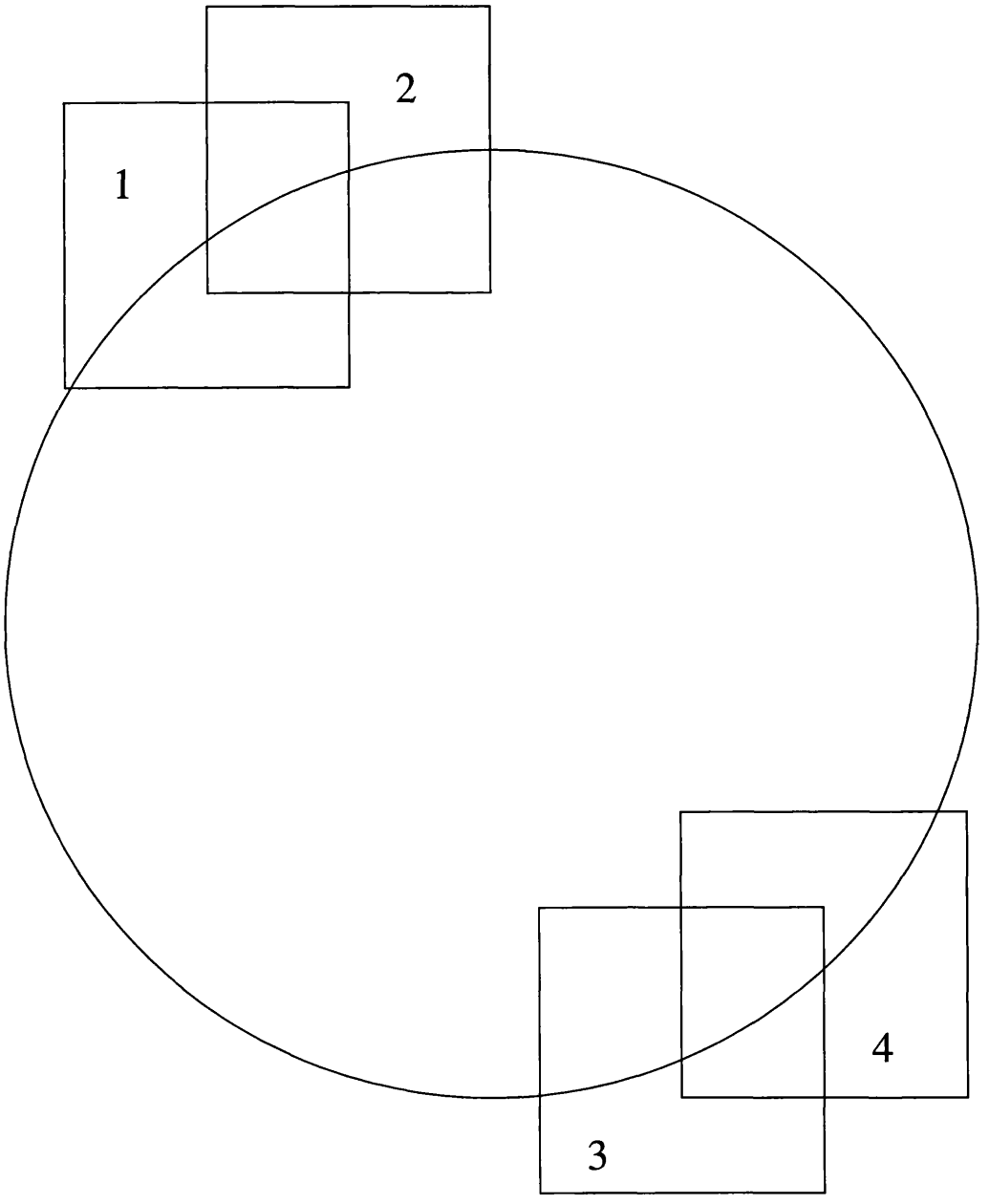

Figure 2.1: Positions relative to the center of the planet at which ProtoCam images were taken in order to achieve complete coverage of the jovian auroral regions.

source which enhanced the brightnesses of images taken at positions 1 and 3 (see fig 2.1). The associated blank sky images did not appear to have this contamination. The most affected areas were those near to the edges of the images, with small contibutions to the overall intensity to the central areas containing auroral emissions. Attempts were made to get rid of the brightness enhancement by fitting a function to the images and then dividing by this function. However, the presence of auroral as well as emission from the body of the planet make this a near impossible task to achieve correctly. We had to contend with fitting the pairs of images together as best we can.

2.2.2 Limb Fitting Procedure

In order to determine the positions of the features on the disk it is necessary to define the position of the limb accurately. Previous experiences analysing images of Jupiter showed that there are some doubts about the accuracy of fitting the limb, either by eye and making use of non–auroral emission to determine the limb (Baron *et al* 1991) or by using some known features, observed at other wavelengths, to fix the position of the planet. We choose to use the method preferred by Baron *et al* (1991), in which they judged the position of the limb by comparing the individual images with a mosaic of the planet, which had been reliably fitted with the elliptical "surface" of the planet, making use of the non–auroral emission as a guide. However, instead of just making visual comparisons, we superimpose the auroral images over the mosaic and then make use of the non–auroral limb to position the images. An outline of the planet is then used to judge the correctness of the fit.

The mosaics of the planet at 3.53 μm and 4.0 μm (figures 2.2 and 2.3 were assembled using the **imaging** program (see section programs). The images were first located in a grid in their estimated positions (relative to the center of the planet which was placed at the center of the grid). The visible edge of the planetary "surface" is then drawn over the mosaic and use to help with the alignment. The coordinates of the limb were computed by taking the scalar product between the line of sight vector and the vectors normal to the planetary surface. The whole mosaic was re-examined and each image shifted to align with the neighbouring images and the planetary outline.

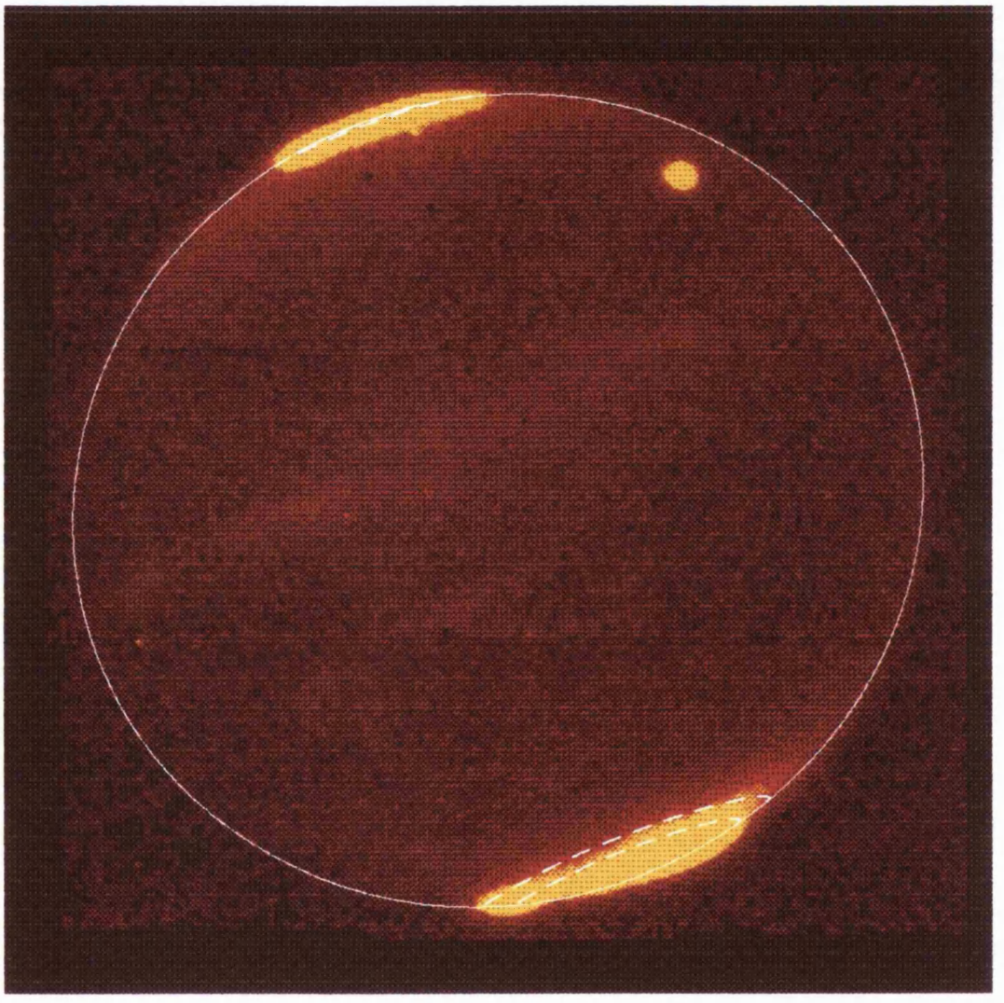

Figure 2.2: A 3.533 μm mosaic of Jupiter composing of nine separate images. These were obtained on the 22nd of April 1993, at the System III CML of 316°. The most intense emission is shown as orange to yellow, and the least as dark brown to black. The dashed lines are marking out the Io Torus footprint (magnetic shell 6 R_J) and the footprint of the last closed field line (magnetic shell 30 R_J) according to Connerney's O_6 model (1991, 1993). An elliptical "surface" of Jupiter was drawn around the planet to aid with the alignment of the images.

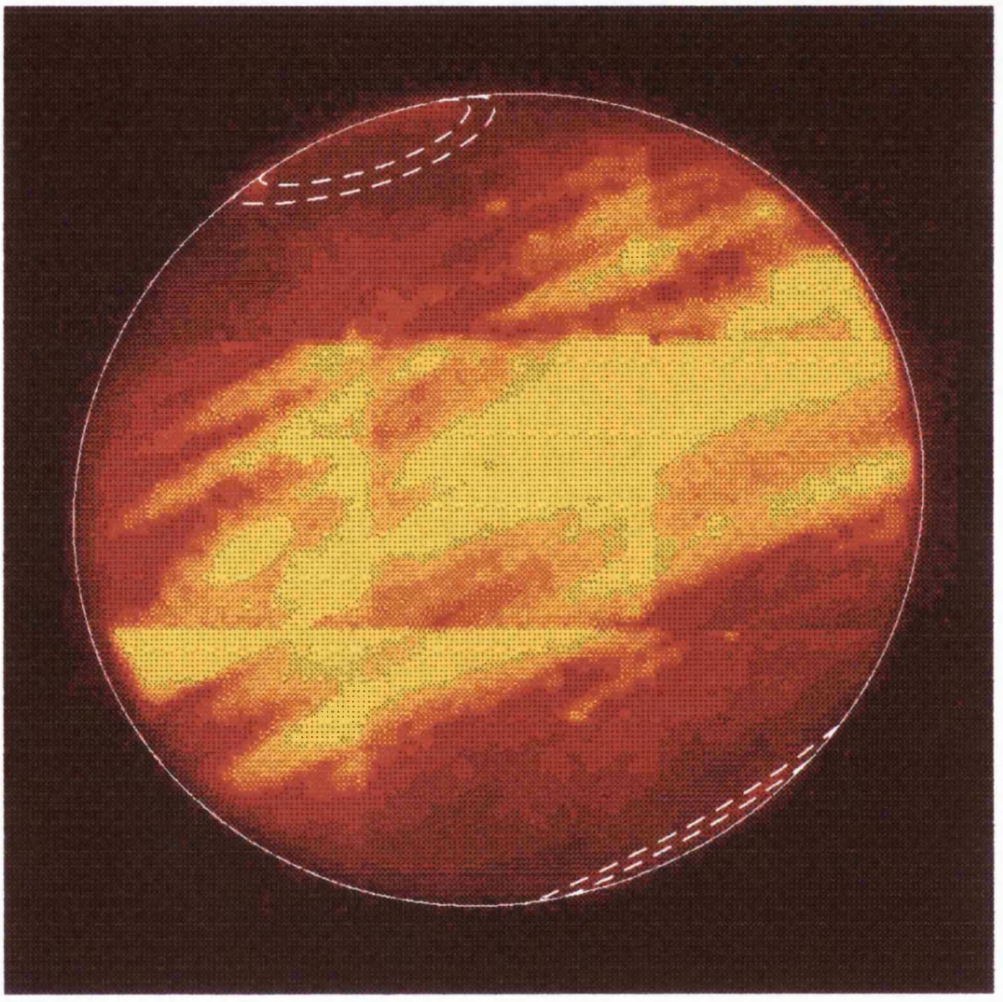

Figure 2.3: A 4.0 μm mosaic of Jupiter composing of nine separate images. These were obtained on the 23rd of April 1993, at the System III CML of 189°. The most intense emission is shown as orange to yellow, and the least as dark brown to black. The dashed lines are marking out the Io Torus footprint (magnetic shell 6 R_J) and the footprint of the last closed field line (magnetic shell 30 R_J) according to Connerney's O_6 model (1991, 1993). An elliptical "surface" of Jupiter was drawn around the planet to aid with the alignment of the images.

For the 3.533 μm mosaic, colour shadings were manipulated to enhance the continuum emission from the body of the planet as much as possible, to bring out the planetary disk. Although very faint this is of great help in fitting the images together to make the mosaics. Figure 2.2 shows a 3.533 μm mosaic of Jupiter taken on the night of the 22nd April 1993. The CML is given in the top left hand corner of the image. A grid of longitudes and latitudes together with the mapping of the Io torus footprint and the last closed field line onto the polar region is superimposed on the mosaic to help with locating auroral features.

A mosaic of Jupiter taken at 4.0 μm is shown in figure 2.3. Emission from the body of the planet is very bright compared to the H_3^+ auroral emissions. However the flux suffers from limb darkening due to an increase in the number of absorbing molecules along the line of sight. The planet, therefore, looks slightly smaller than its elliptical outline. The reverse is true for the optically thin H_3^+ emission, originating from above the methane cloud layer. The limb-brightened polar emissions are clearly visible in the image and appear to sit on top of a background that had diminished considerably compare to the equator.

Using the mosaics as a guide to fitting the limb, images of the auroral regions were "pasted" on top and then shifted to fit in with the picture of the planet, making sure that the limb looks as continuous as possible. The planetary outline is then drawn over the top of all this and the image adjusted again to fit in with the outline as well as the mosaic of the planet. This final adjustment usually only requires small shifts of the order of a couple of pixels or so.

2.2.3 Limb-Brightening Correction

Since H_3^+ emission is optically thin, accurate determination of the morphology requires that the limb-brightening effect be corrected for. Drossart *et al* (1992) made the correction by multiplying the intensity of every point on the disk by the cosine of the emission angle. This probably over-compensates for emission originating close to the limb.

The procedure here is to calculate the ratio of the effective line of sight at a point on the disk to that at the center of the disk, assuming that the emission comes from a shell

of gas of uniform thickness (see figure 2.4). A value of 72,419 km was used for **R** at the equator since we believe that the peak H_3^+ emission originates about 1000 km above the surface of the planet at visible wavelengths (i.e. the ammonia cloud tops). A scale height of 500 km was used for the H_3^+ layer, **H**. This value corresponds to the peak scale height of the H_3^+ model given by Trafton *et al* (1994).

For each pixel on the disk, its x–y coordinate relative to the center of the planet is converted into the corresponding longitude–latitude coordinate and used to calculate the line of sight correction. No attempt is made to allow for the fact that each pixel covers a finite area of the planet. Models will have to be made to estimate how large a column of gas each pixel sees, the effort of which did not seem to justify the potential improvement made to the images. Typical values of the **L/H** ratio for pixels near the limb of the planet ranges from 1.5 to 5. This increases sharply to 12 right at the limb of the planet, however this only affects pixels imaging the planetary edge.

The correction formula was coded into two FORTRAN subroutines, the first to compute the longitude–latitude coordinate of a pixel given its x–y position relative to the center of the planet, the second to calculate the length of the gas column at the computed longitude–latitude relative to that at the center of the planet and then returns the ratio of the two. For auroral emission seen above the limb of the planet the line of sight ratio was set to twice that of a point on the limb since the path length of the atmosphere extends to the corresponding point on the other side of the planet. This may be slightly inaccurate at such geometry since the optically thin assumption may not hold for such long path lengths. For other pixels outside the disk of the planet, i.e. the sky part of the image, the line of sight ratio was set to the same value as for auroral emission seen just above the limb. This renders that part of the image very dark and highlights emission from the planetary disk. The subroutines are all accessible within the **imaging** program depending on the chosen option. The effect of this procedure can be seen in images shown in the next chapter.

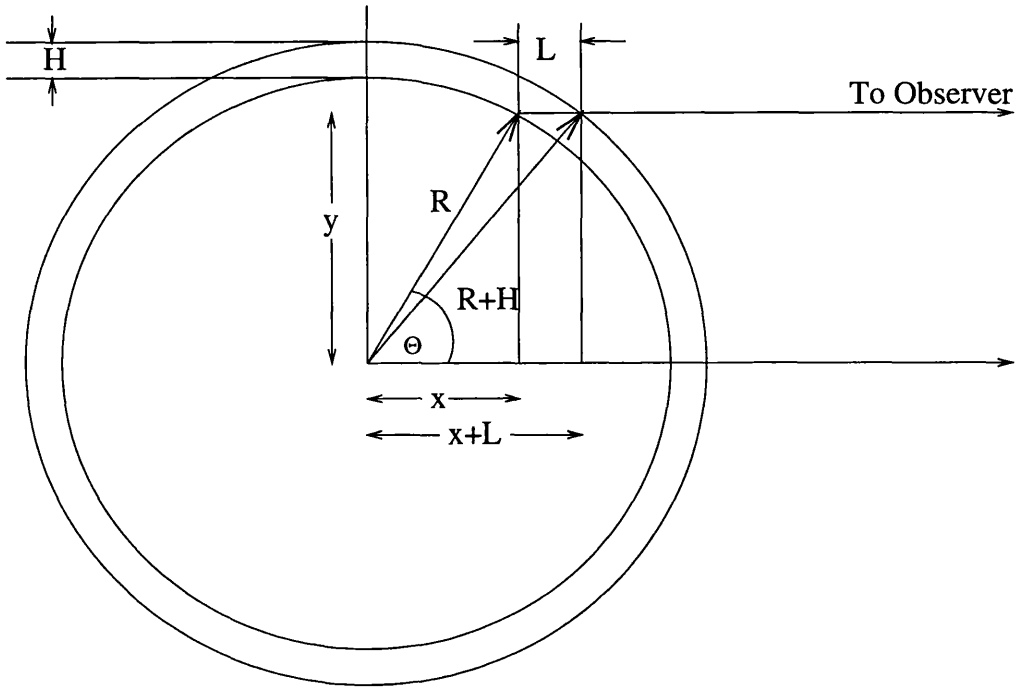

Figure 2.4: Diagram showing how the limb-brightening correction was computed for a point on the disk of the planet. The line of sight ratio is taken to be the ratio of the perceived gas length, **L**, to the gas scale height, **H**. It is assumed that the radius, **R**, has not changed appreciably going from the surface of the planet to the outer edge of the gas layer. Θ is the computed latitude of the desired point on the planetary disk.

2.3 CGS4 Spectroscopy Data

Earlier work by Ballester *et al* (1994) showed that the UKIRT's CGS4 spectrometer more than meets our requirement. The instrumental control and data acquisition software enables the operator to change observing parameters such as wavelength settings and slit orientations relatively quickly so that time lost due to such overheads is less than 20% of total observing time. The instrument is also capable of obtaining spectra at medium resolution (grating mode) and at high resolution (echelle mode). The CGS4DR instrument control and data reduction software allows the observer to automatically reduce the data as soon as it has been acquired.

At the end of an observing run the observer will then have partly reduced data (i.e dark and bias currents subtracted, sky subtracted and coadded) as well as the raw data. Fluxing the spectra may also be done at the telescope. However care needs to be taken over this procedure since it is not all that straightforward (see later).

In collaboration with L. Trafton, T. R. Geballe and G. Ballester, observing time was applied for and was awarded for the nights of the 3^{rd} to the 5^{th} of May 1993. Medium resolution spectra of Jupiter were taken in the K, L and L′ infrared windows along with spectra of the standard star: α-Leo (BS4540, Spectral Class—F9V). Flat and argon arc frames were taken. at various times throughout the observing run. In addition, dark and bias currents frames were taken at the beginning of each night's observing.

Measurements were made using the 150-mm camera and the 150-lines/mm grating in first order giving resolving powers of 1000 and 1300 at 3.4 and 4.0 μm respectively, giving Full Width at Half Maximum (FWHM) of about 3.0×10^{-3} μm (30 Å). Using the telescope in chopping mode each spectrum was obtained by coadding four sets of observations, each set consisting of an exposure on the object and an exposure on a blank part of the sky. Each exposure consisted of six sets of integrations at wavelength positions differing by 1/3 of a resolution element and interleaved together. The total integration time was 4.8 minutes with 2.4 minutes on Jupiter and an equal amount of time on the sky. The length of the slit was 90″ on the sky and we used a slit width of 1″. The projected length of each pixel on the sky was 3.08″. Guiding accuracy was achieved, using the auto guiding

facility of the telescope, to better than 1″. Spectra were obtained with the slit rotated to lie either along the rotational axis or along the equator.

The data acquisition and reduction were automatically performed by the CGS4 instrumental control and data reduction package with the observer indicating to the program what files to use at different stages of observation (Daly and Beard 1992, Wright *et al* 1993). A sample data reduction sequence is outlined in the following (Bailey 1991).

1. Bias frames were coadded and bad pixels masked out. This is then subtracted from all subsequent observations.

2. Dark frames. As above but with bias additionally subtracted out.

3. Flat frames. Added together and bad pixels masked out. A reduced bias frame and a reduced dark frame were subtracted out. For each relevant detector rows a polynomial function was fitted to the data and then divided into the spectrum from that row. The resultant image is a normalised flat field frame.

4. Sky subtraction. The spectra were taken in **chop** mode in which pairs of object and sky integration frames were taken in sequence. Bias and dark currents were subtracted from each integration before the sky frame was subtracted from the object frame. The resultant was coadded to its observational group which, for Jupiter and the standard star, consisted of a set of six integrations at 0.3 s per integration.

5. Flat fielding. The flat field frame was divided into each observational group to remove the pixel to pixel variation.

These steps were set out in an **EXEC** file from which the **CGS4DR** software can access and carry out during the observing run. The reduced spectra are then ready to be fluxed for further analysis. However, as a check, a number of observation groups were selected and re–reduced to confirm that the correct procedures were carried out at the telescope.

2.4 Further Data Reduction

The above data reduction sequence give, as output, flat fielded, sky subtracted and coadded spectral images. The **CGS4DR** software also enable flux calibration to be carried out on the object frames as part of the data reduction procedure. However in the L window the atmosphere has a number of absorption features affecting the spectrum of the standard star (see figure 2.5). A comparison of the H_3^+ spectrum with an atmospheric absorption spectrum provide by the **National Optical Astronomy Observatories** reveals that nearly all of the H_3^+ emission lines are unaffected by atmospheric features. Of the few that are affected by atmospheric absorptions slight modifications can be made to the model to take this into account (see section 2.6.2 H_3^+ Model:- Atmospheric absorption). However the atmospheric absorption will introduce spectral features into the object spectrum if ratioed by the uncorrected spectrum of the standard. Correction is also needed for spectra of the standard taken at 4.0 μm(see figure 2.6) in the L′ window where an absorption feature due to *Bracket-α* is clearly visible. The feature only exists in the spectrum of the standard and therefore does not have any effect on the H_3^+emission from Jupiter.

The procedures to correct atmospheric absorption features are as follow:

1. Extract standard star spectrum from reduced standard frame.
2. Examine for atmospheric absorption and *Bracket-α* features.
3. "Edit" out the features by finding their edges and discarding the data points in between. Care should be taken to make sure that the "edited out" features are due to sources external to the instrument since instrumental function affects all spectra equally.
4. Fit a polynomial to the remaining data points.
5. Divide by a black body function. The photospheric temperature of α–Leo is 6000K.

These step were performed separately from the CGS4DR software using routines specifically written for the task. Descriptions of the programs and some of their functions can

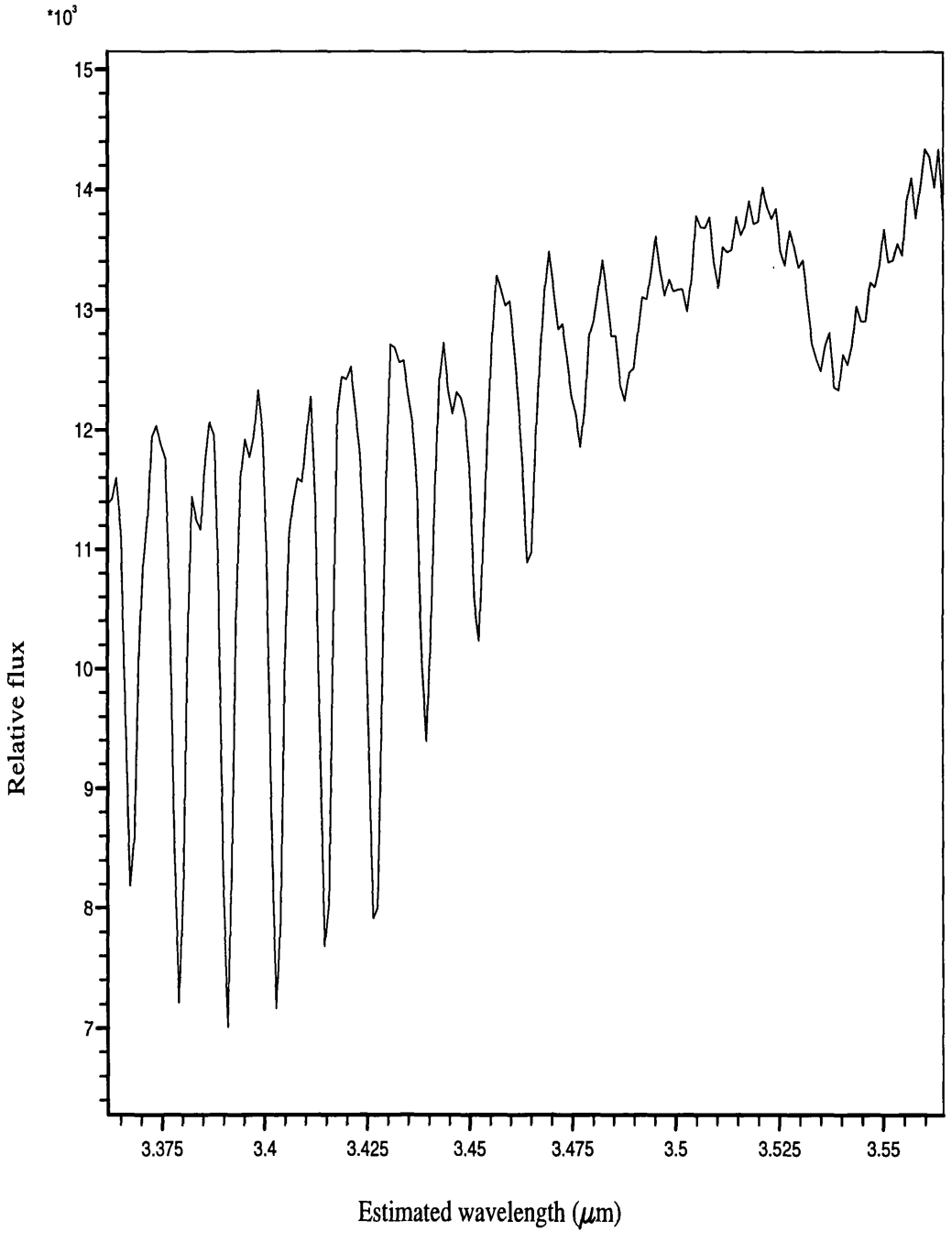

Figure 2.5: Spectrum of the standard taken at 3.5 μm

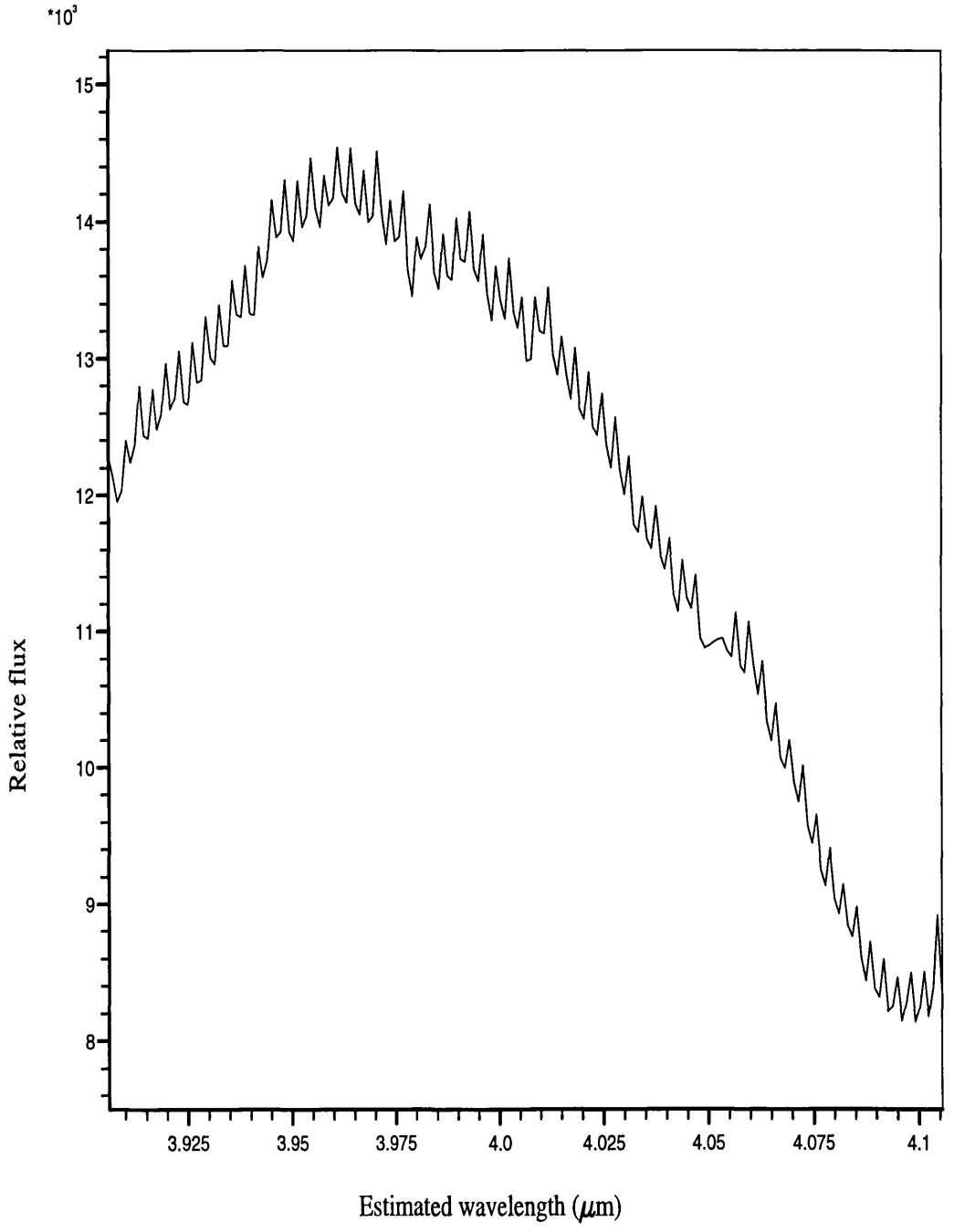

Figure 2.6: Spectrum of standard star taken at 4.0 μm

be found in the **Programs** section later on in this chapter. The corrected spectrum was then copied into other detector rows forming a 2–Dimensional flux calibration frame.

With appropriate scaling, dividing the corrected spectrum of the standard into the object-sky frames will give flux calibrated spectra.

2.5 Spectral Analysis

This section outlines the model and methods used to analyse the spectral data. Least squares and chi squared methods, use in the fitting of data in order to derive temperatures and column densities, are discussed. Two standard deviation and confidence limits methods are used to estimate the range of uncertainty in the fitted parameters and therefore are described.

2.5.1 Theoretical H_3^+ Spontaneous Emission

For a gas in thermal equilibrium the number of molecules, N_i in energy level i is given by:-

$$N_i = \frac{N}{Q(T)}(2J+1)\exp[-E_i/kT] \tag{2.1}$$

where N is the total number of molecules sampled, $Q(T)$ is the partition function, E_i the energy of level i with respect to the ground state and J is the rotational angular momentum of level i. In the case of H_3^+ we must also take into account the spin of the nuclei since this determines whether a particular molecule is in the ortho or para state. Thus:

$$N_i = \frac{N}{Q(T)}(2J+1)(2n_s+1)\exp[E_i/kT], \tag{2.2}$$

where n_s is the spin weighting associated with level i ($1\frac{1}{2}$ for ortho, $\frac{1}{2}$ for para).

The intensity of an emission line due to a transition between upper level i and lower level f is defined as the energy emitted by the source per second and is given by the expression

$$I(\omega_{if}) = N_i h c \omega_{if} A_{if} \tag{2.3}$$

where N_i is the number of molecules in initial state i, ω_{if} is the energy of the wave packet in wave number and A_{if} is the Einstein transition probability of spontaneous emission. Substituting for N_i and normalising per steradian the equation becomes:

$$I(\omega_{if}) = \frac{(2J'+1)(2n_s+1)hc\omega_{if}A_{if}\exp[-E_i/kT]}{4\pi Q(T)}N \tag{2.4}$$

Kao *et al* (1991) published a list of H_3^+ transition intensities, derived from *ab initio* calculations, and their observed frequencies in the laboratory and in space. In the paper they gave, for each line, energy levels, laboratory and space frequencies if the transition has been observed, calculated frequency, upper transition level energy, lower transition level energy and their Einstein-A rate coefficients. The model made use of these values to generate the theoretical H_3^+ spectrum. At the pressure level where H_3^+ is produced on Jupiter, around 10^{-7} to 10^{-9} bar, the emission is optically thin. Thus it is not necessary to consider radiative transfer effects. From earlier studies by Miller *et al* (1991) it was discovered that the *ortho/para* ratio did not vary significantly from 1.0. It was decided that no new information can be gained by fitting this parameter and therefore the *ortho/para* ratio should be fixed at this value for the spectral fittings.

2.5.2 Line Profile

Model functions were convolved with the theoretical spectrum to simulate line broadening due to natural and instrumental effects. Two functions were tried to see how well the line broadening could be simulated.

- The natural and thermal Doppler broadening effects are combined in the Voigt function:

$$H_{(\alpha,v)} = \frac{\alpha}{\pi}\int_{-\infty}^{\infty}\frac{\exp[-(v-u)^2]}{u^2-\alpha^2}du \tag{2.5}$$

  where α is the ratio of the natural or instrumental line width to the Doppler width and v is the ratio of the difference between instrumental wavelength and line wavelength to the Doppler width.

- For a gas at low pressure the molecular velocities has a thermal distribution and is best described by a Gaussian function.

$$a_{(\lambda)} = \frac{1}{\sqrt{2\pi}\delta} \exp[-(\lambda - \lambda')^2/2\delta^2] \tag{2.6}$$

where λ is the instrumental wavelength, λ' is the line wavelength and δ is the Half Width at Half Maximum (HWHM) of the line. Pressure effect on the velocity distribution will be minimal and can be ignored. For the CGS4 spectrometer at medium resolution the instrumental broadening can also be accurately represented by a Gaussian function.

Figure 2.7 shows three theoretical H_3^+ spectra fitted to the same set of 3.45 μmdata. In (**a**) the theoretical spectrum was convolved with a Voigt function. In (**b**) the convolving function was a Gaussian. Finally the spectrum in figure (**c**) was convolved with both the Voigt and the Gaussian. As can be seen from the plots, the Voigt alone function is a poor model for the line broadening, underestimating the intensities on the main body of the emission lines and over estimating for points on the wings of the emission lines. The Gaussian and the combined Gaussian and Voigt functions reproduce the broadening profile very accurately with no significant discrepancy between the model and the data. Although the combined Gaussian and Voigt function was equally good at modelling the data it was felt that the Voigt function added extra complexity to the model, introducing other broadening factors which are not readily detectable in the data. The Gaussian function was finally chosen due to its simplicity and because the instrumental width is broad enough to make the inclusion of other effects unnecessary.

2.6 Characteristics of the Selected Spectral Regions

The two wavelength regions that we selected exhibit markedly different spectral properties. Examples of the 2-D spectral images can be in figures 2.8, 2.9 and 2.10. As well as spectral differences in the two regions, the images also show completely different spatial characteristics, requiring different methods to extract the relevant informations.

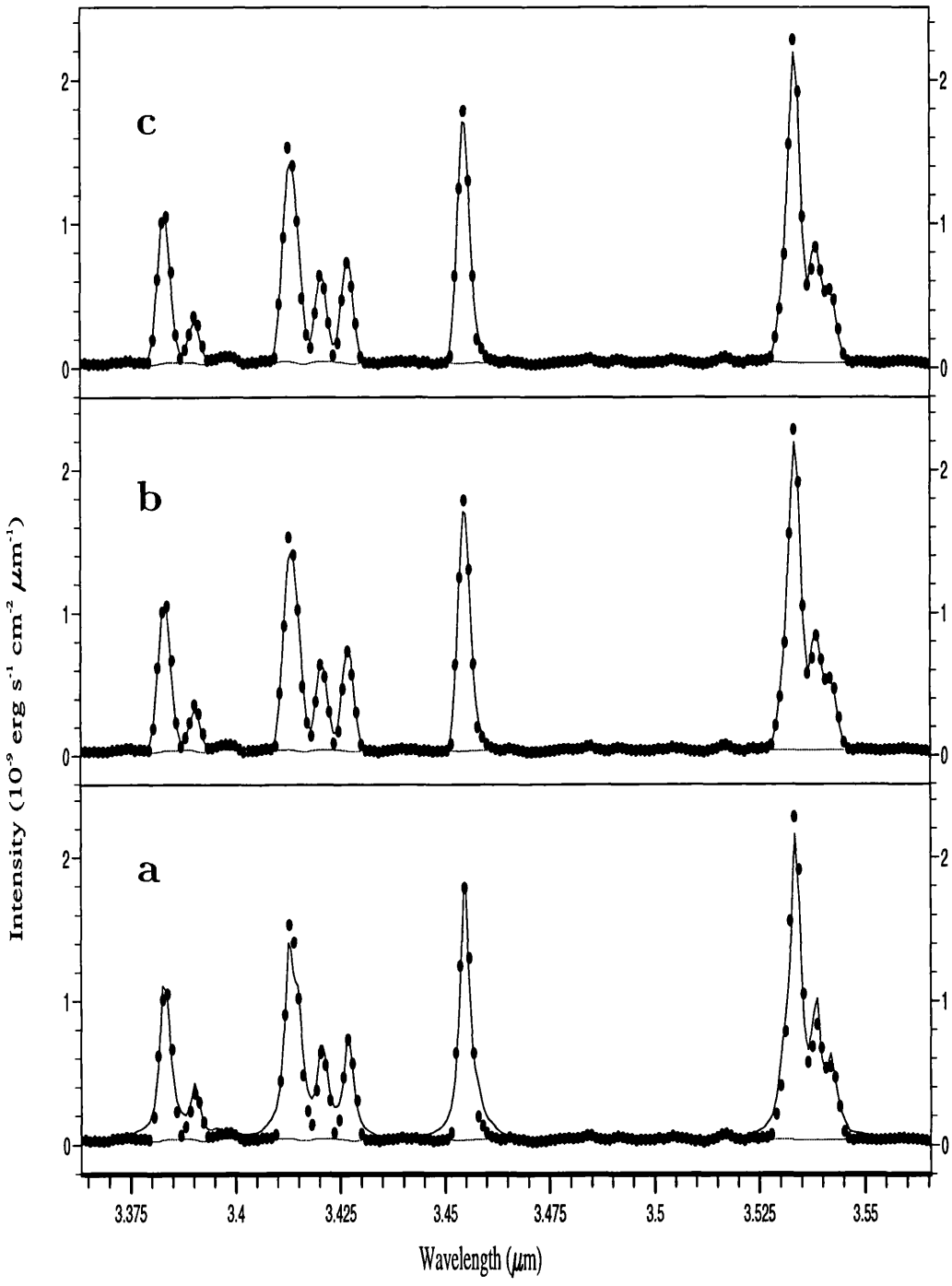

Figure 2.7: Graphs showing a 3.45 μm spectrum fitted using a theoretical H_3^+ emission spectrum broadened by convolving with: (**a**) Voigt, (**b**) Gaussian, or (**c**) combined Voigt and Gaussian profiles.

At 3.45 μm the dominating features of the spectroscopic images are the H_3^+ emission lines which can be seen to extend over the whole of the planet, from north to south (figure 2.8) and east—west (figure 2.9). At this wavelength absorption of solar radiation by the methane cloud layer is almost total, making it particularly favourable for obtaining spectra of H_3^+.

The strongest emissions are found at either of the polar regions, rows 19 and 20 for the north and rows 7 and 8 for the south (figure 2.8). The main generating mechanism of H_3^+ emission here is believed to be charged particle precipitation. The energy deposition due to the precipitating flux is large (10^{13} to 10^{14} W for the FUV emission (Clarke *et al* 1989)) and therefore auroral emission is expected to be the dominant features in the images.

Away from these two regions the intensity diminishes considerably to about 10-20% of peak auroral value, reaching a minimum around the equator. This is typical of all spectral images taken at 3.45 μm. The gradual decrease in intensity towards the equator needs explaining. Outside of the auroral regions H_3^+ is expected to form through the ionisation of H_2 by solar EUV. Geometrically, the intensity of the incident EUV flux is strongest at the equator (neglecting the slight tilt of the equatorial plane with respect to the plane of the ecliptic) and decreases approximately as $1/cos\theta$ where θ is the angle of latitude. However the reduction in incident flux intensity is compensated by an increase in the length of emitting gas column. Since it is generally assumed that H_3^+ is optically thin, the longer gas column length will results in increasing emission intensity to match the reduction in incident EUV flux intensity. The overall effect should be to produce uniform H_3^+ brightness outside of the auroral regions, over the entire planet as viewed from Earth (neglecting the small difference in viewing angle between the Earth and the Sun). That this is not the case is clearly evident from the 3.45 μm spectral image.

Apart from the H_3^+ emission lines there appears to be little else apart from an emission doublet around 3.52 μm which is weak around the poles but increases in intensity to reach maximum around the equator. The doublet was first noted by Ballester *et al* (1994) and proved to be a constant feature in all medium resolution spectra taken at this wavelength region. To date the species responsible for this feature have still not been identified.

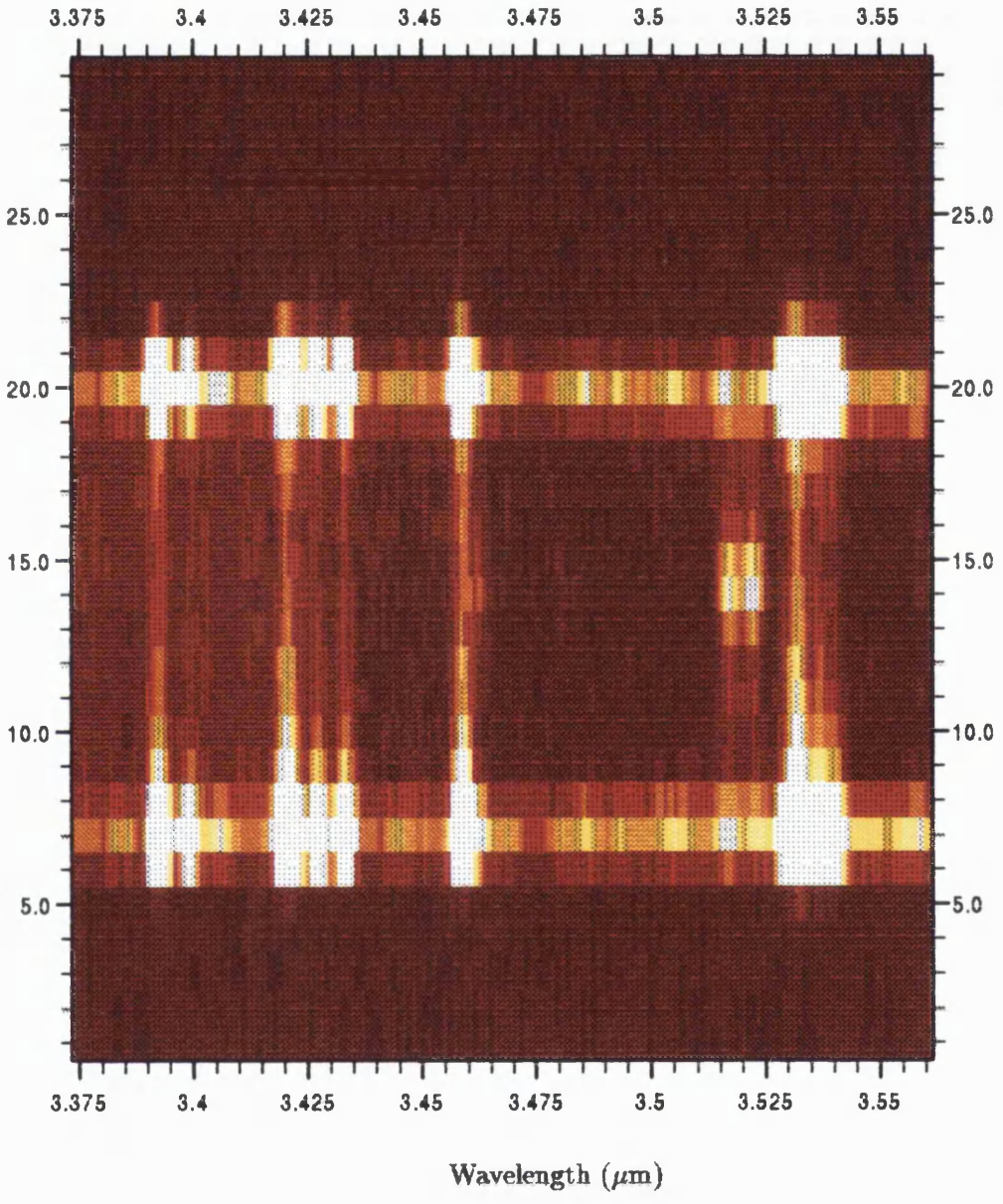

Figure 2.8: An example of a 2-D spectral image taken at 3.45 μm wavelength range. The slit was aligned north—south along the rotational axis. The planet occupies rows 7 (south pole) to 20 (north pole) in the image. A relative intensity colour scale was used for the image.

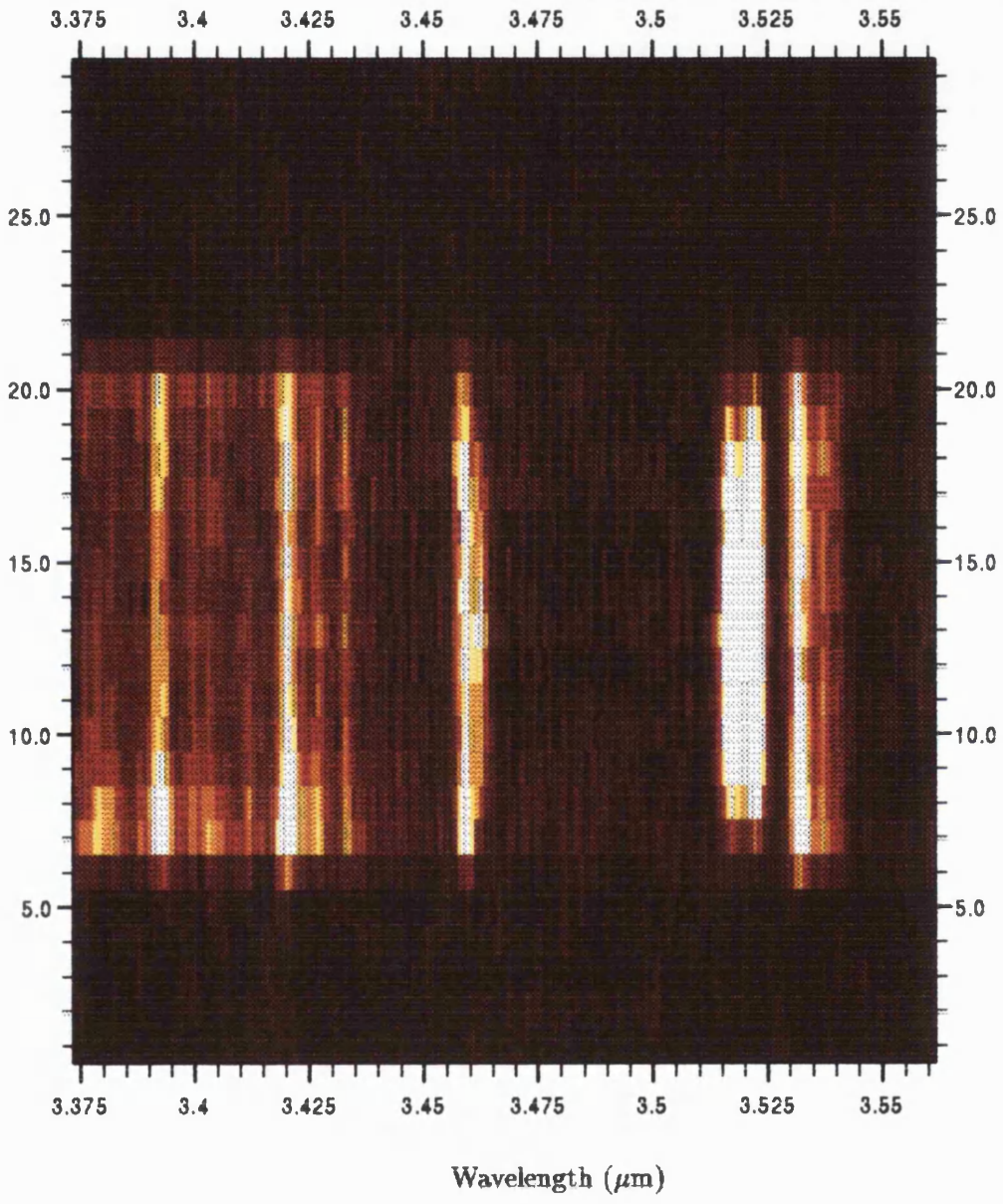

Figure 2.9: An example of a 2-D spectral image taken at 3.45 μm wavelength range. The slit was aligned east—west along the equator. The planet occupies rows 7 (west) to 20 (east) in the image. A relative intensity colour scale was used for the image.

The appearance of the 4.0 μm spectroscopic images is totally different from that of the 3.45 μm (figure 2.10). H_3^+ emission appeared in the images as polar brightening. However, most of the planet is dominated by spectral features resulting from incomplete absorption of solar radiation by the methane layer. Experience gained from the 3.45 μm data suggests that H_3^+ emission from the body of the planet is, at most, 10-20% of auroral intensity and is therefore masked out by reflected sunlight. That H_3^+ is observable at all near the poles is due to the increase in the number of absorbing particles. The spectral features seen clearly on the body of the planet do not entirely disappear at auroral latitudes and therefore have to be taken into account when fitting the H_3^+ spectra.

2.6.1 Background Estimation

The different characteristics of the two selected wavelength regions means that a simple scaled theoretical H_3^+ Spectrum will not be adequate to model the data. Assuming a constant intensity for the background over the wavelength range of the data, excess flux may be attributed to some emission lines and not enough for others. While a flat background is not inappropriate for the aurorae, for spectra on the body of the planet it can give inaccurate values for the fitted temperature and column density. This may be the reason why Ballester *et al* (1994) found the temperature to be higher on the body of the planet than at the aurorae.

A better continuum estimation is obtained by taking out those features which are known to be H_3^+ and fitting a smoothly varying function to the remaining data points. Atmospheric absorption features can be accounted for by dividing an uncorrected spectrum of the standard star into the fitted function. The dependence of the continuum on latitude described earlier, means that this procedure must be repeated for every spectrum taken at 3.5 μm in order to match the latitudinal and temporal variations.

For the fitting of the background in this work a fourth order polynomial was used to approximate the background function. A normalised spectrum of the standard star at 3.45 μm was divided into the polynomial to provide for atmospheric absorption of the continuum.

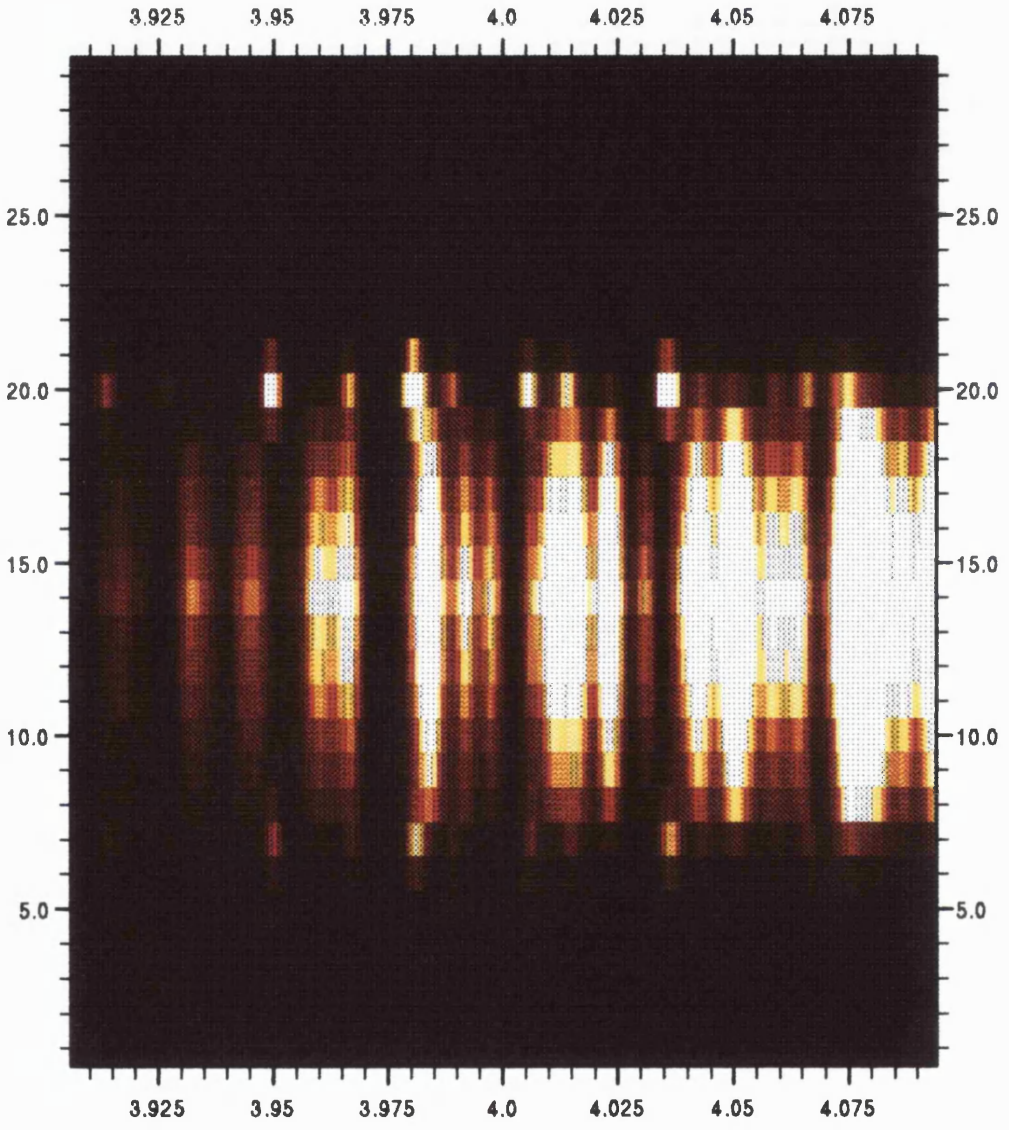

Figure 2.10: An example of a 2-D spectral image taken at 4.0 μm wavelength range. The slit was aligned north—south along the rotational axis. The planet occupies rows 7 (south pole) to 20 (north pole) in the image. A relative intensity colour scale was used for the image.

Figure 2.11 shows two fits to a spectrum obtained at the jovian equator. In (**a**) the spectrum was fitted using a constant background. In (**b**) a fourth order polynomial was fitted to the data points outside of the H_3^+ emission lines. The polynomial function was then convolved with an uncorrected spectrum of the standard star to provide for atmospheric absorption of the jovian continuum. The resultant was then used in the fit as an estimate of the continuum level. Although the standard deviation does not differ greatly between the two, the top spectrum gives a more accurate fit to the data. It results in lower temperature than the fit using a constant background.

For spectra taken at 4.0 μm a different approach to estimating the continuum was required. As have been pointed out earlier methane absorption of the incident solar radiation is not nearly as efficient as that at 3.45 μm. Although the intensity of the reflected flux varies with latitude, the continuum profile remains constant as a function of temperature. With suitable scaling therefore, a spectrum from the body of the planet can be used as the background level for the observed H_3^+ spectrum in the auroral regions.

Figure 2.12 shows a fitted 4.0 μm spectrum of the northern aurora (longitude 160 λ_{III}) extracted from the same image seen in figure 2.10. The estimated background was extracted from a row on the body of the planet, two rows away from northern aurora.

2.6.2 Atmospheric absorption

The theoretical H_3^+ spectrum was checked against an atlas of the Solar spectrum, provided by the National Optical Astronomy Observatories (NOAO) at Tucson, Arizona, to see if any of the H_3^+ frequencies coincide with atmospheric absorption features. Almost all were found to lie in regions free of atmospheric components. The lone exception was a line at 2930.169 cm^{-1} (3.41277 μm) where the atlas shows a strong but narrow absorption feature. For this an absorption factor was introduced into the program and manually adjusted to account for the reduction in line intensity. The theoretical spectrum was then fitted to a number of spectra with the 2930.169 cm^{-1} line reduced by zero, twenty and forty percent of its maximum theoretical value. Figure 2.13 shows the three theoretical spectra fitted to the same set of data. The standard deviations show that the best result

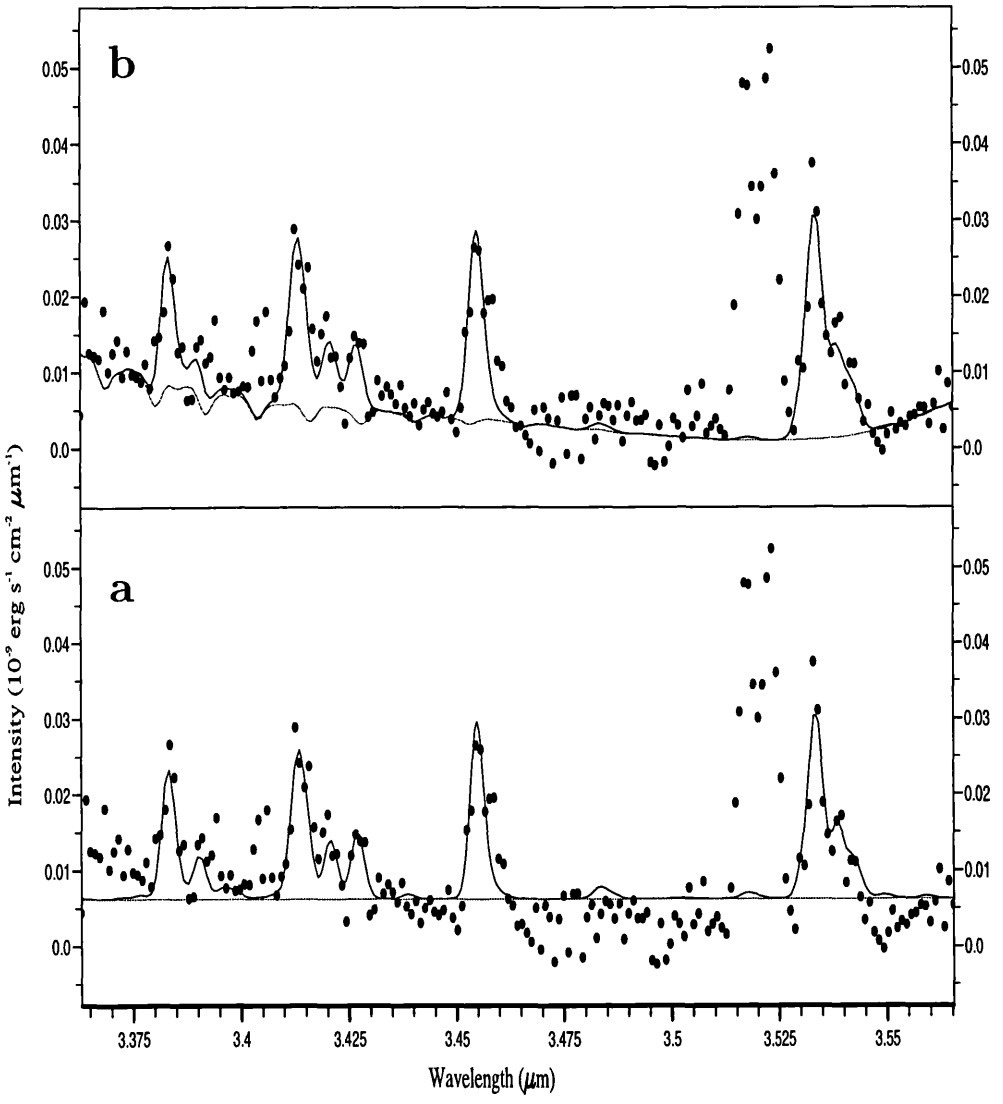

Figure 2.11: Two spectra fitted to the same set of data. In the first the continuum was assumed to be constant at all wavelength, in the second a polynomial convolved with an uncorrected spectrum of the standard star was used as an estimate of the background level. The fitted temperatures and column densities are 1230K and 0.181 mol m^{-2} for the first, 974K and 0.565 mol m^{-2} for the second. The standard deviations are 0.00386 and 0.00344 respectively.

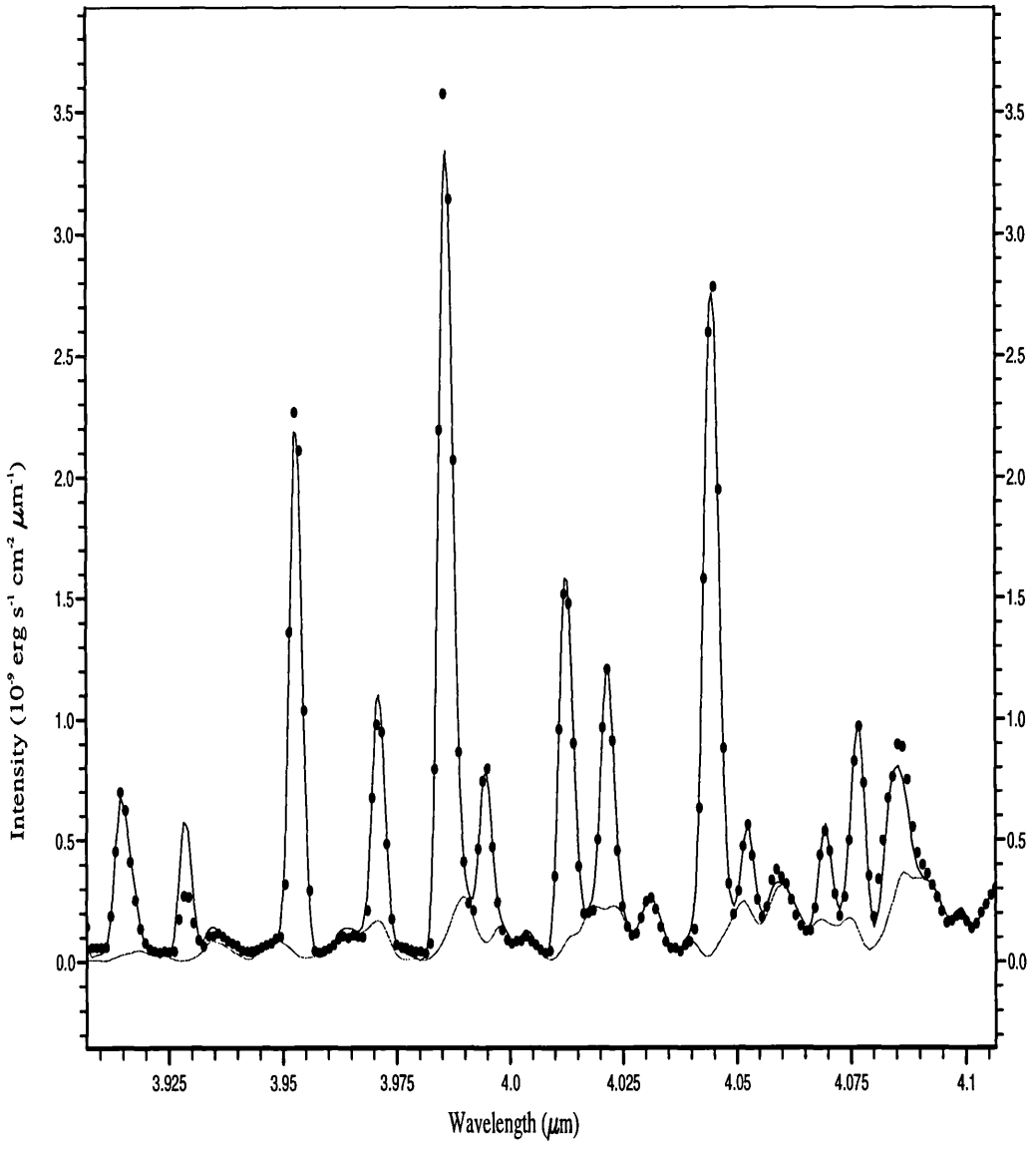

Figure 2.12: Fitted 4.0 μm spectrum of the northern aurora extracted from the spectral image seen in the previous figure. The background used was a scaled spectrum from the body of the planet.

was achieved with the line reduced to 80% of its full intensity, and this value was used in all subsequent fitting.

2.6.3 Fitting Spectra

Unweighted least squares analysis was initially used to derive temperatures and column densities from the spectral data. Least squares is defined as minimising the value of S, given by:

$$S = \sum_{i=1}^{N} (D_i - M_i)^2 \tag{2.7}$$

where D_i are the data points and M_i are the values predicted by the model.

The fitting program required initial guesses of the model parameters to be supplied. The fit to the data was achieved by varying the model parameters to find the minimum value of S. The fitted spectrum was then examined for discrepancy in the wavelength scale and a linear adjustment made if that was found to be the case. The spectrum was then refitted and the new standard deviation compared with the previous one. The procedure was repeated until the standard deviation could no longer be minimised.

For each image, spectra from the relevant rows were extracted and the fitting procedure above was applied to determine the temperatures and column densities. Estimates of the range of uncertainty in the fitted values were obtained by alternately holding the temperature and column density fixed at the best fitted value and then vary the other until the standard deviation doubled.

Preliminary results showed that there is considerable anti-correlation between the fitted temperatures and column densities. This is due to the limited wavelength range of our spectra. Any changes made to either parameter away from the best fitted value induces changes in the other which does not result in a significant increase of the standard deviation. The 2–σ deviation method of estimating the uncertainty ranges does so for one parameter at a fixed point of the other (taken to be the best fitted). The method, therefore, does not have the capability of determining the uncertainty ranges when both parameters are assessed jointly. The implication of this is that the 2–σ method of deter-

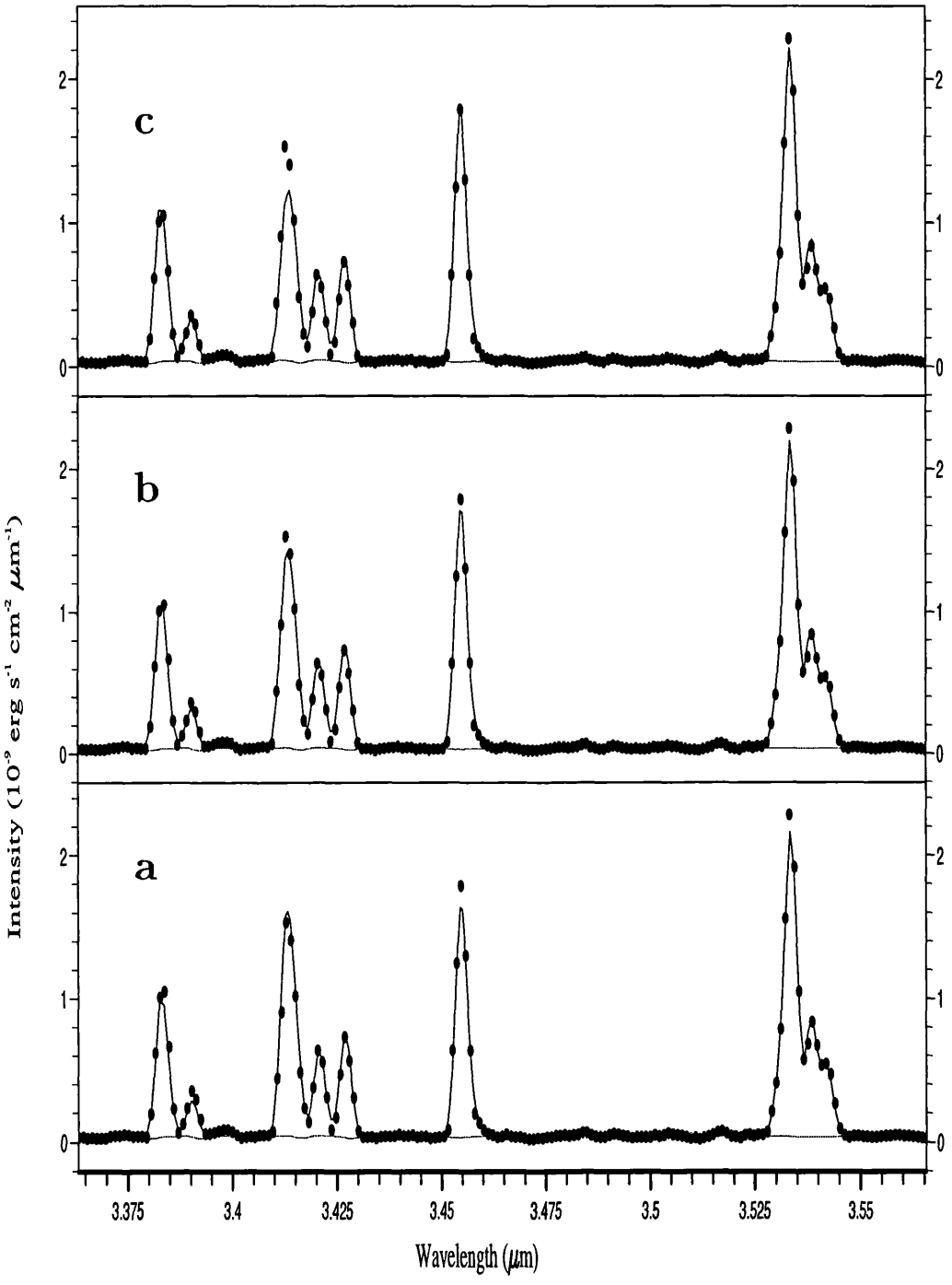

Figure 2.13: Graphs of three theoretical spectra fitted to the same data set. Atmospheric absorption of the 2930.169 cm^{-1} (3.41277 μm) line were set at 0, 20% and 40% for graphs shown in **a, b** and **c** respectively. The standard deviations are .03878, .03126 and .05118 for **a, b** and **c** respectively.

mining the errors may seriously underestimate the range of values the two together can take. More complete discussions on the matter may be found in papers by Cline and Lesser (1970), Lampton *et al* (1976), Cash (1976) and Avni (1976).

If the errors are known for each of the data points then the χ^2 method maybe use in the fitting. Chi squared and reduced chi squared are defined as:

$$\chi^2 = \sum_{i=1}^{N} \frac{(D_i - M_i)^2}{\sigma_i^2} \tag{2.8}$$

and

$$\begin{aligned} \chi_\nu^2 &= \frac{\chi^2}{\nu} \\ &= \frac{\left[\sum_{i=1}^{N} \frac{(D_i - M_i)^2}{\sigma_i^2}\right]}{\nu} \\ \nu &= N - m \end{aligned} \tag{2.9}$$

where σ_i is the error associated with the data point D_i, ν is the degrees of freedom and m is the number of parameters being jointly estimated. This is preferred over least squares since the fit is weighted by the individual variances. The ranges of uncertainty for each of the relevant parameters may be estimated by applying the confidence limit test. More complete treatment of the technique can be found in texts by W.H. Press, B.P. Flannery, S.A. Teukosky and W.T. Vetteling (1986), P.R. Bevington (1969) and other works on statistical analyses. A brief account only will be given of how the method was applied here to determine the uncertainty ranges for the fitted temperature and column density.

The procedure is to obtain the best fit model to the data by varying the parameters and minimising the value of χ^2. A grid of points in the joint parameter space of interest is generated and the model fitted to the data at each of the nodes by varying the remaining parameters. The ranges of uncertainty are then estimated by drawing contours of χ^2 values at the desired confidence levels. The boundary of the contours encloses regions having certain probabilities, depending on the confidence levels of the contours, containing the true parameter values.

For the CGS4 observations the errors on the individual data points were assumed to

be dominated by Poisson statistics, taking the instrumental noise to be negligible. For photon counting the error, σ, on the total number of photons counted is:

$$\sigma_N = \sqrt{N} \tag{2.10}$$

For the reduced spectra in which thermal emission from the atmosphere has been subtracted out the error will be

$$\begin{aligned} \sigma_{(N_o - N_s)} &= \sigma_{(N_o + N_s)} + \sigma_{(N_s)} \\ &= \sqrt{(N_o + N_s) + N_s} \\ &= \sqrt{N_o(1 + 2\frac{N_s}{N_o})} \\ &= \sigma_{(N_o)}\sqrt{1 + 2\frac{N_s}{N_o}} \end{aligned} \tag{2.11}$$

where N_o is the number of counts from the object and N_s is the number of counts from the sky.

Therefore taking the square root of the number of counts in the reduced spectra and multiplying by the factor $(1+2(N_s/N_o))^{1/2}$ the errors on the individual data points maybe deduced to a good approximation. In the infra–red, the thermal emission from the atmosphere is high. For short integration times the sky flux maybe comparable to the flux coming from the object itself. This has been confirmed by examination of images taken at this wavelength. Thus it is reasonable to set the N_s/N_o ratio to 1.

Figure 2.14 shows a contour diagram used to estimate ranges of values that the temperature and column density may jointly take that will reproduce an acceptable theoretical spectrum. The contour is drawn at the 99.9% confidence level (corresponding to the 2–σ level) which encloses a very long and narrow region extending to greater than eight times the fitted column density but within a small (relatively) temperature range. This clearly shows that the two are very strongly coupled. According to B. M. Dinelli (private communication) the two maybe be correlated to $> 99\%$. Therefore, we cannot be truly confident of fitting the temperature and column density independently for the wavelength ranges

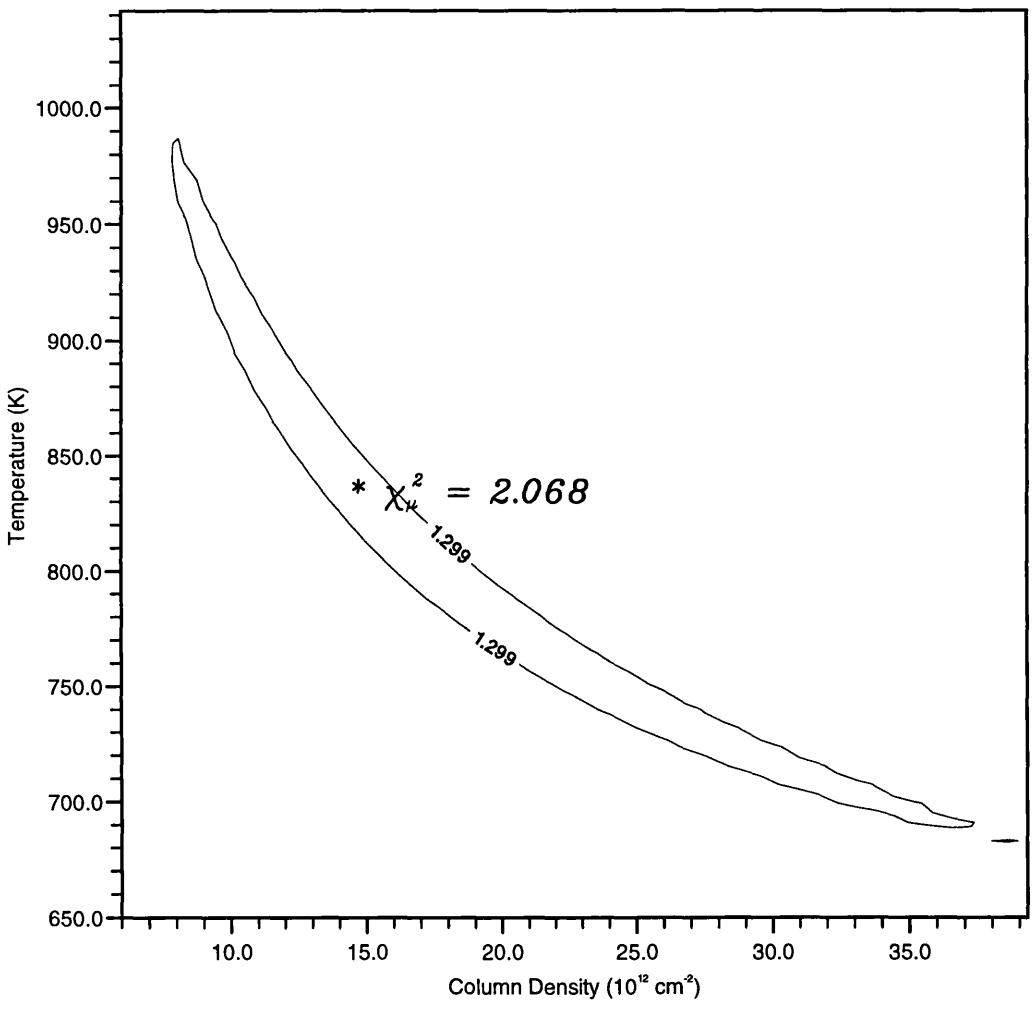

Figure 2.14: Contour diagram used to estimate the uncertainty associated with fitted temperature and column density. The contour is drawn at 99% confidence level for 140 degrees of freedom.

of our spectra. As our wavelength range improves so the temperature, column density correlation will go down. With infinite wavelength coverage we should be able to separate them almost completely. The method demonstrates that error estimation using the 2–σ procedure severely underestimates the size of the errors for this data set.

Clearly joint parameter estimation will not, in this case, yield conclusive results with regards to the variability of the H_3^+ emission. In this respect the 2–σ uncertainty estimation may be more useful in gaining information about the physical conditions of the H_3^+ layer, bearing in mind that the ranges of uncertainties for one parameter was estimated at a fixed value of the other.

Given the strong coupling between the temperature and column density, we now outline a method of combining the two to compute the total H_3^+ emission and thus give useful information on the distribution of H_3^+. Figure 2.15 shows a graph of emissivity against temperature for a single H_3^+ molecule assuming a thermal distribution. For each spectrum the graph was used to determine the emissivity for a single molecule at the fitted temperature. This was then multiplied by the fitted column density to obtain the total emission parameter. This parameter was found to be stable to within $\pm 20\%$ for bright auroral spectra and to better than $\pm 50\%$ for spectra near the jovian equator, over the range of temperature and column density parameters given by the 99% confidence contour. A discussion of the validity of using this parameter is reserved for the chapter dealing with the spectral results.

2.7 Program Suites

2.7.1 Limitation of Available Packages

Monitoring the jovian ionosphere involves a campaign of observations over a long period of time. The data obtained consist of both camera images and long–slit spectral images, both of which need considerable processing before they can be analysed. The use of H_3^+ as a probe of ionospheric conditions means that the procedure for fitting and analysis of spectra has to be repeated again and again. Having the ability to do quick analysis on the data

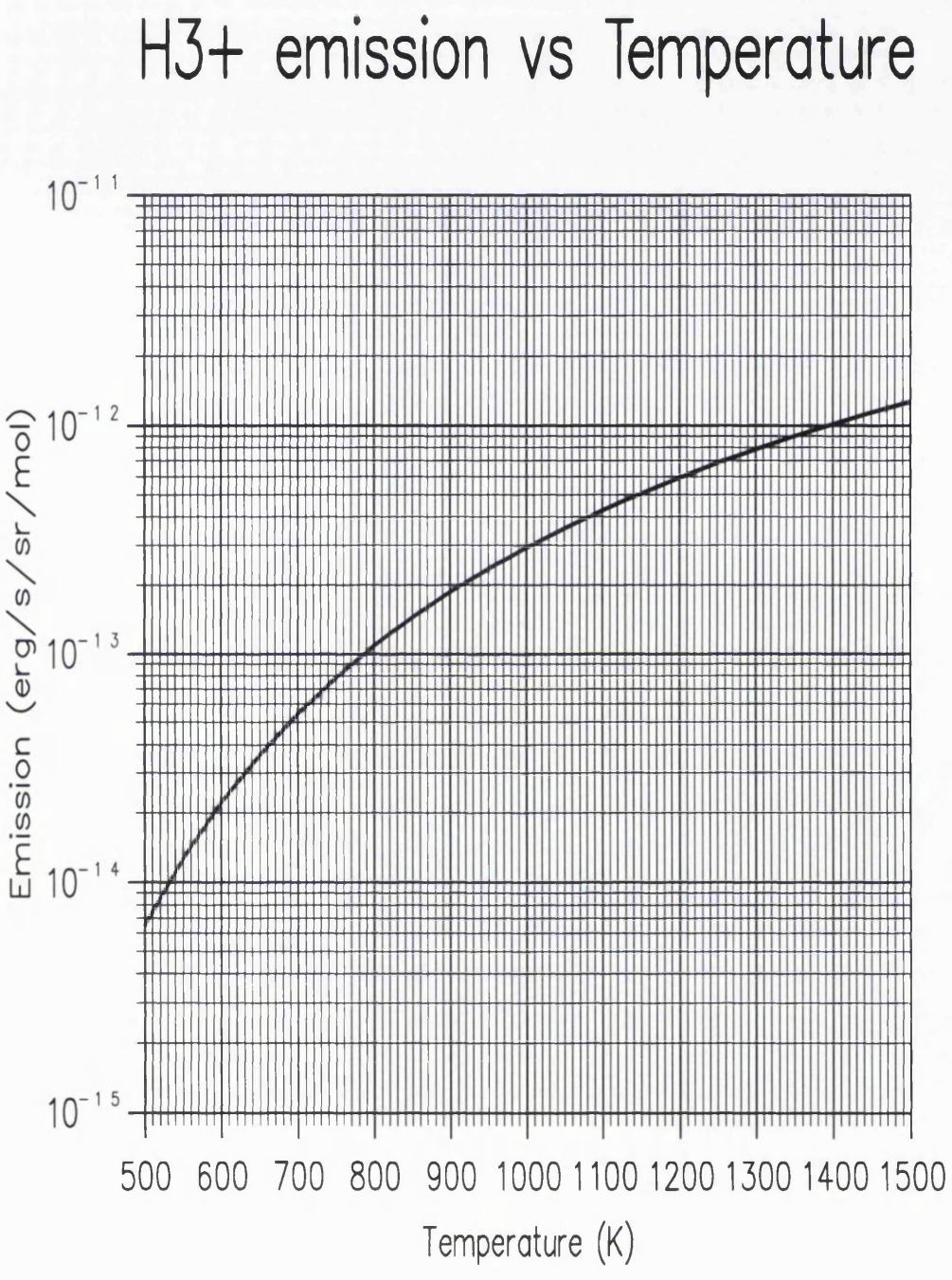

Figure 2.15: Graph of emissivity per molecule of H_3^+ versus temperature. The values are plotted on a logarithmic scale.

obtained during an observation run enables the observer to alter the observing schedule as dictated by the results. Telescope time can then be better utilised to concentrate on areas most profitable for a particular observing night. Further analysis, performed away from the telescope can also be guided by the preliminary results and then refined according to the available resources.

We therefore investigated to what extent the aims above can be carried out with the existing resources. Both of the **IRTF** and **UKIRT** (used to obtained the data in this work) already provide access to data reduction packages. These maybe be used in the initial stages of the data reduction, i.e. subtracting out the dark and bias currents, flat field images, correct bad pixels, etc. However, reducing all available data within the observing time may not always be possible. Further data reduction is therefore needed, carried out away from the telescope.

At the present time a number of data reduction packages are available to the astronomical community. The user may choose from comprehensive packages such as **IRAF**[1] and **FIGARO**[2] or specific packages such as **CGS4DR** which deals only with data from the CGS4 spectrometer. **IRAF** is a large UNIX based package that allows for complex data reduction and image manipulation. However it requires considerable effort from the initial installation to maintenance which may ideally be provided by large research groups with their own computer support staff. **FIGARO** is only released through **STARLINK** and mostly used by UK based astronomers. It carries most of the tasks that **IRAF** is capable of and is more familiar to a majority of UK astronomers. The disadvantage is that it has only recently been ported to UNIX platform from VMS — too late for it to have been used in this work — and some problems still need to be sorted out.

At the start of the project the only access to data reduction packages was through **STARLINK** which provided **FIGARO** running on a number of DEC MicroVaxes workstations. The system had a large number of users and data storage space was severely limited. At the same time an IBM RS6000 workstation running the UNIX operating system was available for computation and data analysis. The machine was significantly faster

[1] Released through and supported by NOAO

[2] Released to and supported by STARLINK

in terms of computing speed and it also had a large amount of available data storage space. However, a data reduction package was not provided with the machine and the purchase and maintenance costs meant that it was not feasible to obtain one. Since most of the data were already partially reduced at the telescope further complex data reduction was not required. However none of the available packages were suitable for the particular analysis we wished to perform, which concentrated on the morphology and physical conditions of the H_3^+ emission regions. The decision was therefore made to write a number of basic data image handling and spectral analysis programs to run under a UNIX environment.

2.7.2 In-House Program Suites

A set of in-house programs was developed and tested to manipulate and view the data. Most of the programs use **UNIRAS** graphical routines to make shaded contour plots of the images or display the data graphically. All programs read the file names as part of the command line. If the names are not given then the programs will prompt for them. A search is made for the files in the directory where a particular program was started. If the files are not found then a prompt is made for the full path name of the directory where the files are kept. Then, if the files are still not to be found, the program will exit and print a warning message.

Image Arithmetic

The following programs allow the user to perform rudimentary arithmetic operations on data images. All data images must be consistent with one another, i.e. have the same array dimensions. For more sophisticated operations the user should refer to data reduction packages such as **IRAF**, **FIGARO**, etc... which provide these and many more. The programs in this set are **add, subtract, multiply, divide**.

Viewing Images and Spectra

The following programs allow the user to view an image as colour shaded contour plot or as histograms of pixel values in the x/y directions. The programs may only be run on a

UNIX workstation with a display capable of handling X windows. The viewing programs are **view_image** and **view_spectrum.**

Image Manipulation

Images taken at the telescope maybe stored in a number of orientations. The images may also contain large parts that are not required when they come to be analysed. The following programs allow the user to trim and rotate the images taken at the telescope to the desirable size and orientation for storage, display and spectral fitting purposes. They are: **trim_image** and **rotate.**

Wavelength calibration

For extended objects, such as Jupiter, spanning several detector rows, the optical distortion is inherent in the spatial information.

To analyse the data it is required that each data point has a wavelength associated with it. Spectra of extended objects such as Jupiter span several detector rows which may differ slightly in their wavelength scale due to possible optical distortion in the instrument.

A program was developed to calculated the wavelength scales for a number of detector rows spanning the relevant region of the image. A second order polynomial is fitted to the selected rows in order to calculate the dispersion for other parts of the image. The program is accessed by giving the command **wavecal.**

Flux Calibration

Spectra of standard stars are usually taken throughout the observing run in order to calibrate the flux coming from the object. In the infra–red this flux is attenuated by absorption in the atmosphere, imposing features onto the standard spectra. These need to be "edited" out otherwise features will show up in the object spectra that does not originate from the object itself. For most observation of the standard stars its spectrum is contained in one or two rows at the most. To flux calibrate extended objects the standard spectrum needs to be extracted and then copied into other rows provided their wavelength

scales does not differ too much from the one the standard is in. To prepare a flux calibration spectrum from a spectrum of a standard use the command **prepare_standard**.

Black Body

Spectra of standard stars are usually assumed to be black body functions at particular temperatures. This implies that the observed fluxes at different wavelengths vary depending on the effective temperature of the standard star. The variation maybe taken out of the standard spectrum by dividing by a theoretically generated spectrum of a black body at the coronal temperature of the star. The command to used is **black_body**.

Fitting

This spectral fitting program was adapted from a routine written by Steven Miller. This was designed to fit CGS4 spectra obtained using the 150 l/mm grating. In Miller's routine the spectrum has to first be extracted from the 2-D images and then convert into ascii using **FIGARO**. The process involved creating a smaller file for each spectrum extracted from the images. With the limited diskspace available on the **STARLINK** system, extracting spectra from more than two images and keeping them on disk until they have been fitted was not a feasible option, and therefore a new routine was written.

The fitting program described in this section uses UNIRAS graphics routine to make contour plots of the 2-D spectral images from which the appropriate spectrum can be selected and fitted within the program itself. An option is available to test for the range of uncertainties in the fitted temperature and column densities.

To run the program the user must provide a number of files supplying the line frequencies, Einstein A–coefficients, energy levels of all available transitions and a wavelength scale. A data file containing various parameters and information about the image to be used in the fitting must also be supplied. Examples of the required files are shown in tables A.1 and A.3. The wavelength scale maybe obtained by using the **wavecal** program described in the previous section.

The fitting program consists of a number of tasks. Commands to perform the tasks

are **efit, extract_background, cgs4_fit**. Descriptions of the commands are outlined in the appendix.

Image Analysis

To analyse the reduced ProtoCam images a program was needed to plot the images and overly them with various features such as a grid of longitudes and latitudes, footprints of the Io plasma torus and auroral boundaries. Images will also be needed to be pieced together to produce a mosaic of either aurorae since the field of view of ProtoCam at its highest spatial resolution (0.25″), is not wide enough to encompass the whole of one aurora in a single image. The command to carry out this task is **mkpict**.

Chapter 3

Imaging the Jovian Aurorae

Results from the analysis of the ProtoCam images obtained on the 22nd and 23rd of April 1993 are reported in this chapter.

The results of the limb fitting and limb brightening–correction are shown in figures 3.5 to 3.16. The limb fitted images are shown paired together with their limb-brightened corrected counter parts. Lines showing the Io torus footprint (outer dashed line) and the footprint of the LCFL are drawn on top of the images to aid interpretation.

3.1 22rd April 1993

On this night we sampled the aurorae at CMLs 342° to 111°.

3.1.1 Northern Aurora

Most of the uncorrected images (figures 3.1, 3.2 and 3.3) show a relatively dim aurora covering only a small area of the pole. Only in the last image could significant structure of the aurora can be detected. In nearly all of the images of the northern hemisphere H_3^+ emission is seen mainly off the limb of the planet and very little inside the planetary disk. At these longitudes (CMLs 342° to 111°) the Io torus footprint and the LCFL footprint are at their highest latitudinal range.

In the last image, figure 3.4, auroral emission is seen confined to within the Io torus

footprint. The emission filled most of the auroral region apart from an area of relative null beginning at longitude 150° and extending almost to the eastern limb of the planet. There is a faint spot seen between the Io torus footprint and the footprint of the LCFL which appears to be connected to the main auroral emission by a faint arc running above the limb of the planet.

The limb brightening corrected images shows that between CMLs 342° and 33° the northern auroral appears very faint almost indistinguishable from the continuum emission. Only in the last image does there appear to be any significant auroral activity. The emission shows up as a large bright area beginning at the western limb of the planet and terminating around longitude 150°. From there a region of H_3^+ emission null extends all the way to the eastern limb.

The apparent lack of emission above the limb of the planet after correcting for the line of sight effect may be due in part to an over correction of the intensity. As was mentioned in chapter 2 the line of sight correction model used here does not, at the present, take into account the size each pixel subtend at the planet's surface. For pixels at the edge or just above the emissions may not completely fill the field of view of the pixel and therefore the large correction factor advocated here may not be appropriate. A correction model taking into account the size of the pixels will need to be used to determine accurately how much is being emitted at high altitudes.

3.1.2 Southern Aurora

At these longitude ranges, from 352° to 98°, the southern aurora offers a favourable viewing geometry according to the footprints of the magnetic shells 6 and 30 R_J. The emission is mostly confined to a region above the LCFL footprint. Nearly all of the images show a large bright area on the western limb connected by a diffuse arc of emission to a smaller spot on the eastern limb (figures 3.5, 3.6 and 3.7).

Almost all of the images show an area of emission null, extended in longitude, starting at around longitudes 0° to about 60°. The last image, figure 3.8, shows that this area extends around the whole planet as far as 188°, the last longitude in the range to be visible

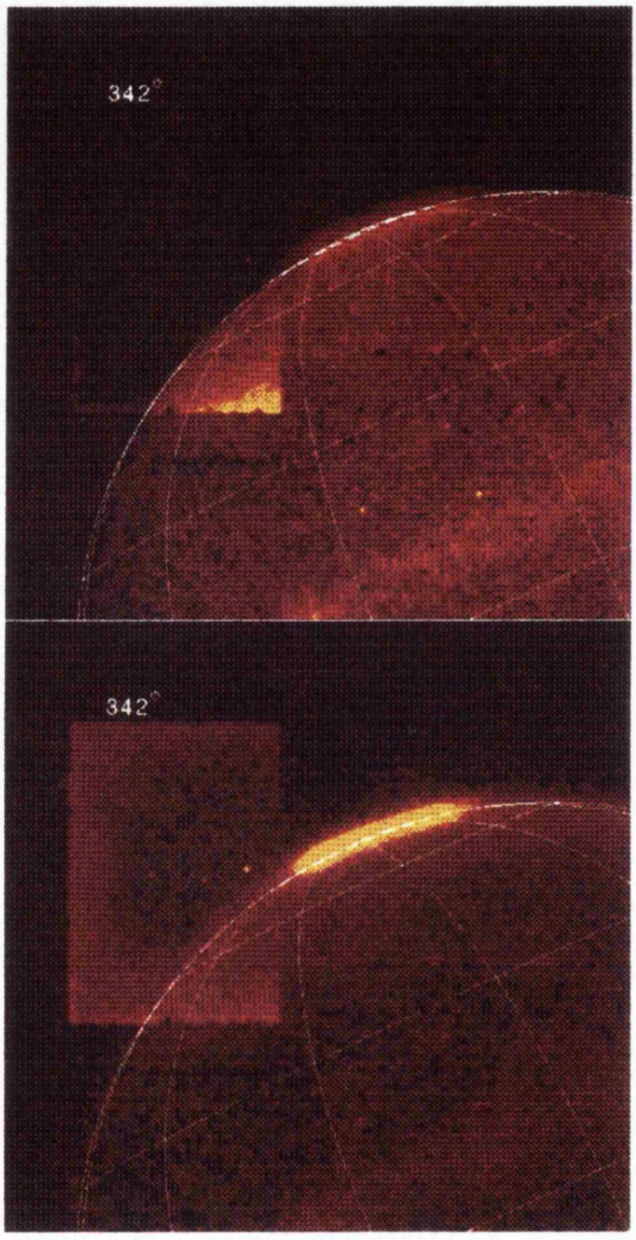

Figure 3.1: Images of the H_3^+ north aurora taken at 3.533μm. Footprints of the IPT and the LCFL, according to the O_6 model, are shown on the images as dashed lines. The CML is given in the top left hand corner of each image. The limb-brightened corrected image is shown at the top.

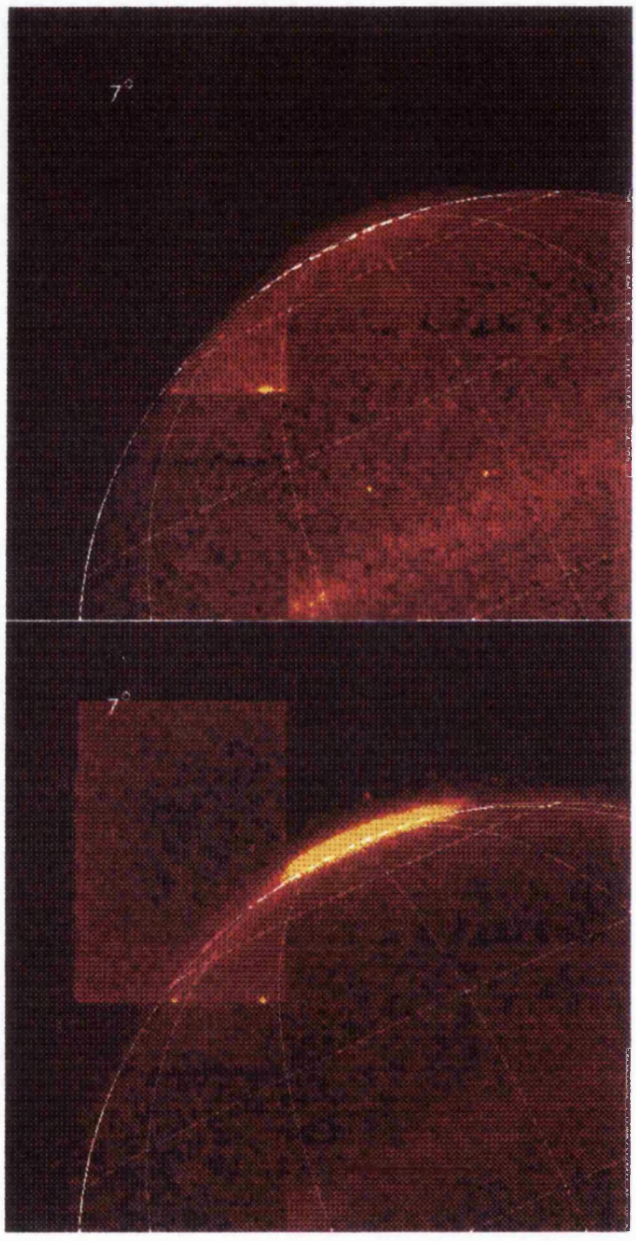

Figure 3.2: Images of the H_3^+ north aurora taken at 3.533μm. Footprints of the IPT and the LCFL, according to the O_6 model, are shown on the images as dashed lines. The CML is given in the top left hand corner of each image. The limb-brightened corrected image is shown at the top.

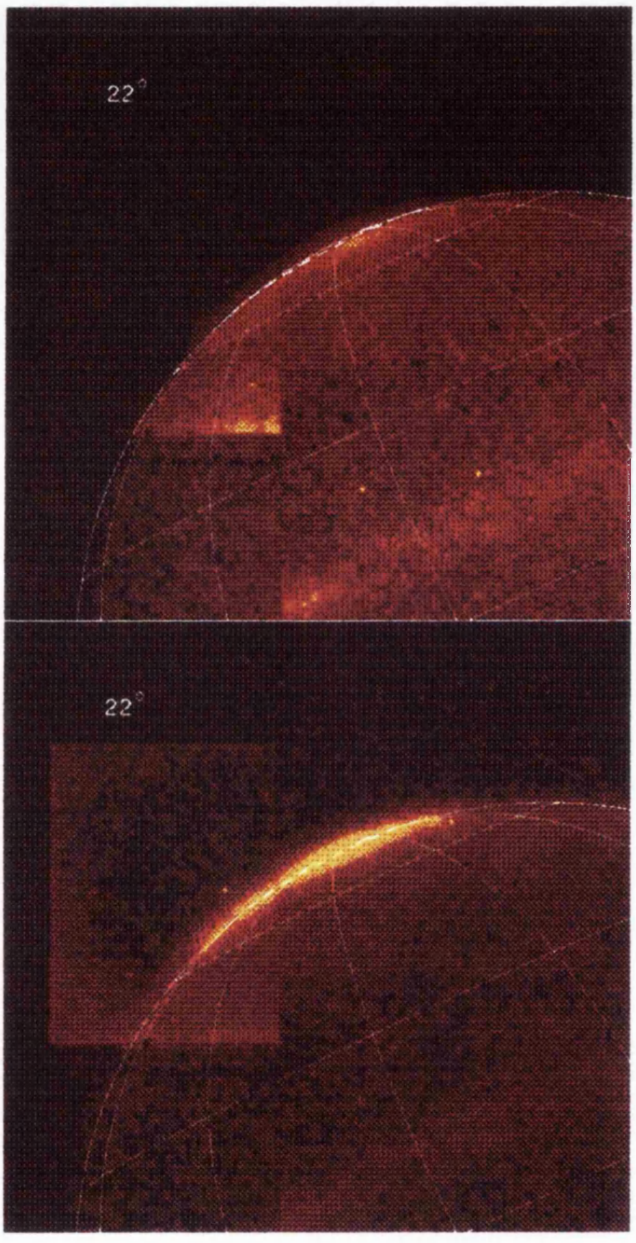

Figure 3.3: Images of the H_3^+ north aurora taken at 3.533μm. Footprints of the IPT and the LCFL, according to the O_6 model, are shown on the images as dashed lines. The CML is given in the top left hand corner of each image. The limb-brightened corrected image is shown at the top.

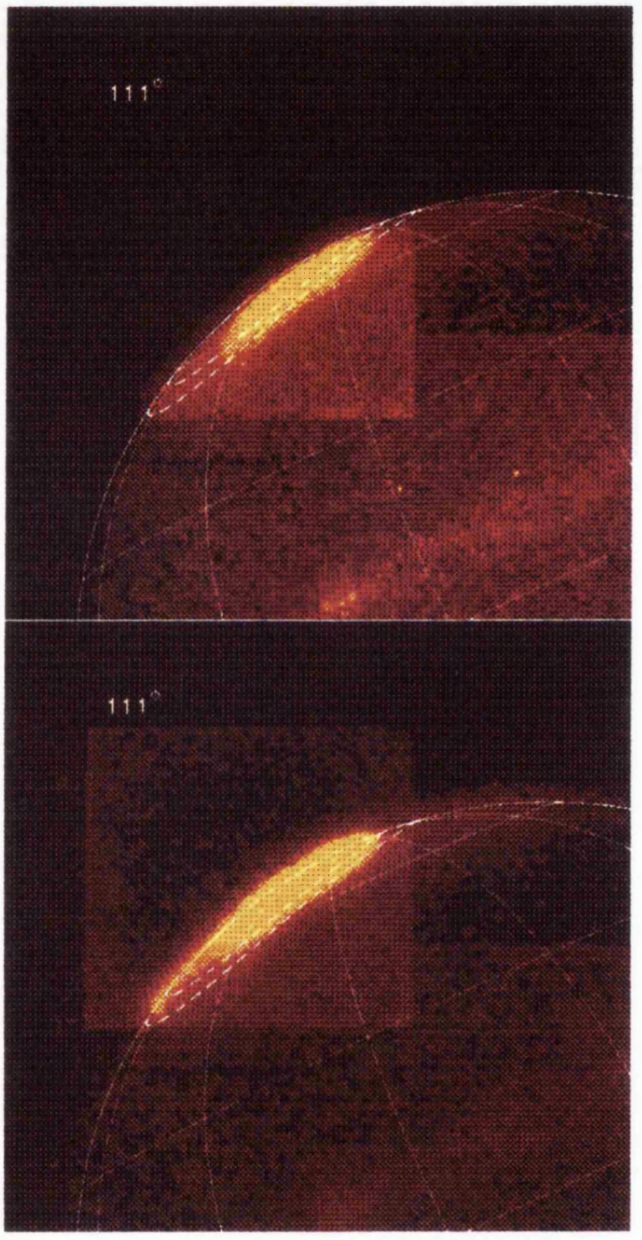

Figure 3.4: Images of the H_3^+ north aurora taken at 3.533μm. Footprints of the IPT and the LCFL, according to the O_6 model, are shown on the images as dashed lines. The CML is given in the top left hand corner of each image. The limb-brightened corrected image is shown at the top.

in these images.

The limb brightening corrected images taken at CMLs 352° to 33° all show a large bright area of emission beginning at around longitude 300° and extending to about 60°. All images show what appear to be sections of an oval surrounding the pole and connecting to the area of bright emission.

3.2 23rd April 1993

The CMLs sampled on this night range from 83° to 250°.

3.2.1 Northern Aurora

In the north polar region, the aurora is at its weakest in the first two pairs of images (figures 3.9 and 3.10). This is as expected, since the footprints of both the Io Plasma Torus and the LCFL are at their northern most latitudinal ranges.

In the two uncorrected images the emission shows up as thin a bright band beginning at the Io torus footprint and extending to above the limb of the planet. On the east limb, in the region between the Io torus footprint and the LCFL, there is a spot quite separate from the main aurora. At this viewing geometry the spot seems to be above the limb of the planet. The fact that the spot coincides with the Io torus footprint and does not extend into the open field lines region suggests that it may have some connection with the plasma torus. However, Io was on the opposite side of the planet to the location of the emission spot at the time.

In the next image in the sequence, figure 3.11, the auroral structure is essentially the same as the one seen the previous night. There appears to be no change over the 24 hours between the two observing runs. In this image, figure 3.11, the spot has increased a little in brightness compared to the preceding image, extending into the disk and is connected to the main auroral emission by a thin arc running above the limb of the planet.

At CML 124° the arc has developed into a broad band, becoming part of the larger emission area. At CML=197° the aurora shows up as two bright patches of emission, one

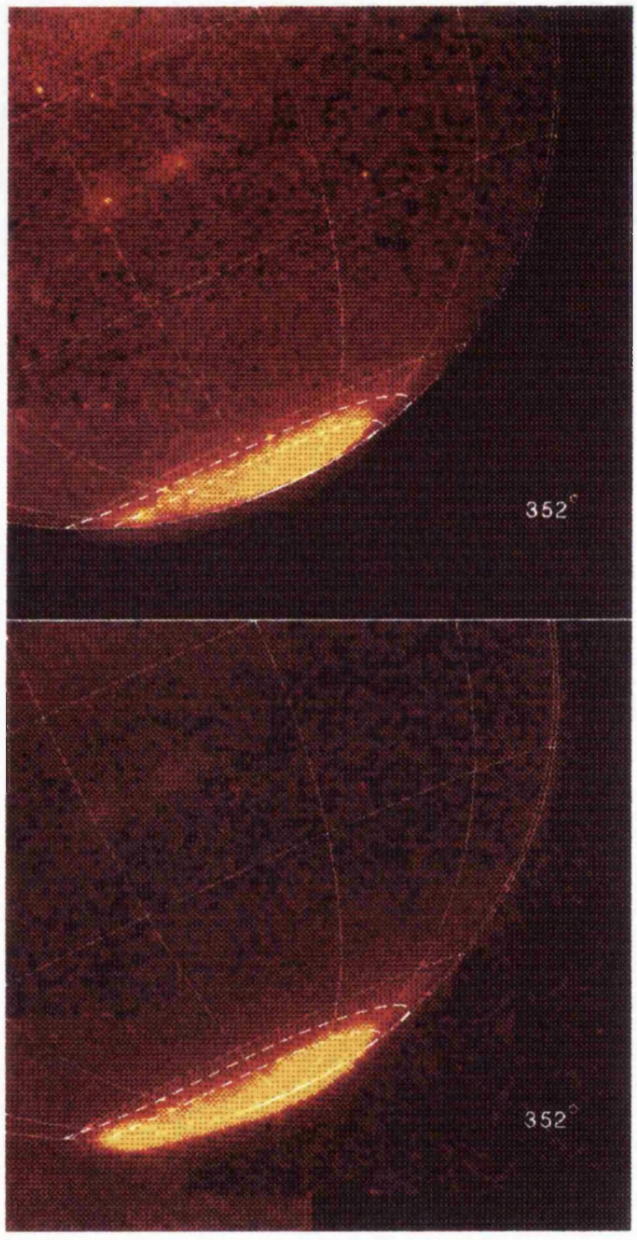

Figure 3.5: Images of the H_3^+ north aurora taken at 3.533μm. Footprints of the IPT and the LCFL, according to the O_6 model, are shown on the images as dashed lines. The CML is given in the top left hand corner of each image. The limb-brightened corrected image is shown at the top.

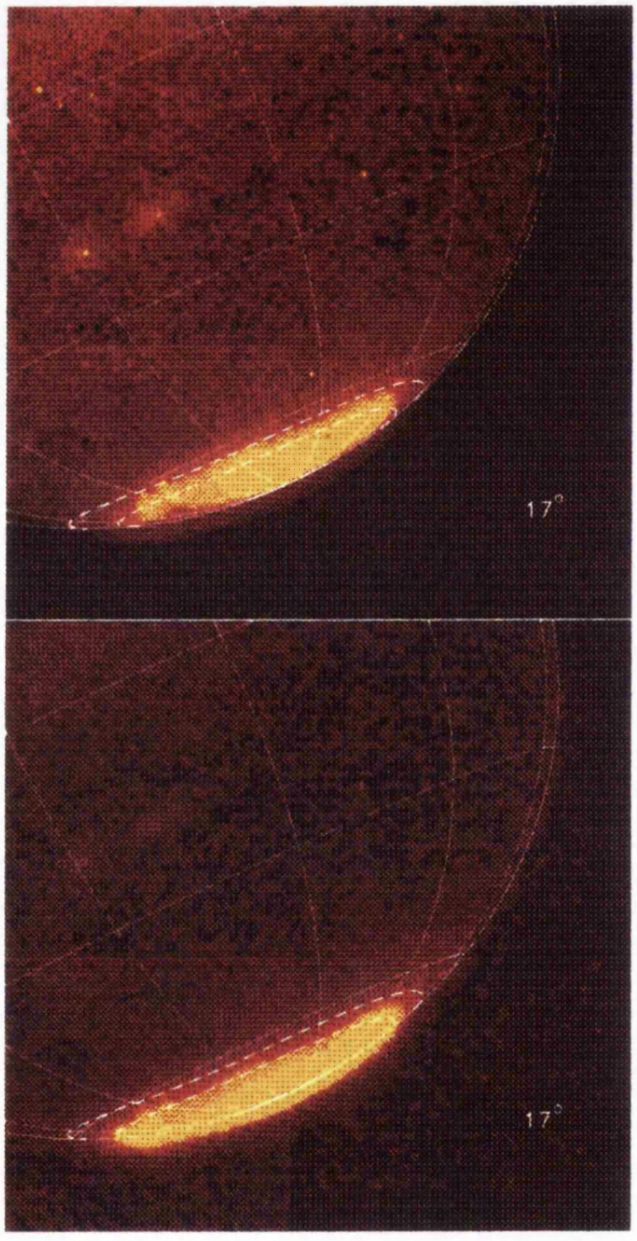

Figure 3.6: Images of the H_3^+ north aurora taken at 3.533μm. Footprints of the IPT and the LCFL, according to the O_6 model, are shown on the images as dashed lines. The CML is given in the top left hand corner of each image. The limb-brightened corrected image is shown at the top.

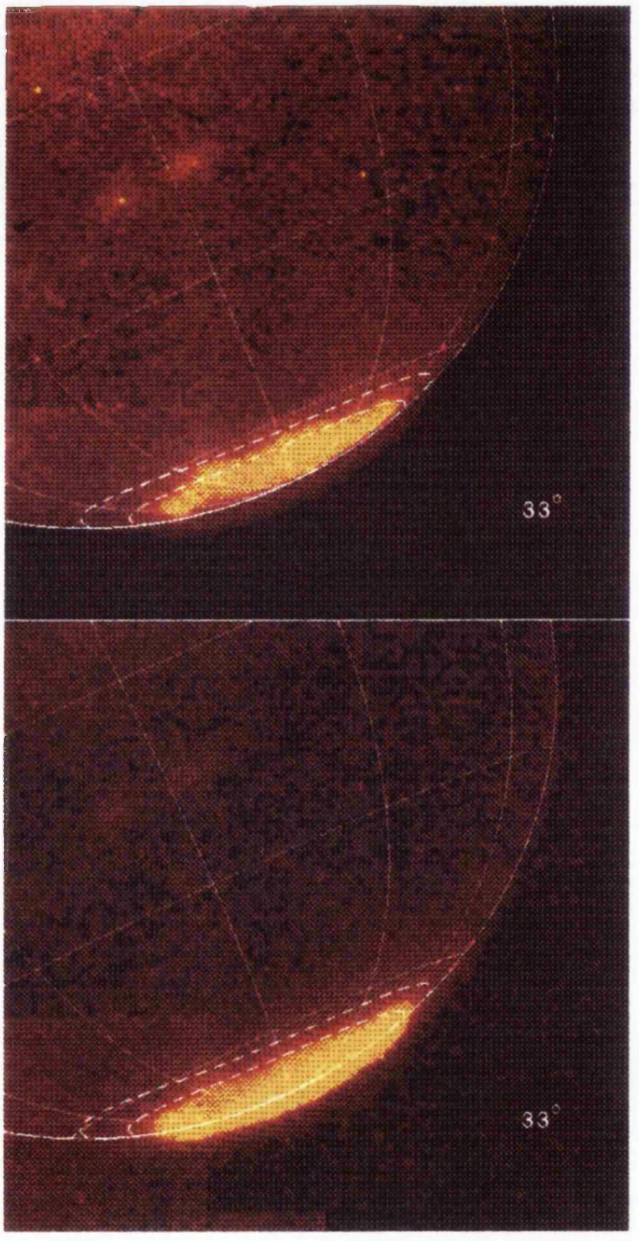

Figure 3.7: Images of the H_3^+ north aurora taken at 3.533μm. Footprints of the IPT and the LCFL, according to the O_6 model, are shown on the images as dashed lines. The CML is given in the top left hand corner of each image. The limb-brightened corrected image is shown at the top.

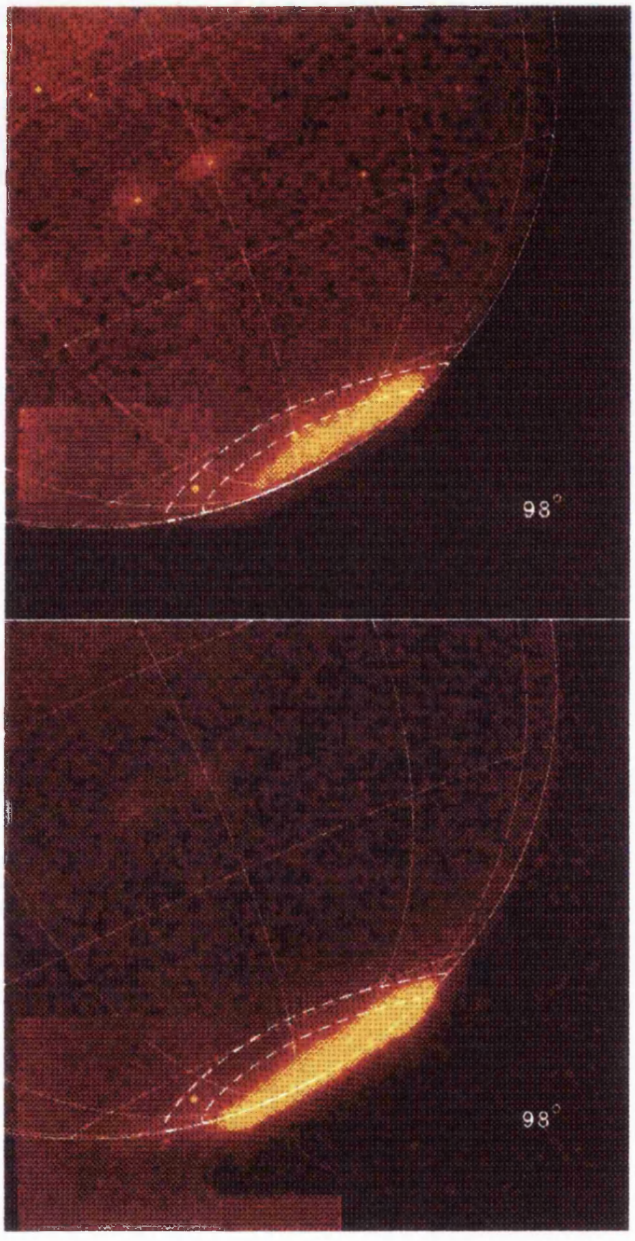

Figure 3.8: Images of the H_3^+ north aurora taken at 3.533μm. Footprints of the IPT and the LCFL, according to the O_6 model, are shown on the images as dashed lines. The CML is given in the top left hand corner of each image. The limb-brightened corrected image is shown at the top.

at $\sim 240°$ on the eastern limb, the other at about 160°, on the western limb. The two connected together by a more diffuse band of emission giving the overall structure a crab like shape. The same structure is still clearly in evidence one image later at the CML of 209° and much less so in other later images. The development of the arc as a function of longitude can not be followed as it rotates into view since no image of the northern aurora was obtained between CMLs 124° and 197°. However the structure seen in figure 3.13 and later would suggest that the spot and the arc seen in earlier images are just part of a much larger structure extending over the whole of the northern polar region. What are seen as a spot and an arc joining it to the main emission in images at CMLs 83° to 124° may be the emission from the bright patch at longitude 240° and the diffuse band emerging from the other side of the limb. If this is the case then for the very early images, i.e. at CMLs 83° and 97°, the emission must have occurred to very high altitude in order to be seen at these longitudes.

Another interesting aspect to the auroral structure that can be seen in the images is the existence of an area of very low (comparatively) auroral emission between longitudes 170° and 220°, although this is not very clear in the last image (CML=245°). The significance of this feature will be discussed later.

Correcting for the limb-brightening, drastically changes the auroral structure seen in the uncorrected images. The results shows that the northern aurora consists of a large bright region west of longitude 160° and a relatively bright spot around longitude 240°. Between 160° and 240° the aurora is relatively dim. There are spots of emission that appear elongated longitudinally. In figure 3.13, the spots seem to connect up, to form an "oval" which appears to follow the footprint of the LCFL. The "oval" is attached to the large region of bright emission to the west but does not seem to connect with the bright spot at longitude 240°. However the patches are faint and there are considerable gaps so that the exact shape of the oval can not be determined accurately.

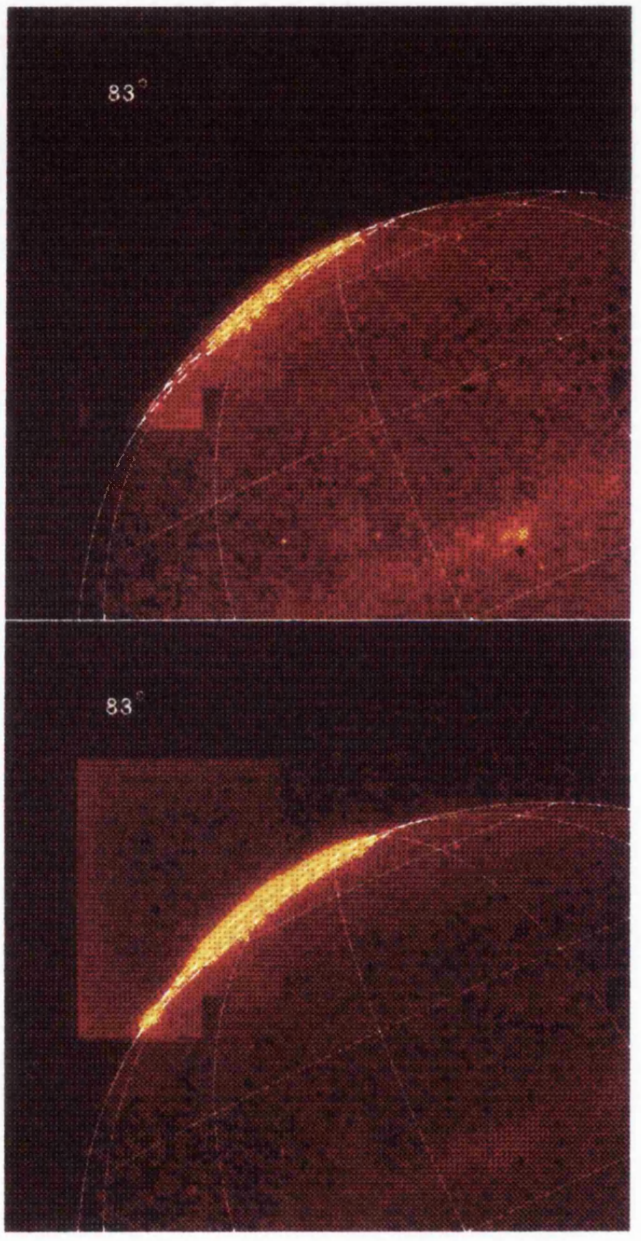

Figure 3.9: Images of the H_3^+ north aurora taken at 3.533μm. Footprints of the IPT and the LCFL, according to the O_6 model, are shown on the images as dashed lines. The CML is given in the top left hand corner of each image. The limb-brightened corrected image is shown at the top.

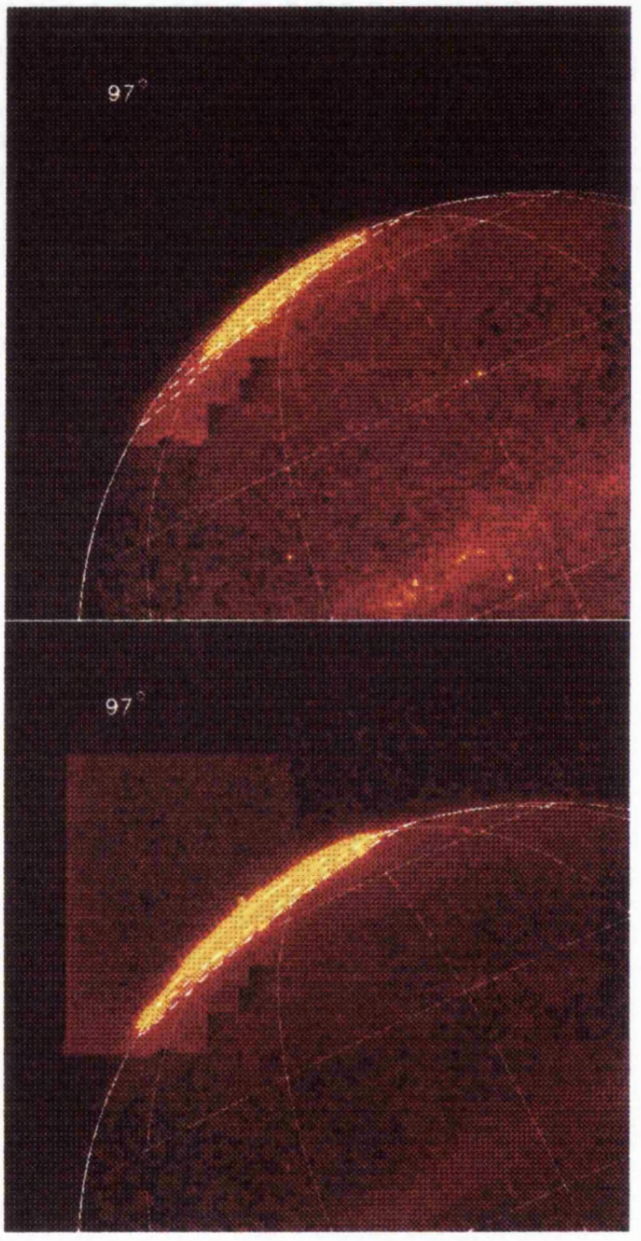

Figure 3.10: Images of the H_3^+ north aurora taken at 3.533μm. Footprints of the IPT and the LCFL, according to the O_6 model, are shown on the images as dashed lines. The CML is given in the top left hand corner of each image. The limb-brightened corrected image is shown at the top.

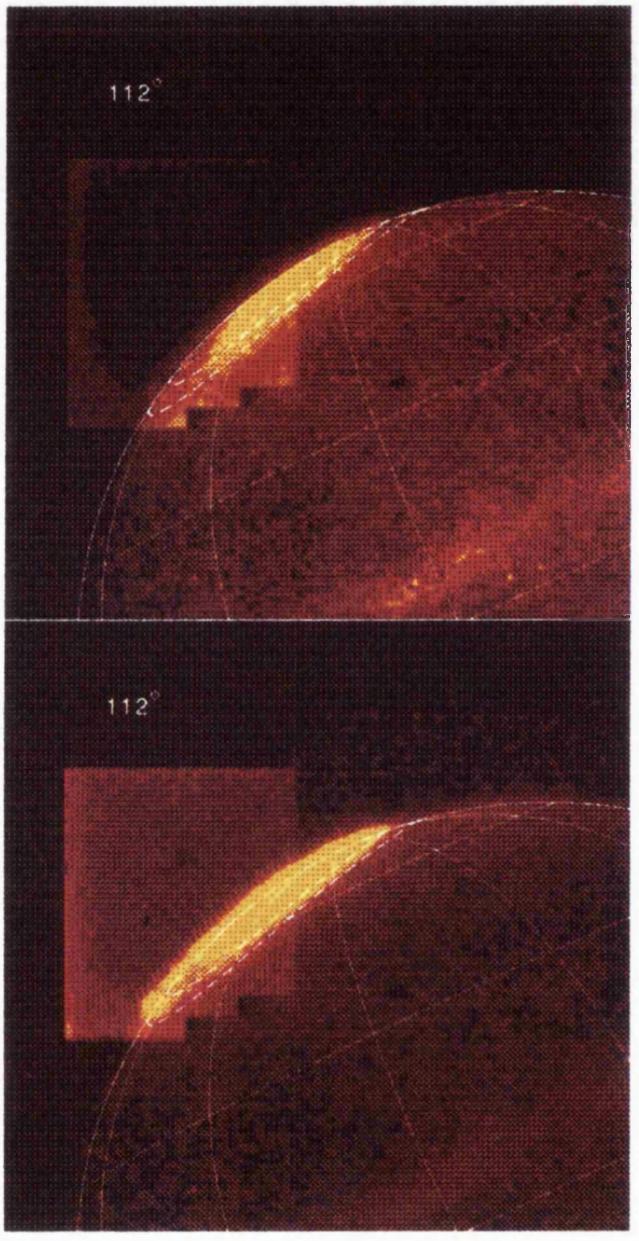

Figure 3.11: Images of the H_3^+ north aurora taken at 3.533μm. Footprints of the IPT and the LCFL, according to the O_6 model, are shown on the images as dashed lines. The CML is given in the top left hand corner of each image. The limb-brightened corrected image is shown at the top.

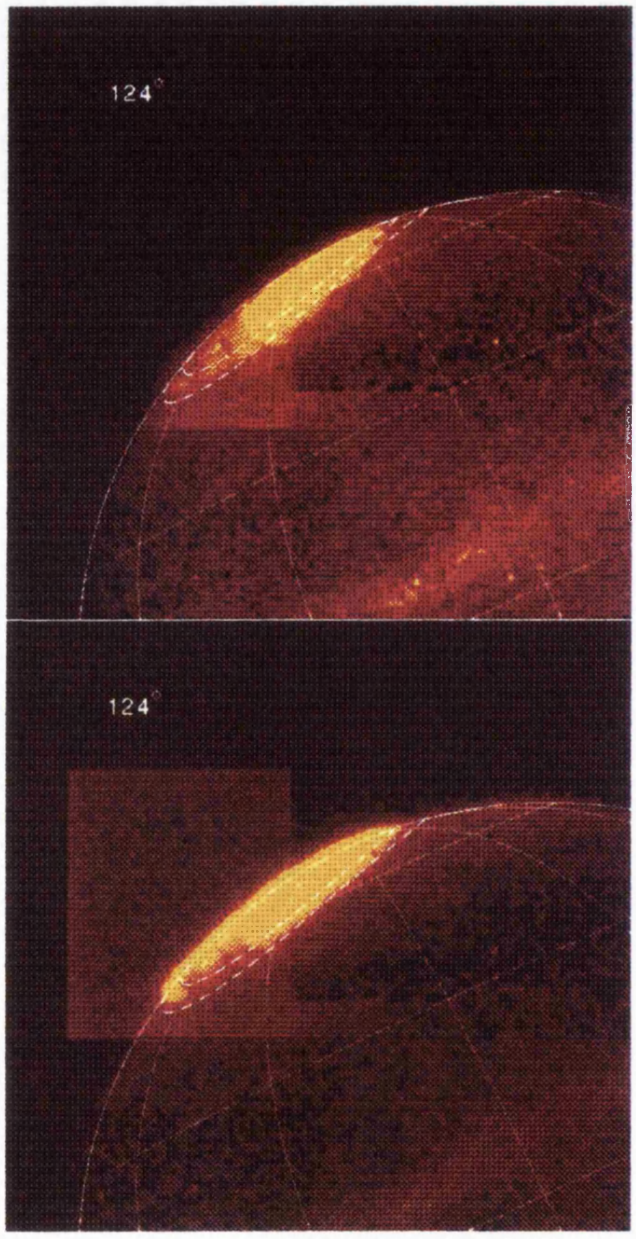

Figure 3.12: Images of the H_3^+ north aurora taken at 3.533μm. Footprints of the IPT and the LCFL, according to the O_6 model, are shown on the images as dashed lines. The CML is given in the top left hand corner of each image. The limb-brightened corrected image is shown at the top.

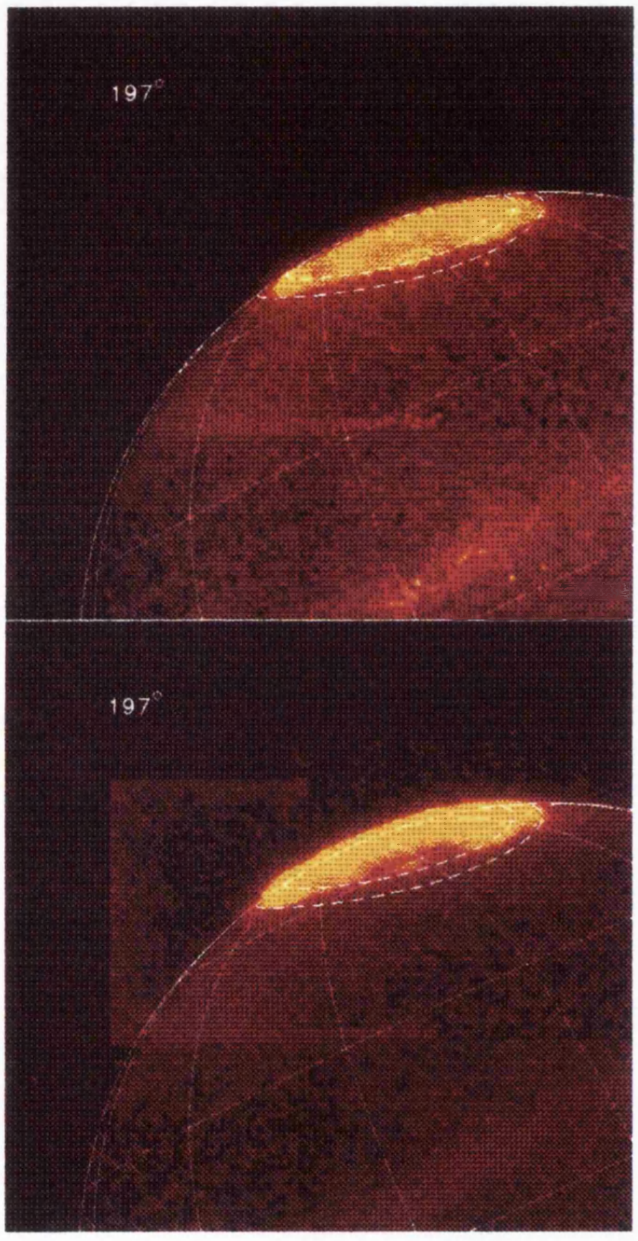

Figure 3.13: Images of the H_3^+ north aurora taken at 3.533μm. Footprints of the IPT and the LCFL, according to the O_6 model, are shown on the images as dashed lines. The CML is given in the top left hand corner of each image. The limb-brightened corrected image is shown at the top.

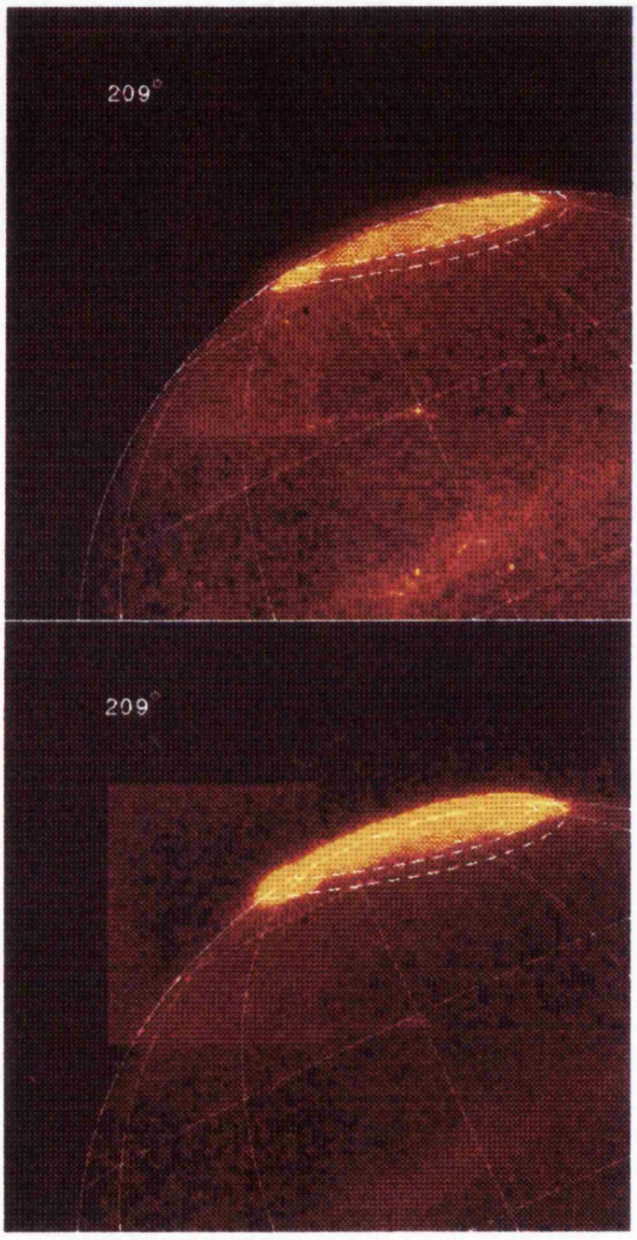

Figure 3.14: Images of the H_3^+ north aurora taken at 3.533μm. Footprints of the IPT and the LCFL, according to the O_6 model, are shown on the images as dashed lines. The CML is given in the top left hand corner of each image. The limb-brightened corrected image is shown at the top.

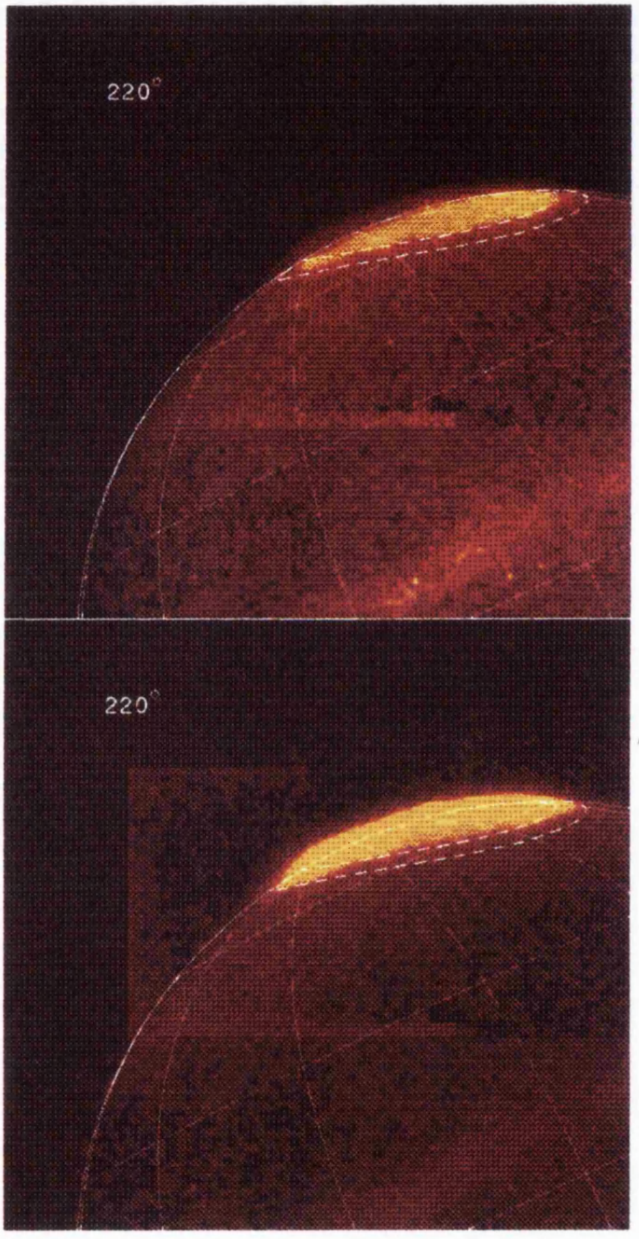

Figure 3.15: Images of the H_3^+ north aurora taken at 3.533μm. Footprints of the IPT and the LCFL, according to the O_6 model, are shown on the images as dashed lines. The CML is given in the top left hand corner of each image. The limb-brightened corrected image is shown at the top.

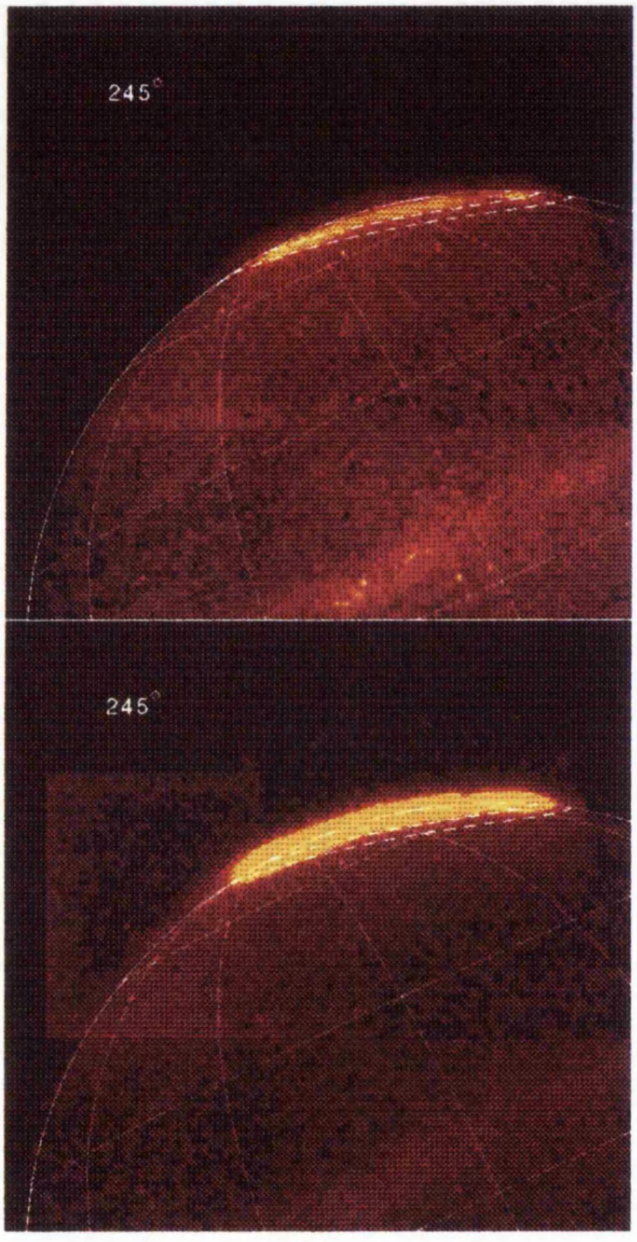

Figure 3.16: Images of the H_3^+ north aurora taken at 3.533μm. Footprints of the IPT and the LCFL, according to the O_6 model, are shown on the images as dashed lines. The CML is given in the top left hand corner of each image. The limb-brightened corrected image is shown at the top.

3.2.2 Southern Aurora

In the south the uncorrected images show that the auroral emission is more diffuse overall and the structure is not as distinct compared with that in the north. From images taken at CMLs 93° to 134°(figures 3.17 to 3.20), auroral emission is largely confined to within the LCFL, except on the western limb where it extends down to the Io torus footprint. As different longitudes rotate into view the aurora is seen to grow eastward, leading with a bright spot, to cover the whole of the limb up to the eastern limit of the LCFL. There is some similarity between this spot and the one observed in the north at these longitudes in that most of it seems to be outside the disk of the planet. This suggests that the spot is a manifestation of high altitude auroral emission on the other side of the planet, shining through the atmosphere.

From images taken at CML=202° onwards (figures 3.21 to 3.24), the aurora appears as a thin bright band covering all area pole-wards of the LCFL and extending northward to the Io torus footprint on the east and west limb. At these longitudes the Io torus footprint and the footprint of the LCFL are at their southern most latitudes and it seems that the auroral geometry is a reflection of this. On the east limb the emission appears as a bright spot located between the Io torus footprint and the LCFL. The intensity of the spot remains constant until the last image when it diminished considerably and appears to have become detached from the main auroral emission. This is a curious feature since both the spots, observed in the north at CMLs 83° to 124° and the earlier one in the south seen in images at CMLs 93° to 134°, increased in brightness as the planet rotated round and appeared to have some connection with the as yet unseen part of the aurora. This could be due to some kind of enhancement of the aurora in this region and considerably limb-brightened. The feature becomes diminished as it moves further into the body of the planet, as the effect of limb-brightening lessens.

The limb-brightening corrected images revealed a structure that was not apparent in the uncorrected images. This is most evident in the first two images (figures 3.17 and 3.18) and faintly in the next two (figures 3.19 and 3.20). It appeared to be the same oval seen in images taken during the previous night's observation, seemingly centering on the

magnetic pole and connects with the bright area of emission on the west limb (longitudes 3000° to 60°). The oval seem to be much dimmer in intensity compared to the area of bright emission. From CMLs 202° (figure 3.21) onwards the aurora is at its most narrow viewing geometry and therefore it is hard to determine if the oval is continuous at these longitudes. However the corrected images show a thin line of emission just south of the LCFL and a sharp decrease in intensity right at the limb. It is possible that the thin emission line in these later images could be part of the oval continuing round to these longitudes. The oval does not appear to follow the footprints of either of the magnetic shells (30 R_J and the Io Torus). This oval could possibly be the southern counterpart to the discrete emission seen in the north. The structure, however, is not so clear as in the northern aurora.

3.3 Discussion

The images presented in the last section show that the auroral structures remained essentially the same as when they were first observed by Baron *et al* (1991) and Kim *et al* (1991). The same morphology can be seen in images obtained by Drossart *et al* (1992), Baron *et al* (1993), Connerney *et al* (1993) and Kim *et al* (1994). In the north the large bright area around longitude 150° and the bright spot at longitude ~240° prove to be features that are constant in all images taken at the CML of about 180°. In the south the bright area of emission seen between longitudes 30° and 60° were also present in images taken by Baron *et al* (1991).

The areas of emission minima seen between 160° and 210° in the north, and between 60° and 150° in the south almost coincide with regions of strong surface magnetic field according to the O_6 of Connerney (1993)

Limb brightening correction brings out a whole host of information in the images. The interesting features are listed below.

1. Aurorae emission is not uniform over the polar regions.

2. In the northern aurora:

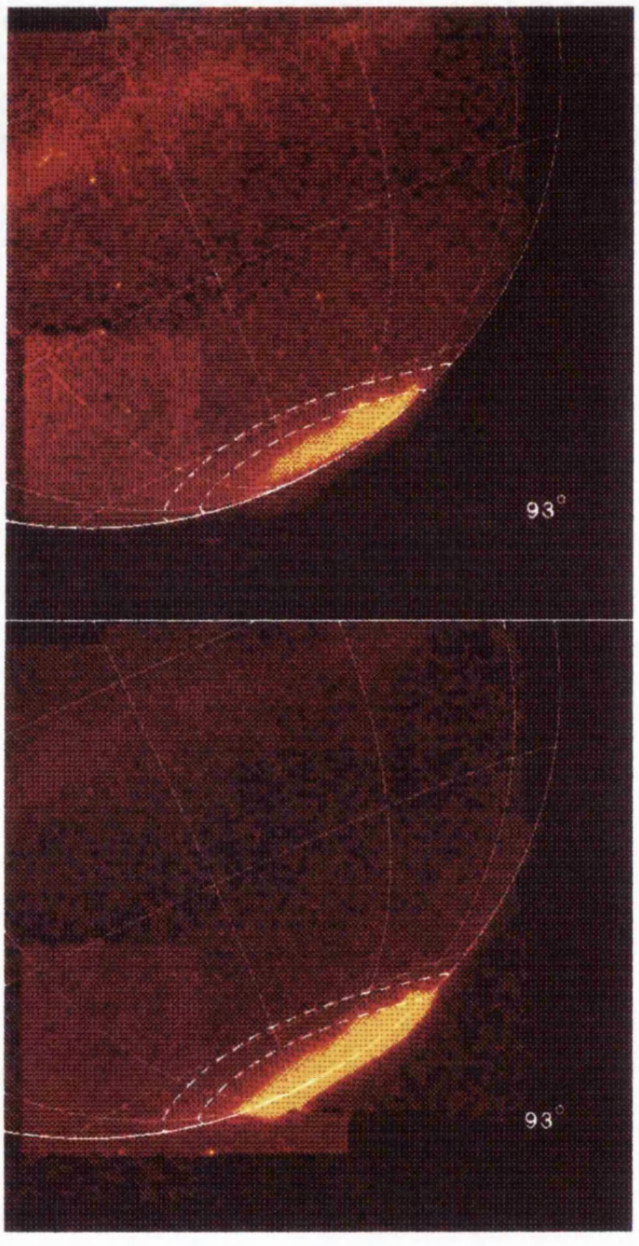

Figure 3.17: Images of the H_3^+ north aurora taken at 3.533μm. Footprints of the IPT and the LCFL, according to the O_6 model, are shown on the images as dashed lines. The CML is given in the top left hand corner of each image. The limb-brightened corrected image is shown at the top.

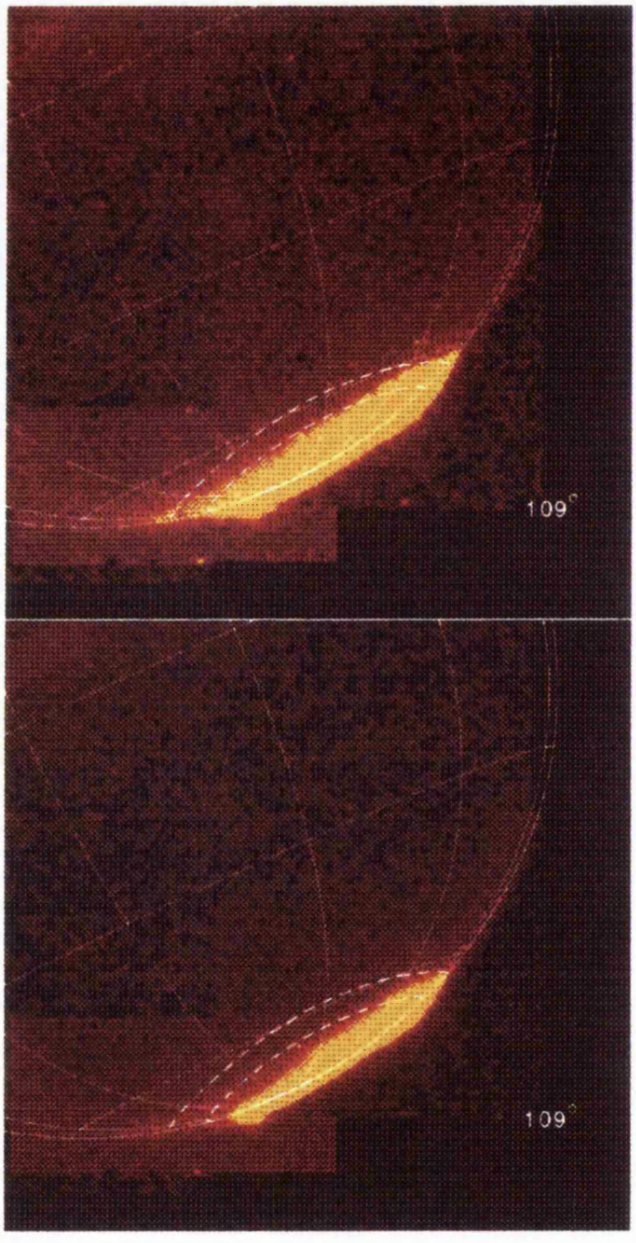

Figure 3.18: Images of the H_3^+ north aurora taken at 3.533μm. Footprints of the IPT and the LCFL, according to the O_6 model, are shown on the images as dashed lines. The CML is given in the top left hand corner of each image. The limb-brightened corrected image is shown at the top.

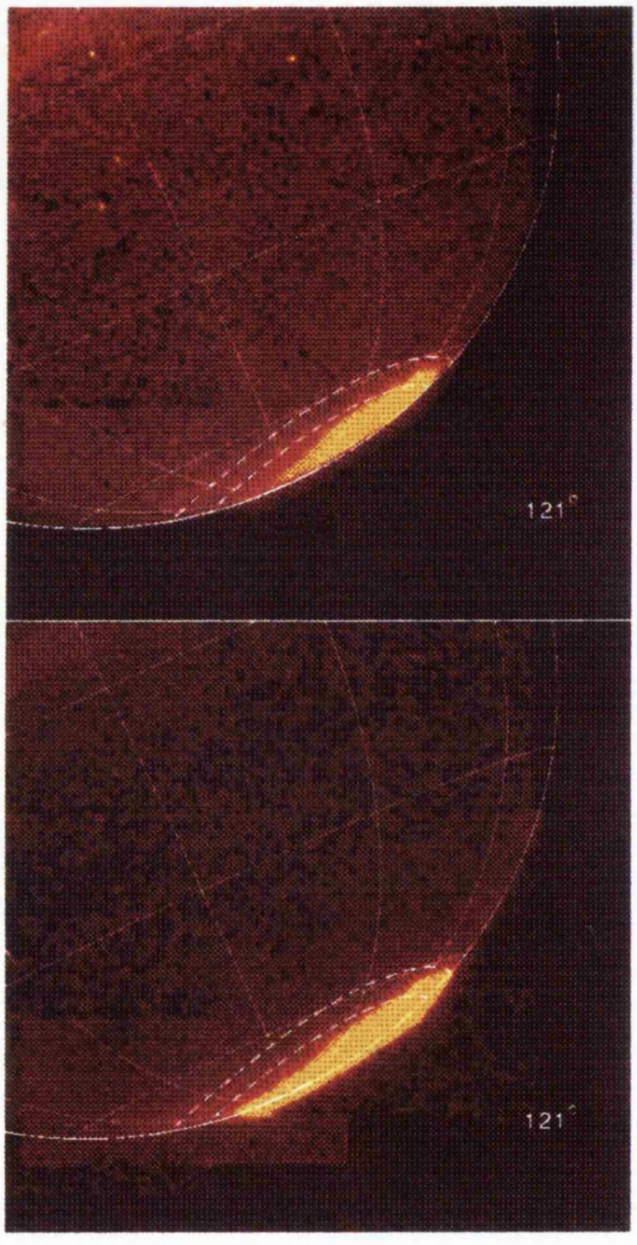

Figure 3.19: Images of the H_3^+ north aurora taken at 3.533μm. Footprints of the IPT and the LCFL, according to the O_6 model, are shown on the images as dashed lines. The CML is given in the top left hand corner of each image. The limb-brightened corrected image is shown at the top.

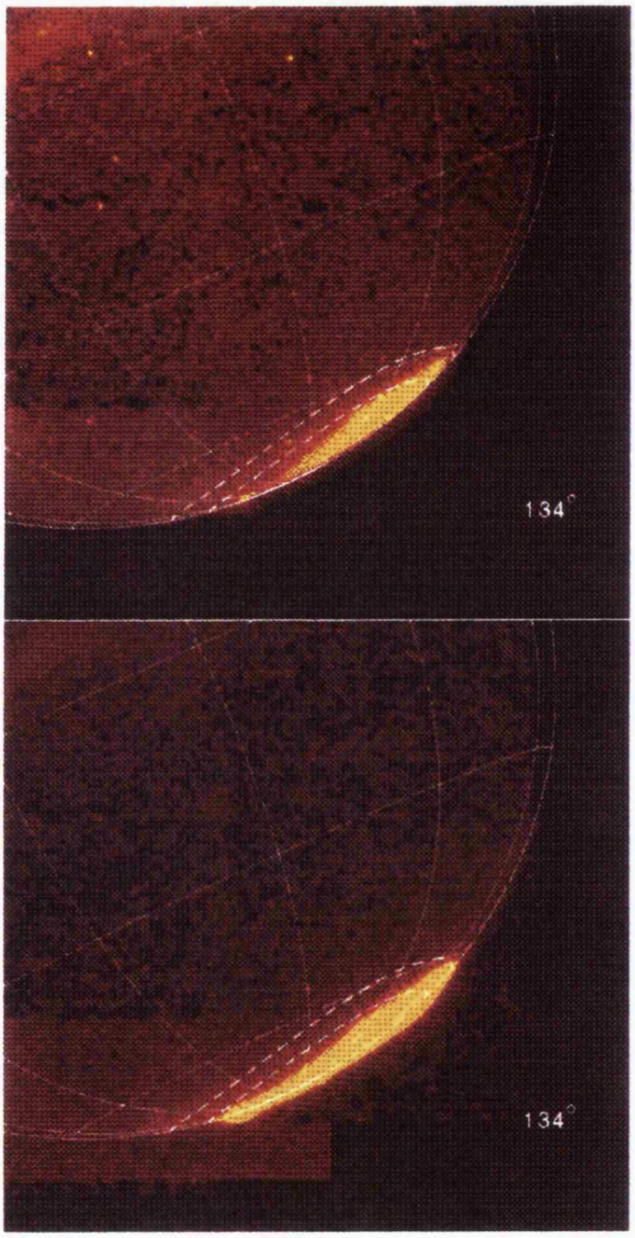

Figure 3.20: Images of the H_3^+ north aurora taken at 3.533μm. Footprints of the IPT and the LCFL, according to the O_6 model, are shown on the images as dashed lines. The CML is given in the top left hand corner of each image. The limb-brightened corrected image is shown at the top.

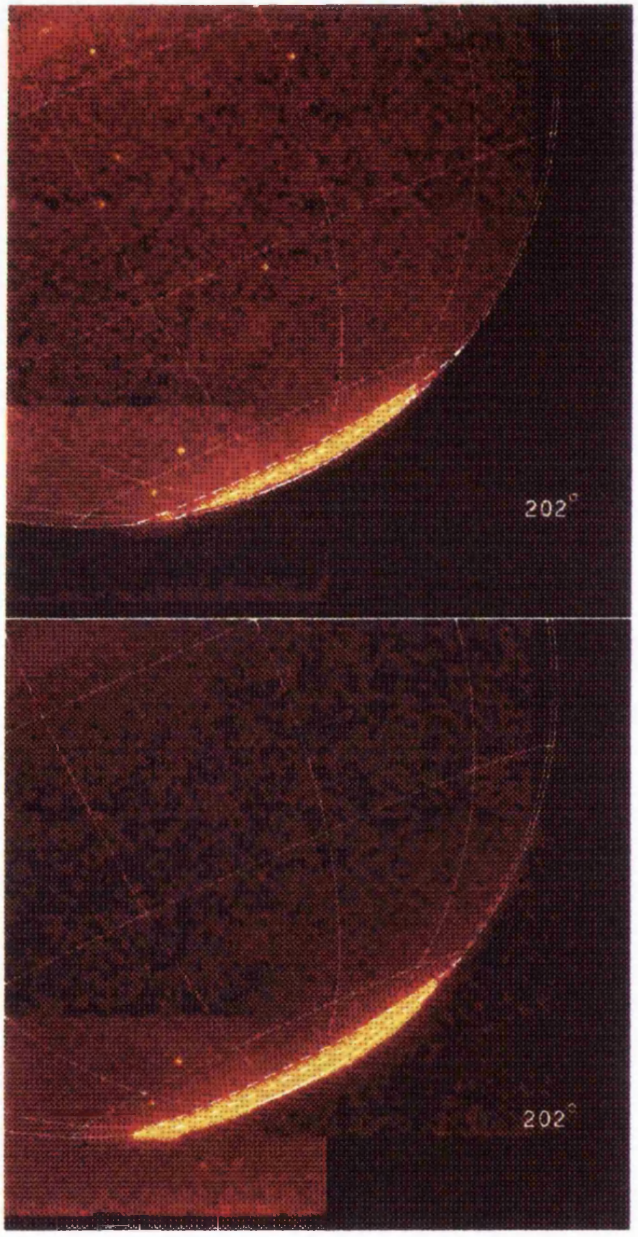

Figure 3.21: Images of the H_3^+ north aurora taken at 3.533μm. Footprints of the IPT and the LCFL, according to the O_6 model, are shown on the images as dashed lines. The CML is given in the top left hand corner of each image. The limb-brightened corrected image is shown at the top.

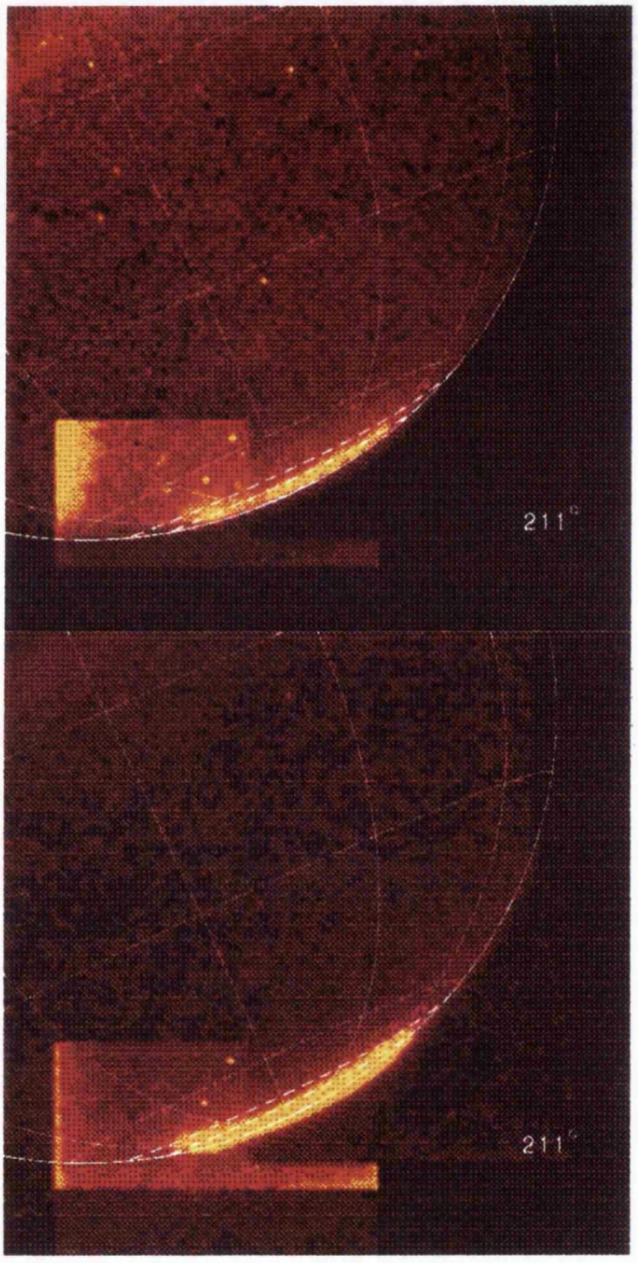

Figure 3.22: Images of the H_3^+ north aurora taken at 3.533μm. Footprints of the IPT and the LCFL, according to the O_6 model, are shown on the images as dashed lines. The CML is given in the top left hand corner of each image. The limb-brightened corrected image is shown at the top.

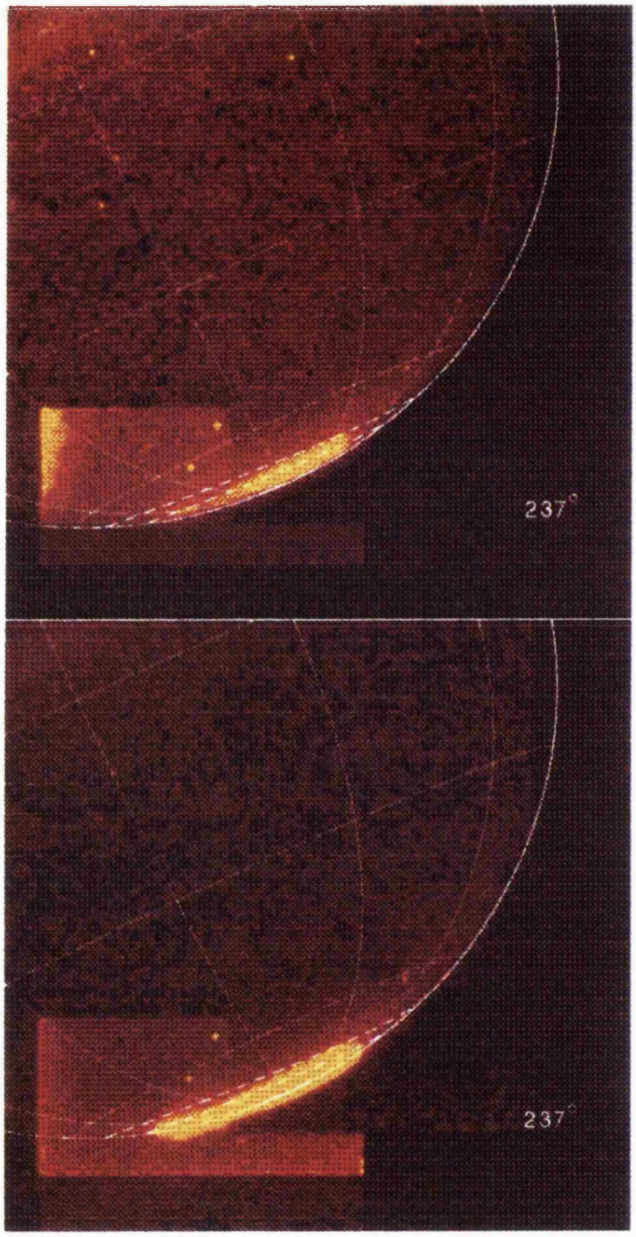

Figure 3.23: Images of the H_3^+ north aurora taken at 3.533μm. Footprints of the IPT and the LCFL, according to the O_6 model, are shown on the images as dashed lines. The CML is given in the top left hand corner of each image. The limb-brightened corrected image is shown at the top.

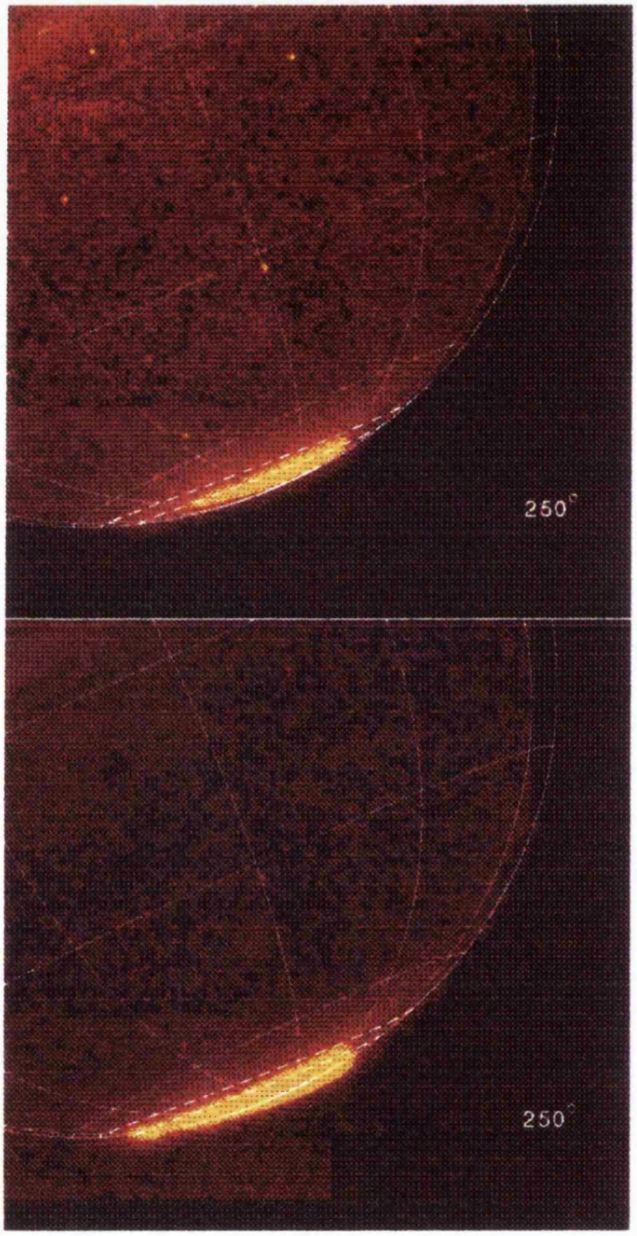

Figure 3.24: Images of the H_3^+ north aurora taken at 3.533μm. Footprints of the IPT and the LCFL, according to the O_6 model, are shown on the images as dashed lines. The CML is given in the top left hand corner of each image. The limb-brightened corrected image is shown at the top.

(a) A large bright area is observed from longitude 150° eastward.

(b) A series of spots seem to link up to form an oval centering on the pole and connecting with the large bright area.

(c) A large bright spot is observed diametrically opposite to the large bright patch and is separate from the auroral oval. The spot is located around longitude 240° and lies between the L=30 shell and the Io torus footprint.

3. For the southern aurora:

(a) A single bright patch is observed around longitude 60° and eastward.

(b) Faint oval-like emission is seen surrounding the pole. This appears to be continuous and connecting up with the bright auroral patch. The oval does not seem to follow either of the Io Torus footprint or the footprint of the 30 R_J magnetic shell and is at higher latitudes than both of them. However, poor viewing geometry of the southern aurora means that it is hard to confirm the fact.

(c) Pole-wards of the arc the emission seems to be considerably diminished.

(d) No spot equivalent to the one in the north is seen between the footprint of the 30 R_J magnetic shell and the Io Torus footprint.

The conclusions drawn from the above points are that, in the north, H_3^+ emission corresponding to L values $\geq$30 is essentially confined between longitudes 240° and eastward to 160°. According to Connerney's O_6 magnetic field model, highest surface field strength occurs between longitudes 100° and 200°. It is puzzling, therefore, to find an H_3^+ emission maximum at 150°.

The possible auroral oval in the north, seen in the limb brightening corrected images, is not a continuous line but more like a series of bright spots tenuously connected and linking up with the large bright patch around longitudes 150°. The presence of discrete bright spots indicates that particle precipitation and electrical heating due to field-aligned currents is the mechanism by which energy is supplied to the aurora here. The large

unstructured bright patch near to the pole at $\lambda_{III} = 150°$ suggests that particle precipitation due to angular diffusion is the principal energy source in this region. The existence of auroral ovals was hinted at by Baron *et al* in 1992 when they presented their images at that year's DPS meeting. Kim *et al* (1994) claimed to see such an oval in their limb brightening corrected images for the northern aurora. The location of Kim *et al*'s northern oval is not much different from the one observed here. Longitudinal variations in their oval is seen here as a series of connecting spots.

The bright spot at longitude ~240° has been present in all images of the northern aurora (Baron *et al* 1991, Kim *et al* 1991, Drossart *et al* 1992, Baron *et al* 1993, Connerney *et al* 1993, Kim *et al* 1994). Scant attention was paid to it apart from noting that it exists. Kim *et al* (1994) noticed the existence of the spot, but attributed it to limb brightening since it did not show up in their images after applying limb brightening–correction. However the spot is as bright as the area of emission at longitude 150° and a good deal brighter than the arc of diffuse emission connecting the two.

The latest U.V. images of the aurorae (Gérard 1994) showed that the northern aurora forms and oval centering on the magnetic pole. Prangé (private communication) suggested that at certain geometry the emission path length can be very long, showing up as bright spots on the limb of the planet (see fig 3.25). Normal limb brightening correction is inappropriate for such an emission geometry. A model of the oval will have to be constructed to obtain the required correction factors, which will be the subject of future work on this kind of imaging.

Like the north, the southern aurora in largely confined to magnetic shells $\geq$30. Regions of maximum surface field strength show up as areas of local minimum in the H_3^+ emission. Conversely the area where H_3^+ emission is brightest (longitude 40°) seems to coincide with the region of local minimum in surface field strength. There are no other bright patches of emission which may perhaps reflect the more uniform surface field strength found in the south. The auroral emission is more diffuse and the structure is not as well defined as that found in the north. This could also be another indication of the weaker surface field strength in the south compare to that in the north. The auroral oval seen in the

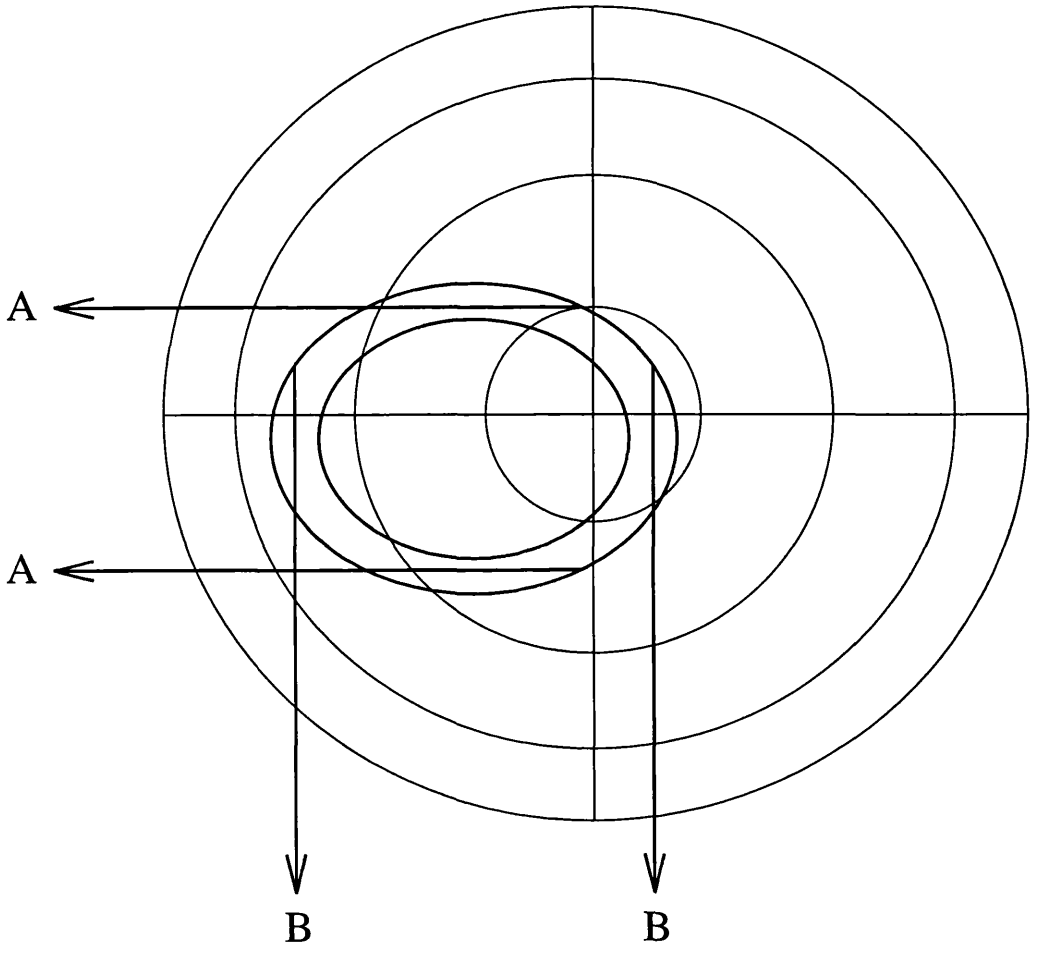

Figure 3.25: Diagram showing how the path length of an emission oval varies depending on the viewing angle of a distant observer. The column length will be longer when viewed at **A** than when viewed at **B** and therefore the emission will appear correspondingly brighter.

corrected images gives an indication that currents (field-aligned or otherwise) is having an effect in the southern aurora. However, its faintness suggests that this mechanism is not as strong as that at work in the north. A departure of the emission structure from the geometry of the magnetic field is shown by the fact that the auroral oval does not follow either of the footprints plotted on the image. The oval could be mapping out a footprint of a magnetic shell at much larger distance than the 30 R_J plotted. There is some tentative evidence for field lines remaining closed at such large distances from the planet (Prangé private communication), however, it is not clear whether this is permanent or just a transient response to some unknown event. Also, it should be noted that the O_6 model of Connerney (1991, 1993) is not perfect at surface level and this could also be the reason why the aurora seems to be at higher latitude than the 30 R_J oval.

Chapter 4

Spectroscopic Study of Jupiter

Results from fitting to the data obtained using the CGS4 spectrometer are reported in this chapter. Fitted temperatures and column densities are shown first for the pole to pole spectra. A discussion about the correlated nature of the fitted parameters then follows in which they are shown to be highly anti-correlated. A total emission parameter is introduced in an attempt to circumvent the correlation between the model temperature and column density. Finally the results for spectra taken with the slit aligned along the equator is examined for signs of the east—west asymmetry perceived in the spectral images.

In fitting the spectra, extensive use was made of the H_3^+ transitions listed in tables 4.1 to 4.4 for the 3.5 μm and 4.0 μm ranges respectively. The values were originally taken from Kao *et al* (1991) but have been updated to incorporate the latest theoretical predictions (B. M. Dinelli, private communication).

4.1 Pole to Pole Spectra

In the 3.45 μm wavelength range, it has been demonstrated that H_3^+ emission can be seen at all latitudes (see chapter 2). This is reflected in tables 4.5 to 4.14 where temperatures and column densities were obtained by fitting to spectra from all the rows on the planet.

As has been discussed previously, H_3^+ emission is only observable near the polar region

Ortho H_3^+ transitions only							
J'	$E'(cm^{-1})$	$\omega_{if}(cm^{-1})$	$A_{if}(cm^{-1})$	J'	$E'(cm^{-1})$	$\omega_{if}(cm^{-1})$	$A_{if}(cm^{-1})$
9	6174.287	2714.245	0.400E-2	4	5895.604	2870.890	0.165E+3
5	5969.366	2737.851	0.315E+2	5	3552.620	2894.610	0.629E+2
7	6310.101	2741.151	0.665E+2	4	3233.027	2918.026	0.430E+2
6	6299.228	2746.608	0.387E+2	4	3446.685	2930.163	0.118E+3
2	7758.420	2764.106	0.715E+2	4	5810.346	2934.155	0.638E+2
4	6254.046	2769.393	0.300E+2	5	6390.680	2944.828	0.228E+3
7	6782.988	2773.664	0.380E+1	6	4029.071	2949.555	0.429E+2
3	5430.347	2816.843	0.286E+2	6	6514.192	2961.572	0.813E+2
9	6650.164	2821.518	0.937E+2	6	6638.729	2965.232	0.393E+2
5	5969.366	2825.956	0.119E+3	5	6212.584	2979.557	0.104E+3
4	3144.790	2829.924	0.106E+3	5	6129.579	2984.787	0.151E+3
6	6514.192	2840.694	0.440E+2	7	4561.507	2986.672	0.269E+2

Table 4.1: Einstein A_{if} coefficients for CGS4 3.45 μm fitting.

in the 4.0 μm wavelength range. Therefore, for 4.0 μm observations, tables 4.15 to 4.22 only report the results for those rows on or near to the poles of the planet, namely rows 19 to 22 for the north and rows 6 to 9 for the south, where H_3^+ emission lines can be detected.

In fitting the spectra both the temperature and the column density were free parameters but the ortho/para ratio was fixed at 1:1. Uncertainty estimates using the 2-σ deviation described in section 2.5 give errors of about $\pm$30 K for the brightest rows and up to $\pm$200 K for less intense rows on the body of the planet. Uncertainties for the column densities range typically between $\pm$15% for rows sampling the auroral regions to $\pm$60% for those on or near Jupiter's equator. Where the upper and lower values are not available for the temperature and column density, the error determination procedure could not make sensible assessments of the limits, within the 2-σ deviation, due to the quality of the spectra.

In addition to the fitted temperatures and column densities the tables also report a number of other parameters. The **Lat./km** parameter gives the estimated latitude/height above the limb for the center of each row only, assuming that the planet was accurately positioned on the images. This means that rows which appeared to be just off the planet

Para H_3^+ transitions only							
J'	$E'(cm^{-1})$	$\omega_{if}(cm^{-1})$	$A_{if}(cm^{-1})$	J'	$E'(cm^{-1})$	$\omega_{if}(cm^{-1})$	$A_{if}(cm^{-1})$
9	6030.797	2696.224	0.736E+0	3	3063.193	2826.117	0.919E+2
2	5265.703	2718.262	0.421E+2	4	3325.518	2831.340	0.107E+2
2	7751.643	2719.667	0.501E+2	4	3259.663	2832.188	0.448E+2
4	5714.864	2724.058	0.354E+2	4	5845.422	2842.936	0.159E+3
2	2812.642	2725.898	0.988E+2	6	6249.022	2854.191	0.231E+2
2	2790.127	2726.219	0.604E+2	4	5930.849	2868.404	0.146E+3
3	5485.542	2730.887	0.186E+3	5	3721.811	2889.052	0.623E+1
6	6414.529	2730.204	0.402E+1	5	3659.563	2891.867	0.265E+2
6	6392.663	2733.100	0.147E+2	5	3395.911	2894.488	0.123E+3
6	6249.022	2740.568	0.294E+2	4	5887.398	2895.874	0.983E+2
6	6139.144	2743.233	0.618E+2	5	6167.744	2908.081	0.150E+3
3	2930.998	2762.068	0.839E+2	4	3351.023	2923.361	0.871E+2
7	6448.892	2764.567	0.619E+2	4	3422.758	2928.351	0.111E+3
3	3002.486	2765.547	0.210E+2	4	5651.768	2932.988	0.245E+2
4	6362.564	2767.678	0.752E+2	6	4187.703	2937.793	0.422E+1
8	6298.772	2769.010	0.899E+2	6	4128.273	2942.209	0.174E+2
4	6452.726	2770.940	0.113E+3	5	6275.155	2949.638	0.156E+3
4	5845.422	2783.325	0.470E+2	5	6375.334	2952.576	0.162E+3
4	5845.422	2783.325	0.470E+2	6	3883.248	2955.154	0.801E+2
3	5572.834	2783.417	0.117E+3	6	3684.325	2956.073	0.137E+3
4	5714.864	2785.121	0.181E+3	4	5887.398	2956.400	0.879E+1
7	6671.363	2788.114	0.511E+2	5	6326.970	2975.947	0.102E+3
8	6673.502	2797.093	0.721E+2	7	4719.008	2978.657	0.298E+1
3	5532.956	2809.767	0.741E+2	7	4662.536	2984.069	0.122E+2
5	6167.744	2818.072	0.519E+2	7	4419.204	2989.480	0.398E+2
3	5572.834	2818.196	0.116E+2	4	5920.812	2989.815	0.699E+2
3	2992.161	2823.152	0.477E+2	6	6392.663	2996.752	0.122E+2

Table 4.2: Einstein A_{if} coefficients for CGS4 3.45 μm fitting.

Ortho H_3^+ transitions only							
J'	$E'(cm^{-1})$	$\omega_{if}(cm^{-1})$	$A_{if}(cm^{-1})$	J'	$E'(cm^{-1})$	$\omega_{if}(cm^{-1})$	$A_{if}(cm^{-1})$
3	5909.6490	2424.7970	0.348E+02	1	2616.4870	2529.7240	0.128E+03
4	6254.0460	2433.9010	0.303E+02	5	6212.5837	2539.7440	0.622E+02
6	6638.7290	2436.9560	0.280E+02	3	5566.3299	2541.4331	0.564E+02
4	5895.6041	2449.8000	0.100E+03	3	5430.3466	2554.2766	0.106E+03
6	4029.0708	2452.7183	0.810E+02	4	5432.7349	2557.4840	0.448E+02
5	6129.5804	2456.0833	0.103E+02	3	2876.5910	2561.4930	0.341E+02
2	7326.8504	2457.8772	0.112E+03	2	5180.6620	2566.9040	0.984E+02
3	5077.4894	2464.6526	0.564E+02	6	3568.9500	2573.5820	0.201E+02
5	3742.3456	2471.9230	0.113E+03	4	3233.0270	2574.6600	0.229E+02
5	3552.6199	2472.8460	0.723E+02	9	4604.8010	2575.1120	0.143E+02
2	5285.8930	2474.0535	0.785E+02	4	5810.3460	2577.6290	0.101E+03
4	3144.7904	2486.5593	0.457E+02	2	7758.4200	2577.7580	0.251E+03
6	6638.7291	2492.0398	0.107E+02	7	4177.2040	2591.3230	0.159E+02
0	7492.6596	2498.3457	0.471E+03	5	3673.4970	2593.4600	0.982E+01
3	3025.5278	2509.0750	0.123E+03				

Table 4.3: Einstein A_{if} coefficients for CGS4 4.0 μm fitting.

Para H_3^+ transitions only							
J'	$E'(cm^{-1})$	$\omega_{if}(cm^{-1})$	$A_{if}(cm^{-1})$	J'	$E'(cm^{-1})$	$\omega_{if}(cm^{-1})$	$A_{if}(cm^{-1})$
2	7514.5900	2427.5870	0.153E+02	4	3325.5178	2492.5416	0.111E+03
7	4248.8910	2431.8210	0.518E+02	0	6578.3361	2493.0768	0.644E+01
4	6362.5640	2434.6100	0.147E+02	3	2930.9981	2503.3479	0.597E+02
1	7991.6810	2437.9690	0.937E+02	3	3002.4862	2508.1312	0.107E+03
4	6105.2550	2438.5090	0.289E+02	4	5930.8492	2508.7576	0.461E+02
3	7460.6960	2438.6400	0.218E+02	3	5572.8344	2510.2918	0.728E+02
6	3684.3250	2446.6327	0.306E+02	2	5304.1123	2514.6199	0.998E+02
6	4187.7035	2447.9036	0.104E+03	1	5124.5077	2515.7553	0.125E+03
6	4128.2727	2449.5330	0.963E+02	2	2755.2911	2518.2073	0.838E+02
0	4997.4225	2449.8855	0.247E+03	4	5845.4217	2520.6779	0.832E+01
2	7751.6427	2452.9568	0.854E+02	2	8170.3690	2530.3704	0.10E+03
6	3883.2484	2453.4080	0.607E+02	4	5250.2191	2532.2537	0.65E+02
7	4456.2220	2454.3892	0.256E+02	5	6326.9697	2534.9223	0.58E+02
0	2521.2820	2457.2906	0.119E+03	4	5887.3982	2536.9310	0.79E+02
5	6346.0320	2457.5689	0.224E+02	2	5778.2632	2538.2530	0.58E+02
2	7299.5340	2458.2938	0.621E+02	1	5087.0036	2539.4510	0.13E+03
5	3395.9113	2467.5520	0.370E+02	1	7571.9410	2539.9650	0.14E+03
8	5108.9604	2470.6213	0.126E+02	3	5532.9562	2541.2936	0.10E+03
5	3721.8108	2472.3250	0.109E+03	2	5265.7032	2542.4674	0.12E+03
5	3659.5633	2473.2388	0.955E+02	1	2609.3774	2545.4180	0.66E+02
2	7514.5902	2482.6143	0.997E+02	2	5304.1123	2548.8213	0.15E+02
3	5485.1516	2483.5535	0.174E+02	4	5542.5039	2550.3432	0.14E+02
9	5818.7127	2484.1401	0.910E+01	2	2790.1274	2552.9877	0.22E+02
1	7571.9410	2484.9374	0.141E+03	2	2723.7648	2554.6640	0.45E+02
3	5209.3075	2486.8448	0.328E+02	3	2992.1610	2564.4080	0.24E+02
2	7751.6427	2485.9396	0.139E+03	4	3063.1930	2567.2850	0.27E+02
3	5280.7993	2491.9761	0.117E+02	3	3063.1930	2568.7030	0.64E+01
4	3259.6634	2491.7493	0.871E+02				

Table 4.4: Einstein A_{if} coefficients for CGS4 4.0 μm fitting.

may still have auroral emission in them. This point is illustrated clearly in figure 4.1 showing a 3.45 μm image with two white lines indicating the estimated positions of the planetary limbs. H_3^+ emission can still be detected up to two rows beyond the limb of the planet. Given that the spatial resolution in the direction parallel to the 1″ slit was 3.08″, this means at Jupiter the distance covered by each pixel would have been about 10000 km. It is generally believed that H_3^+ forms high up in the jovian atmosphere, between 200 km to 2000 km above the homopause. But even at the uppermost limit it would be unrealistic to expect H_3^+ to be detectable up to 20000 km from the "surface" of the planet. Examination of the standard star spectral image revealed spectral intensities of up to 5% were found on both sides of the row containing the observed spectrum. Thus detector array leakage alone combined with seeing effects (of the order of 1″) could explain the apparent presence of small amount of H_3^+ emission at distances up to 20000 km from the "surface" of the planet.

Peak intensities of H_3^+ emission lines at 3.533 μm for the 3.45 μm data and at 3.986 μm for the 4.0 μm data are given in column headed **Imax**. This is intended to help with the interpretation of results. The **L.S.** column gives the estimated correction factor due to the limb brightening effect. This was divided into the fitted column densities to obtain limb brightening corrected values, $\mathbf{N(H_3^+)^*}$. Columns giving the total emissions $\mathbf{E(H_3^+)}$ and total emission corrected for the line of sight effect $\mathbf{E(H_3^+)^*}$ will be discussed later on in this chapter.

Examples of fitted spectra are shown in figures 4.2 and 4.3. The spectra were extracted from the 2-D spectroscopic images shown in figures 2.8 and 2.10.

4.1.1 Northern Auroral Results

The results for the northern aurora can be found in tables 4.5 to 4.22 occupying rows 19 to 22. At around λ_{III} = 180° the auroral boundary extends as far south as latitude 50° (southern–most limit of the Io torus footprint). In this situation row 18 may pick up some of the auroral emission due to the relatively large pixel size (≈10000 km/pixel). However at these latitudes we see only the very outer edge of the aurora and, unless a

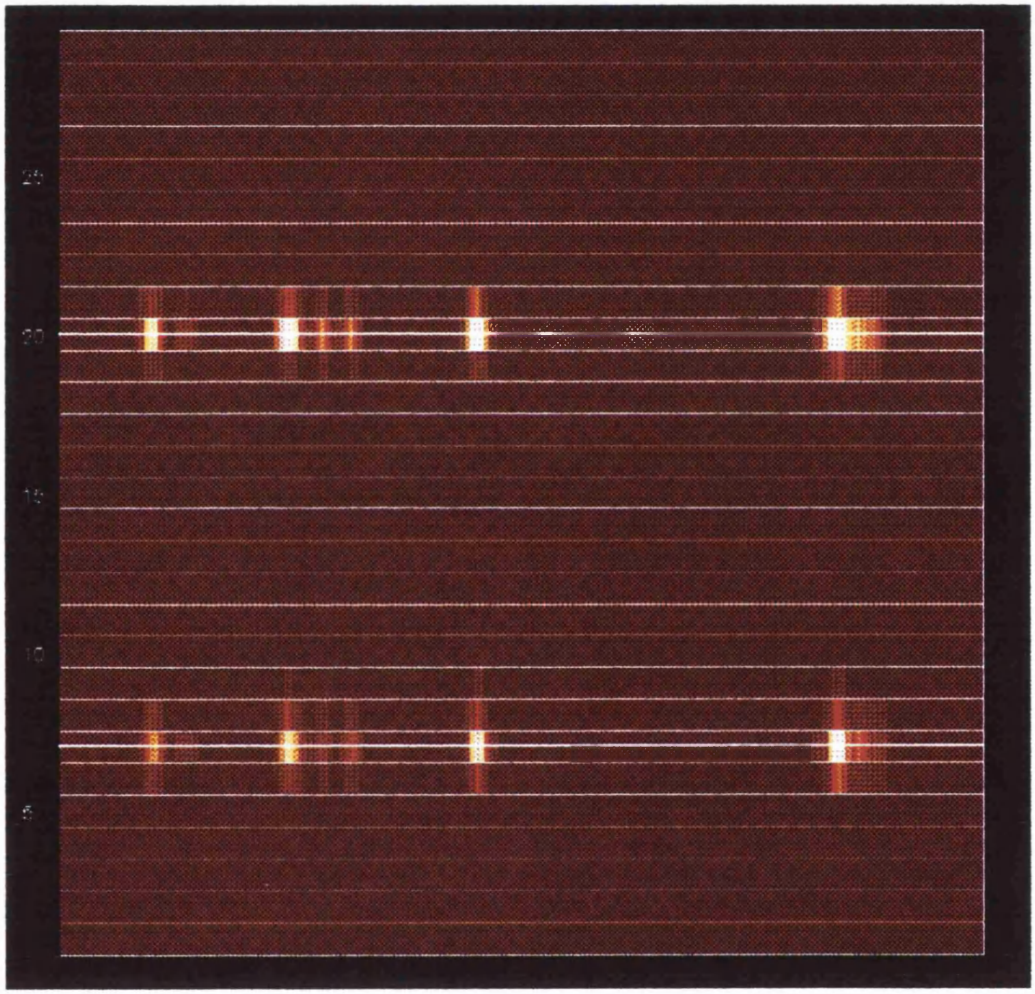

Figure 4.1: 2-D spectral image of Jupiter. Two white lines running through the middle of spectral rows show where the edges of the planet is estimated to be.

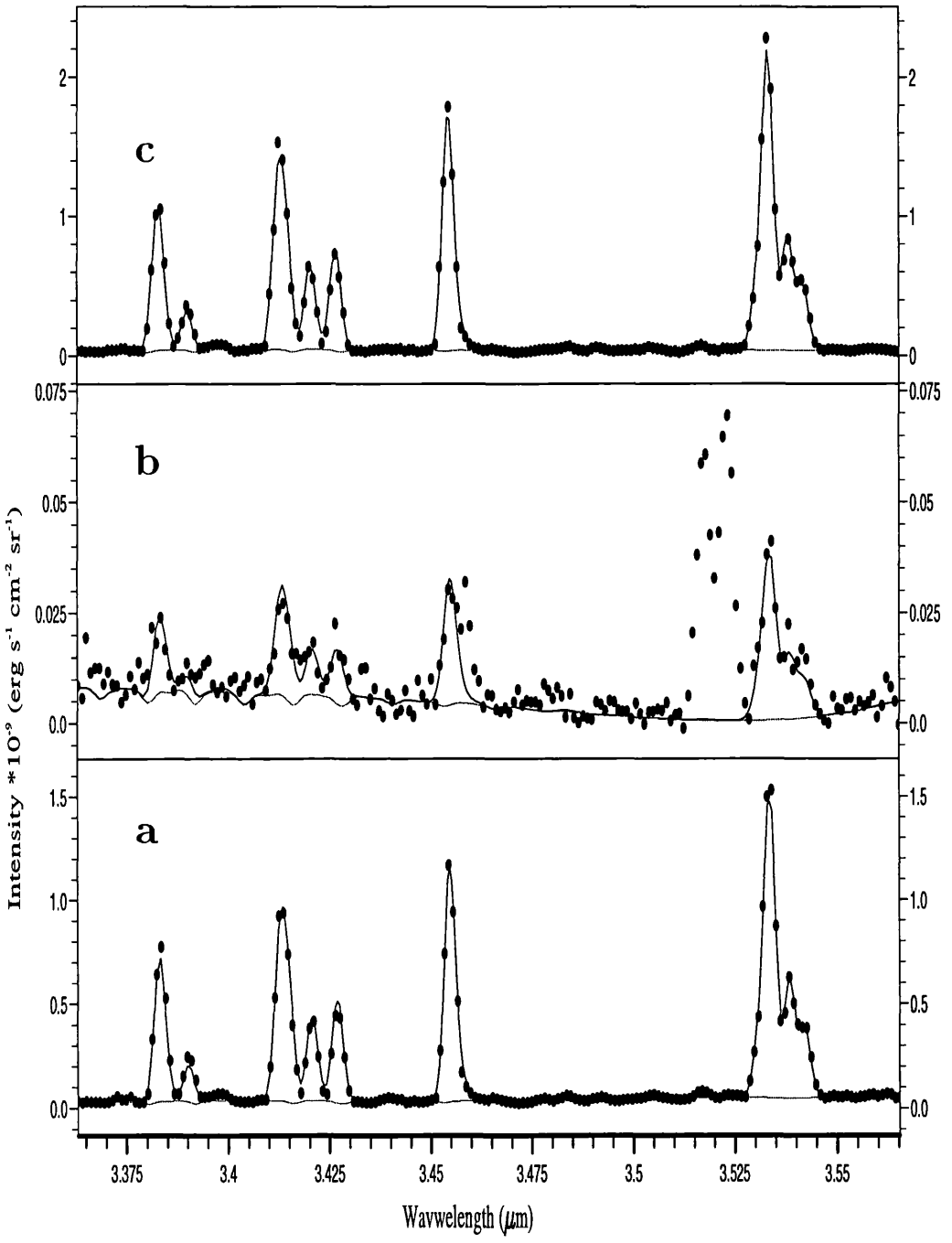

Figure 4.2: Examples of fitted 3.45 μm spectra from individual rows shown in fig 2.8. The spectra were taken from rows 20 (**c**), 14 (**b**) and 7 (**a**). The fitted temperatures and column densities are 822K and 51.4 $\times$ 10^{12} cm^{-2} for row 20, 755K and 1.44 $\times$ 10^{12} cm^{-2} for row 14, 786K and 41.6 $\times$ 10^{12} cm^{-2} for row 7. The unfitted feature in the spectrum (**b**) at 3.52 μm is the "doublet" referred to by Ballester *et al* (1994) and in chapter 2 of this work.

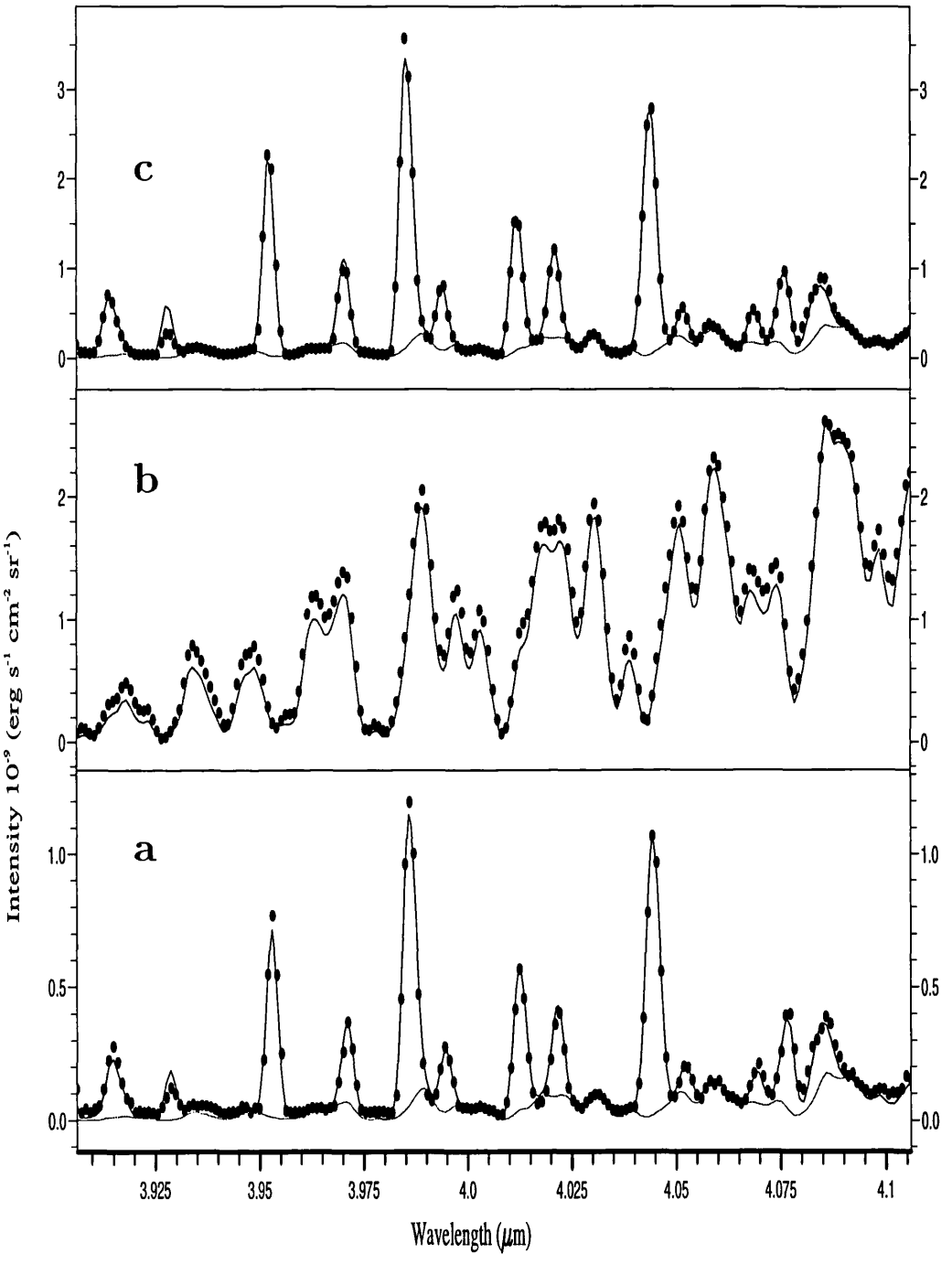

Figure 4.3: Examples of fitted 4.0 μm spectra from individual rows shown in fig 2.10. The spectra were taken from rows 20 (**c**), 14 (**b**) and 7 (**a**). The fitted temperatures and column densities were 903K and 43.7 $\times$ 10^{12} cm^{-2} for row 20, 1019K and 10.47 $\times$ 10^{12} cm^{-2} for row 7. **b** shows a typical spectrum used as an estimate of the continuum emission in the fitting.

significant fraction of the pixel is filled by the aurora, the contribution to the intensity of the spectrum is not significant.

Fitted temperatures for the 3.45 μm data range from around 700 K to over 1000 K. Between λ_{III} = 170° and 240° the temperature shows an increase by more than 200 K. This variation is outside of the estimated range of uncertainty and seems to be genuine. A temperature minimum was found around λ_{III} = 90°. However the 4.0 μm temperature profile for the north polar region shows a minimum around λ_{III} = 180° where, according to the results derived from the 3.5 μm data, a maximum is expected, and a maximum around 330° to 30° where a minimum is expected. Temperatures derived for spectra at λ_{III} = 26° and 92° have large uncertainties and therefore, values in keeping with those derived from the 3.45 μm data are possible. At λ_{III} = 299° and 339° the fitted temperatures have small uncertainty ranges and so reconciling results in this wavelength region with the 3.45 μm data is not so easy.

Fitted column densities corrected for the limb-brightening effect also exhibit spatial variability ranging from about 1.5 $\times$ 10^{12} cm^{-2} to over 18.5 $\times$ 10^{12} cm^{-2}. A broad peak in the column density is observed around λ_{III} = 100° to 180° which is in a different position to and precedes the temperature peak.

4.1.2 Southern Auroral Results

Fitted temperatures for the southern aurora ranged from about 750 K to over 1000 K. There is also evidence for longitudinal variation with a temperature peak around λ_{III} = 180° to 210°. A narrow minimum is observed around λ_{III} = 60°. There also appears to be some latitudinal variation in the auroral region with the top temperature found at latitudes ~55° to ~70° and the pole cooler by up to 200 K.

Line of sight corrected column densities range from about 1.5 $\times$ 10^{12} cm^{-2} to around 16.9 $\times$ 10^{12} cm^{-2}. Longitudinally, the results suggest a distribution different from that of the fitted temperature.

The column density distribution shows a broad peak between λ_{III} = 250° to 50°, which is almost on the opposing side to that of the temperature, and a minimum between

λ_{III} = 150° and 200°.

4.1.3 Result for the Main Body of the Planet

Results derived from fitting to spectra sampling regions on the body of the planet (rows 10 to 18 in figure 4.1) are shown in tables 4.5 to 4.14. Fitted temperatures range from 650 K to over 1000 K. There were "spots" of elevated temperatures, but these may be artifacts of the fitting and are unlikely to be genuine. The associated uncertainties are quite large, up to ±200 K in some cases, and as such the results showed very little indication of latitudinal or longitudinal variation.

Fitted column densities ranged from less than 0.6×10^{12} cm^{-2} to about 1.5×10^{12} cm^{-2}. There appears to be variation with longitude but the uncertainty ranges were too large for this to be confirmed. Latitudinally H_3^+ column density seems to be a minimum around the equator.

4.1.4 Summary of Fitted Parameters

The fitted temperatures are generally higher for the 4.0 μm data than the 3.5 μm data. With the fitted column densities the opposite is true however; 4.0 μm data gave lower numbers than the 3.5 μm data. This may indicate some deviation from local thermal equilibrium, even within the ν_2 fundamental vibrational band. However, it also highlights once more the problems associated with the high (anti) correlation between temperature and column density. No information was available for either the temperature or column density on the body of the planet from the 4.0 μm data due to the high continuum level masking out any H_3^+ emission.

Figures 4.4 and 4.5 show attempts at mapping the fitted temperatures and column densities to determine spatial variability. Footprints of the LCFL and the Io torus are shown as a series of large dots joined by curves. The most striking aspect to be seen in the map is the temperature difference between the northern and southern hemispheres. This is quite unexpected since there has been no prior indication of such asymmetry from previous spectroscopic studies.

Another remarkable feature is that temperature structures seem to follow the footprints quite closely, although offset northward by 5° to 10°. However, the difference is within the latitudinal range encompassed by the detector array pixel size and no significance should be attached to this. Also of note is the cooler region southward of the LCFL.

The column density map (figure 4.5) also shows marked asymmetry between the north and the south. In the north, large column density only occurs over a limited range of longitudes around 100°, while most of the southern aurora exhibits fairly large column density. Peak column density in the north appears to lie just outside of the auroral boundary (footprint of the LCFL), which is puzzling. However, this may be due to latitudinal uncertainty associated with the large pixel size rather than an unknown particle precipitation or energy deposition source. A local minimum in the column density between $\lambda_{III} = 300°$ to 360° coincides with the northern most latitudinal range of the auroral boundary. H_3^+ column density distribution in the south appears largely restricted to the auroral region. There is no peak in the column density such as that seen in the north, but like the north, the local column density minimum occurred at longitudes where the auroral boundary is at its southern most latitude.

Comparing the temperature map to that of the column density map shows that the two differ considerably in the location of their local aurora maxima and minima. In both the north and the south, temperatures peak at regions of local column density minima. This illustrates the point made in chapter 2 about the anti–correlative nature between the model temperature and column density parameters. Separating the two would require much more spectrally extensive data than is available here. Therefore, the temperature and column density distributions described in this section should not be accorded too much significance.

4.2 Combined Spectra

The foregoing section indicates the difficulty in disentangling temperature and column density variations for the individual rows. Interpretation of the data is further confused by the longitudinal dependence of the auroral zones noted previously and the limited

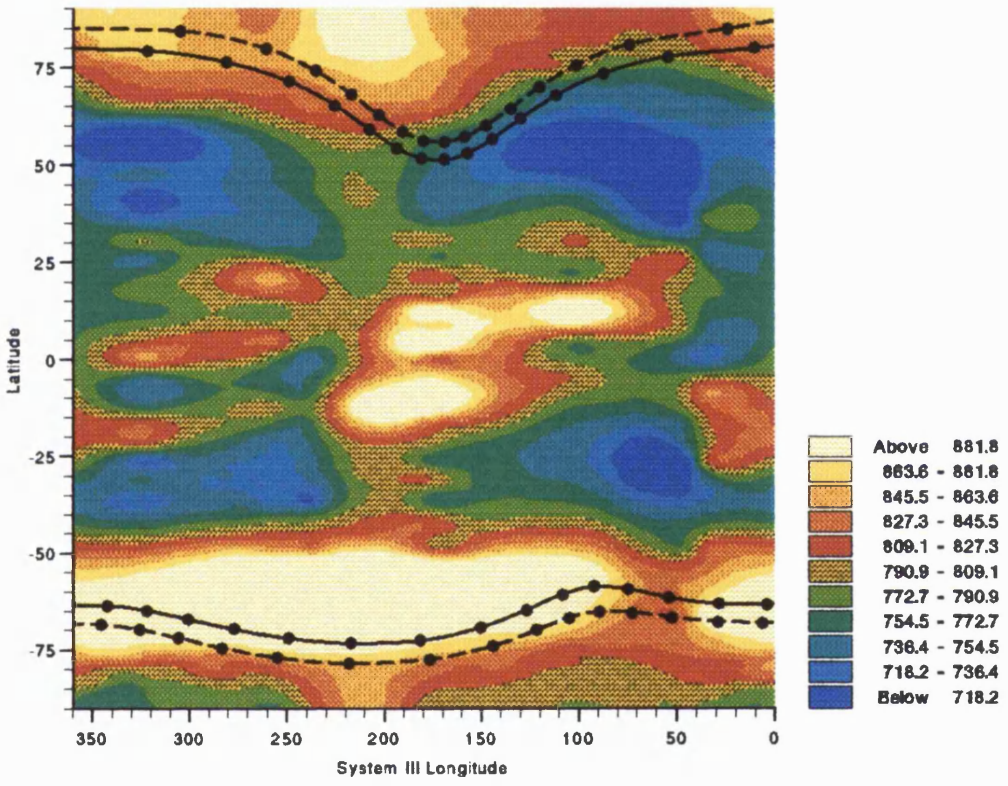

Figure 4.4: Mapping of fitted temperatures onto the surface of Jupiter. Colour shadings associated with temperature ranges are given by the legend to the right of the map. Footprints of the Io Plasma Torus and the LCFL (Connerney 1991, 1993) are shown by curves connecting the dots on the map. Solid curve for the Io Plasma torus and dashed one for the LCFL.

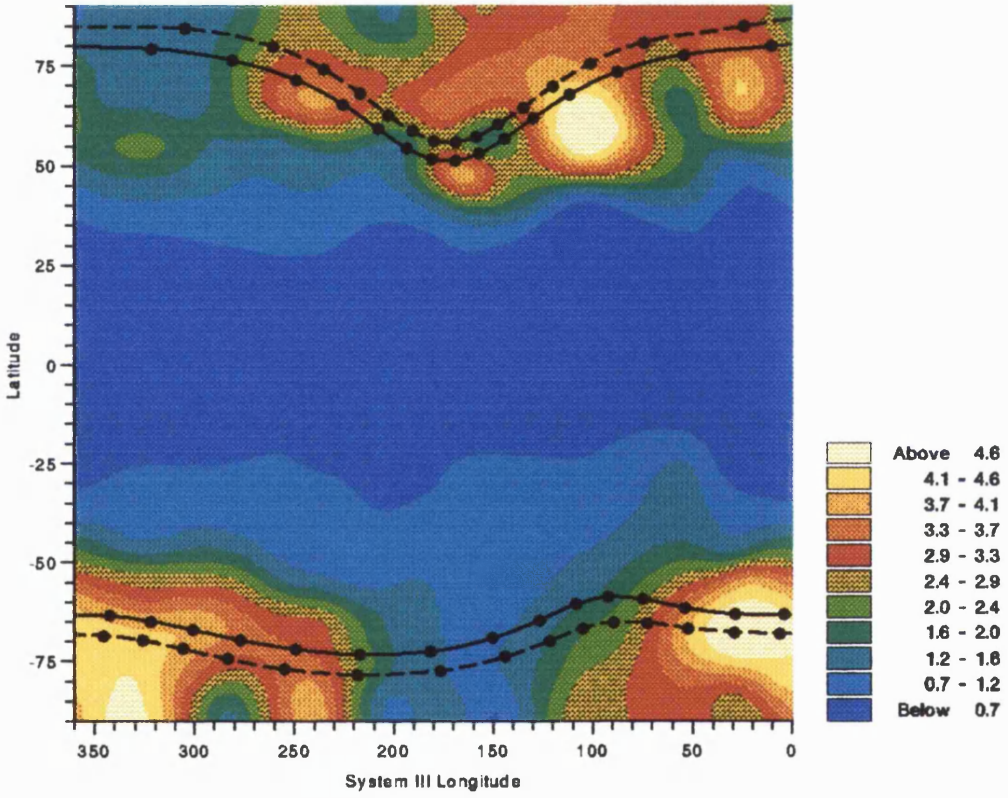

Figure 4.5: Mapping of fitted column densities onto the surface of Jupiter. Colour shadings associated with column density ranges (units of 10^{12} cm^{-2}) are shown by the legend to the right of the map. Footprints of the Io Plasma torus and the LCFL (Connerney 1991, 1993) are shown by curves connecting the dots on the map. Solid curve for the Io Plasma torus and dashed one for the LCFL.

spatial resolution of the spectra.

We, therefore, decided to split each image into five sections sampling different regions of Jupiter. Spectra within each section were combined and fitted to get an overall temperature and column density for that region. The regions decided upon were: (1) north and (5) south (50° to 90° latitude) aurorae, covering about 30,000 km, (2) north and (4) south mid–latitudes (20° to 50° latitude) again covering about 30,000 km and the (3) equator (20° south to 20° north) covering a larger distance of 40,000 km because four spectral rows were binned together instead of three for the other regions. For the 4.0 μm spectra, as previously discussed, only the auroral regions could be probed. Combining the spectra in this way enhances the signal to noise ratio of the resultant spectrum (important for spectra sampling parts of the planet away from the polar regions).

We now introduce a parameter, which we termed "integrated number density," to describe the number density obtained from fitting to the combined spectra. Since we are only interested in the longitudinal profiles of the H_3^+ emission, the integrated number density will be used to denote the number of H_3^+ molecules found in a strip of the planet 1 cm wide, averaged over a distance sub-tending 1″ at the telescope, whose length is equal to the distance bounded by the regions in question. Its dimension will be "molecules cm^{-1}."

Tables 4.23 to 4.24 show results of fitting the combined spectra. The average temperature for the auroral regions is about 800 K. For the mid-latitudes the average temperature is not much lower at around 750 K. Fitted temperatures for the equator are highly variable but the average temperature is about the same as mid-latitudes (750 K). The profiles observed in the fitted temperatures of the individual rows for the northern and southern aurorae are still in evidence here. The average integrated number density for the auroral regions is about 3×10^{22} mols cm^{-1}, however there are large variations ranging from around 6×10^{21} mols cm^{-1} to over 8×10^{22} mols cm^{-1}. Average integrated number density for the mid-latitudes is about 1×10^{22} mols cm^{-1} and for the equator is about 5×10^{21} mols cm^{-1}. The profiles seen in the integrated number densities also match the column densities found in fitting to the individual spectra. For the mid-latitudes and the equator, fitted temperatures seem to be constant (within the estimated errors) around

750 K to 800 K at all longitudes, with a few exceptions.

4.3 Total Emission

In chapter 2 we argued that since there is a strong (anti–)correlation between the model temperature and column density, combining the two parameters to calculate the total emissions observed would give an overall view of H_3^+ throughout the planet.

By assuming LTE we worked out the emissivity per molecule at the fitted temperature and then multiplied this value by the fitted column density to obtain a value for the total emission, $E(H_3^+)$. The total emission results are found to be consistent for the 3.45μm and 4.0μm data.

Values obtained for the total emission and their line of sight corrected values are given in tables 4.5 to 4.22 in the columns $E(H_3^+)$ and $E(H_3^+)^*$ respectively. Those that were estimated to be just off the limb of the planet (i.e. 183 km, 5456 km) are assigned the latitude 90° in subsequent analyses. Figure 4.6 shows an attempt at mapping the computed total emission parameter onto a longitude, latitude grid. The map graphically demonstrates the variability of the emission, highlighting the local minima in the auroral regions and showing that the emissions reaches a minimum around the equator. Figure 4.7 shows 2-D maps of the total emission parameter which are more useful in determining the relationship between the H_3^+ emission and magnetic field parameters such as the auroral boundaries (magnetic shell = 30 R_J footprint) and the Io torus footprints (magnetic shell = 6 R_J), computed using Connerney's O_6 model (1991, 1993).

In general, the main emitting areas appear very close to the auroral boundaries. In the north bright H_3^+ emission is concentrated between λ_{III} = 60° and 200° corresponding with the region where the auroral boundary is at its southern most extent. The emission seems to peak at 150° longitude which corresponds to the region of highest surface magnetic field strength. Outside of this longitudinal range the northern auroral boundary remains very near the pole, coinciding with much lower emission.

In the south, the emission appears to fill most of the polar region. There seems to be a broad maximum beginning around λ_{III} = 250° and extending eastward to about 50°.

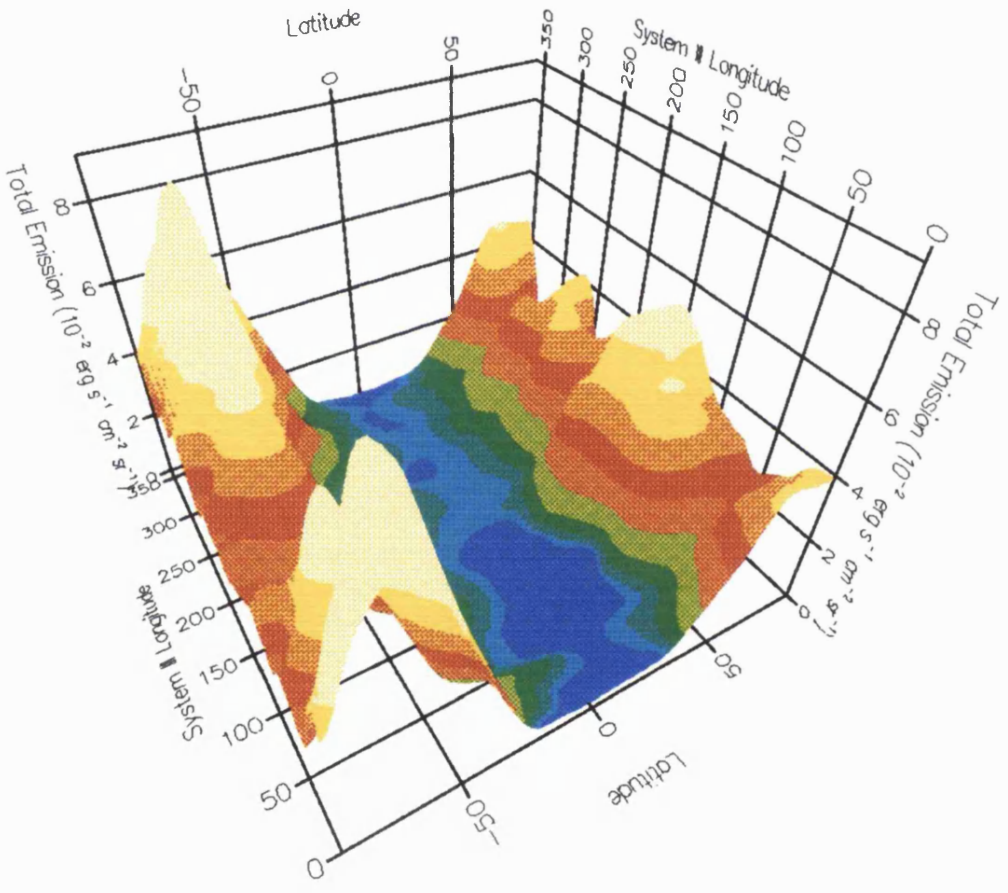

Figure 4.6: 3-D mapping of the computed total emission parameter onto the surface of Jupiter. The emission has been corrected for the limb-brightening effect and is given in units of 10^{-2} erg s^{-1} sr^{-1} cm^{-2}.

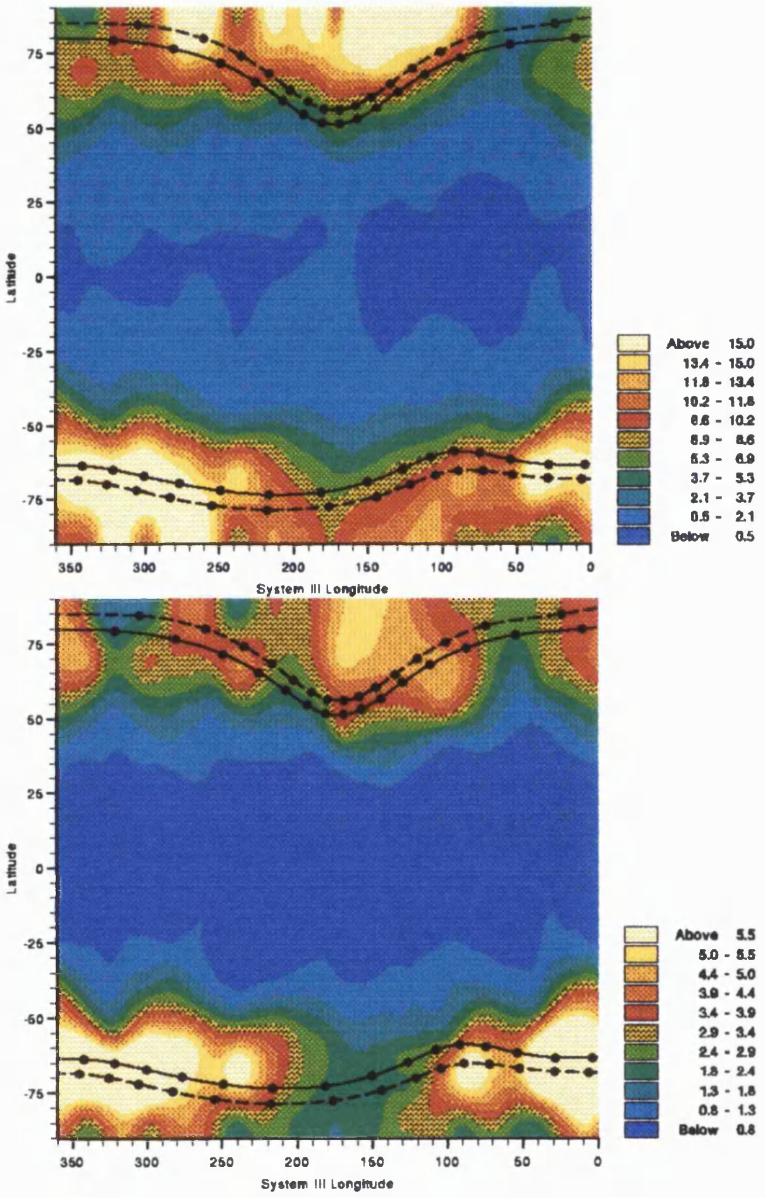

Figure 4.7: 2-D maps of the computed total emission. Colour shadings associated with total emission ranges are shown on the right and is given in units of 10^{-2} erg s^{-1} sr^{-1} cm^{-2}. The bottom map is a limb-brightening corrected version of the top. The auroral boundaries are shown as dashed lines connecting the dots. The Io torus footprints are shown as solid lines connecting the dots. Both were computed using Connerney's O_6 magnetic field model (1991, 1993).

The emission decreases to a local minimum between λ_{III} = 120° and 200°, corresponding to the southern most latitudinal range of the auroral boundary and the Io torus footprint.

There appears to be a big difference in the latitudinal positions of the northern and southern aurorae. The northern aurora seems to be dimmer and the emission almost all coming from regions pole-wards of the Io torus footprint. In contrast the southern auroral is rather bright and extends to a some distance outside of the Io torus footprint. H_3^+ emission at the south pole itself is relatively dim. This may appear to contradict the results from imaging work showing that the northern aurora consists of spots and patches which are generally brighter than the southern auroral features, the appearance of which is diffuse but is more uniform. However, the difference is almost certainly due to inaccuracies in estimating the latitudinal locations of the spectra and the "smearing" effect of the poorer spatial resolution of the spectrometer. The total emission map seems to have a systematic northward shift of about 10° at all longitudes. This is easily within the range of latitudes covered by spectra sampling regions pole-wards of the mid-latitudes.

The asymmetry between the northern and southern auroral H_3^+ emission appears to reflect the asymmetry of the jovian magnetic field. The surface magnetic field strength being higher (10–14 G) and concentrated in a relatively small region in the north compared to the south where the surface field strength remains at around 10 G almost throughout the whole auroral region.

Outside of the auroral regions, between latitudes ± 50°, H_3^+ emission drops to about 10% of the intensity found at the poles. The total emission shows evidence of latitudinal as well as longitudinal variation. If the production of H_3^+ is due to solar EUV alone, then the pole to pole distribution profile would be relatively flat. This is because decreasing solar flux intensity at high latitudes will be offset by the increase in the line of sight effect. The results from mapping the total H_3^+ emission parameter therefore, suggests that solar EUV flux alone cannot account for all of the non-auroral H_3^+ emission. An additional mechanism is required in order to explain the variation in the concentration of H_3^+.

Figures 4.8, 4.9, 4.10 and 4.11 show our attempts at correlating the computed total emission parameter with magnetic field parameters for regions between ± 50° latitude.

The O_6 (Connerney 1991, 1993) model was used to compute the surface magnetic field strength and dip angles. An offset tilted dipole was used to compute the magnetic shell and the loss cone parameters instead of the O_6 model, because it was computationally much simpler and differs little from the O_6 model away from the auroral regions.

Of the four magnetic field parameters, we find the best agreement with the magnetic field dip angles (figure 4.9). We do not find such a correlation with the other magnetic field parameters. The large area of emission minimum around $\lambda_{III} = 100°$, 10° latitude, is coincident with the northern most range of the magnetic dip equator. The region also happens to be close to the location of the H Lyman-α bulge (Clarke 1989, 1991). It would appear that which ever mechanism is responsible for the enhancement of the H Lyman-α emission, is either depressing the formation of H_3^+ in this region, or enhances the H_3^+ emission only outside of the bulge region. Since H Lyman-α emission originates generally at altitudes above the H_3^+ level, a possible mechanism might, therefore, be required to deposit its energy at higher altitudes in the bulge region, and lower down outside of it.

The existence of the H Lyman-α bulge could also be due to thermal broadening of the Hα line as proposed by Jaffel *et al* (1993). They suggested the broadening is due to turbulence in the bulge region. The turbulence may dredge up heavier material, such as methane, from altitudes lower than the H_3^+ peak which can act to reduce the concentration of H_3^+. Alternatively, The broadened Hα may scatter more of the incident solar radiation, thereby reducing the flux penetrating to the H_3^+ peak altitude. However, the wind-speed they suggested, up to 10 km/s, in order to account for the Hα line width is faster than the speed of sound. The supersonic wind speed should produce shocks in the jovian atmosphere, causing localised heating. Such a scenario would have clearly visible signatures, particularly in the infrared. Aside from the H Lyman-α bulge, no shocked gas signature has been observed either from spacecrafts or ground-based telescopes.

4.4 Total Auroral Emission

Total emission were also computed for the combined spectra to get an overall impression of the distribution of auroral H_3^+. Since the signal in each row near to the poles were added

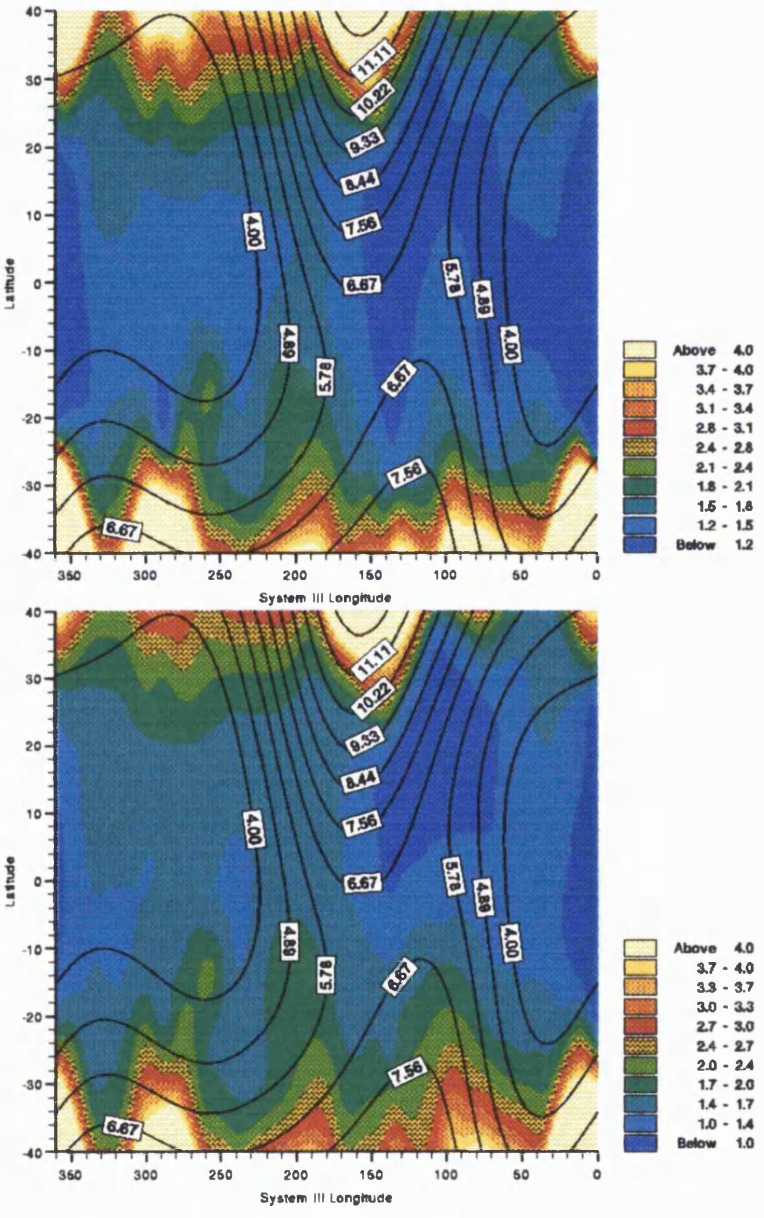

Figure 4.8: Shaded contour maps of the computed total emission for latitudes between $\pm$ 40°. The labelled lines are contours of constant surface magnetic field strength according to the O_6 model. Limb-brightened corrected emission map is shown in b.

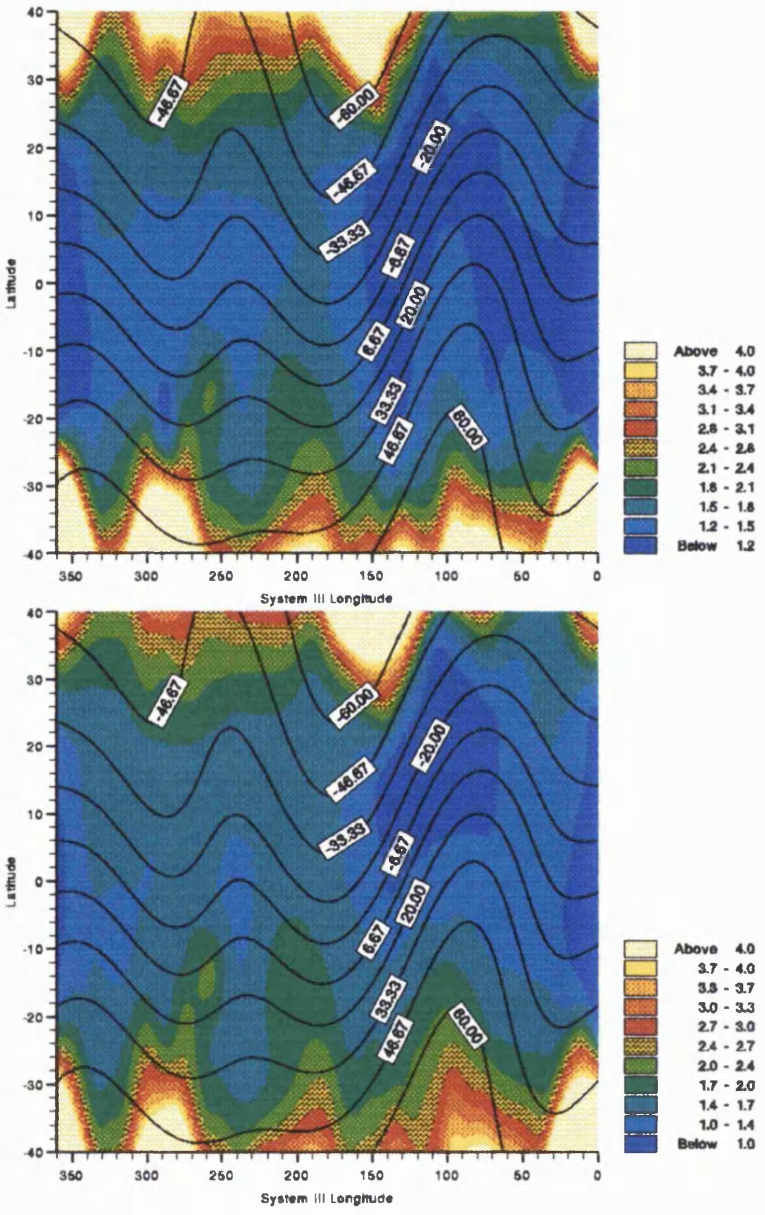

Figure 4.9: A shaded contour map of the computed total emission for latitudes between ± 40°. The labelled lines superimposed on top of the map are contours of constant dip angles of the magnetic field lines according to the O_6 model. Limb-brightened corrected emission map is shown in b.

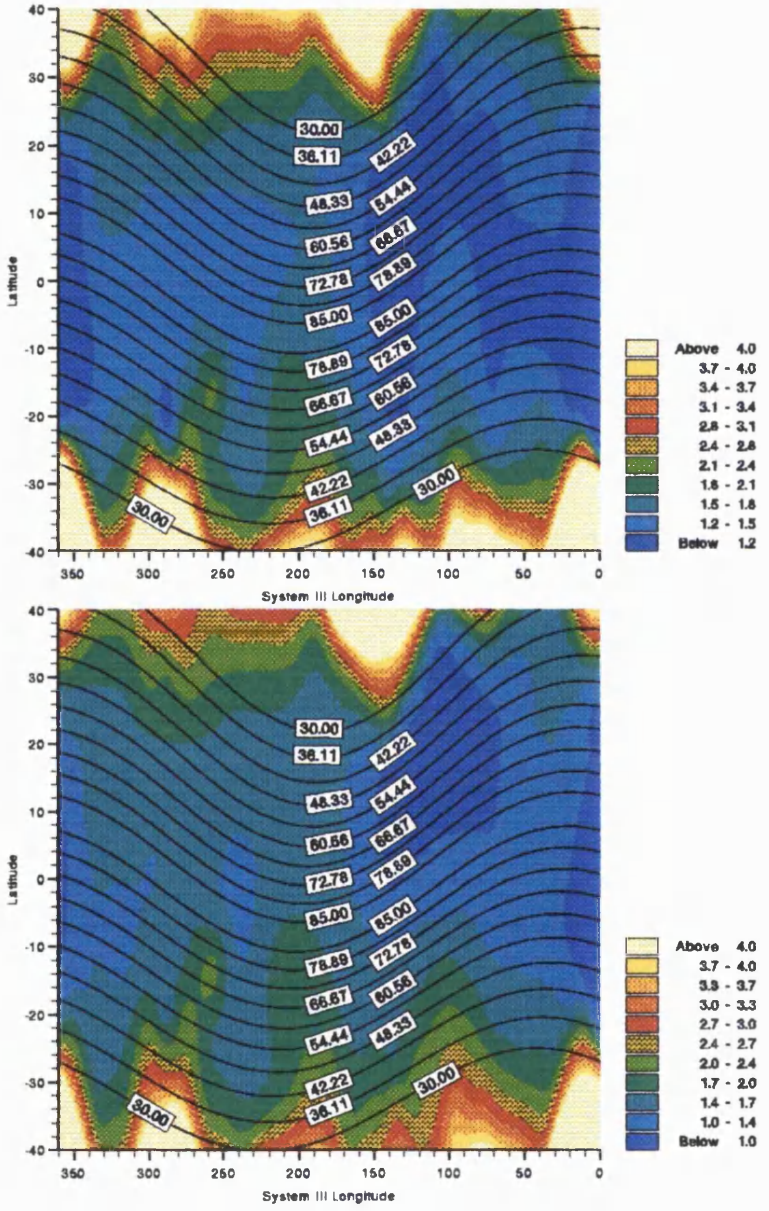

Figure 4.10: A shaded contour map of the computed total emission for latitudes between ± 40°. The labelled lines superimposed on top of the map are contours of constant loss cone angles at the magnetically conjugate equatorial point, according to the offset-tilted dipole model. Limb-brightened corrected emission map is shown in b.

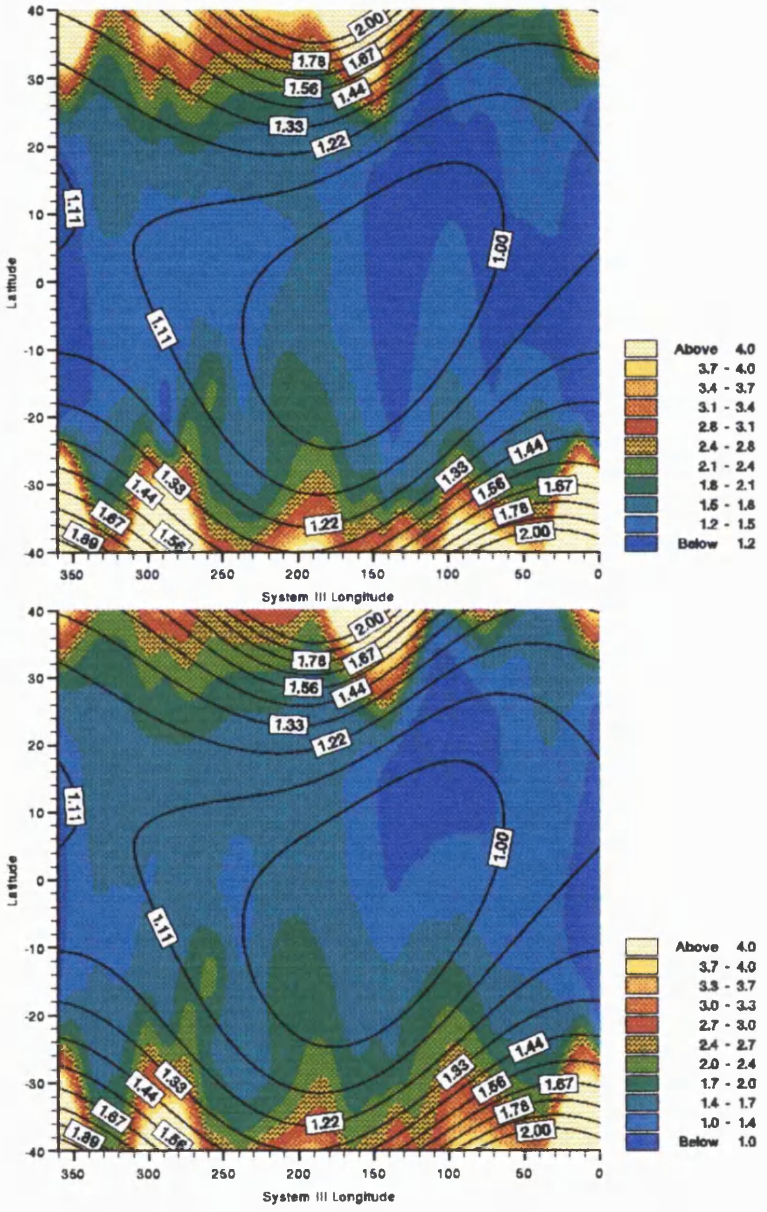

Figure 4.11: A shaded contour map of the computed total emission for latitudes between ± 40°. The labelled lines are the footprints of magnetic shells according to the offset tilted dipole model. Limb-brightened corrected emission is shown in b.

together to form one spectrum for each auroral region, the resultant total emission was thus, computed for a strip of the planet 1 cm wide on Jupiter and of a length sufficient to cover all the rows in which we detect emission due mainly to auroral emission. And because, in this section, we are primarily interested in the longitudinal variation of the H_3^+ emission (the spatial information is degraded by this procedure), we feel that it is inappropriate to express the results in terms of energy per unit area, since it is unlikely that the aurorae would fill completely, the field of view of all three rows simultaneously. The results are expressed in units of ergs s^{-1} sr^{-1} cm^{-1} (E(cml)), to show that the emission is computed for a strip of the planet imaged by a number detector rows simultaneously.

The E(cml) parameter is not to be confused with the computed total emission per unit area normally quoted in this work and elsewhere.

Using the E(cml), parameter we have been able to determine the longitudinal profile of the H_3^+ emission in the aurorae (graphs 4.12 and 4.13). The graphs show that, in the north H_3^+ emission peaks around $\lambda_{III} = 150°$ with perhaps a second, smaller peak around 210°. However, the sparseness of the data means that this remains inconclusive for the time being. In the south the emission shows a broad peak between $\lambda_{III} = 300°$ and 50°, with a minimum between 150° and 200°. The emission profile determined using the E(cml) parameter have enabled us to demonstrate that changes in the auroral H_3^+ emission during the SL9 comet impact with Jupiter occurred only at specific regions in both the north and the south (Miller *et al* 1995).

From these results we have estimated the total power of the auroral output to be 5×10^{12} W sr^{-1} for both the northern and southern aurorae. This is approximately the same amount of power output that has been quoted for the U.V. aurorae (Strobel and Atreya 1983).

4.5 Equatorial Spectra

It has been proposed that formation of H_3^+ outside of the auroral regions is principally due to the incident solar EUV flux, with, perhaps, small contribution from other sources (see section 4.3). If this is the case then we might expect to see a dawn—dusk asymmetry

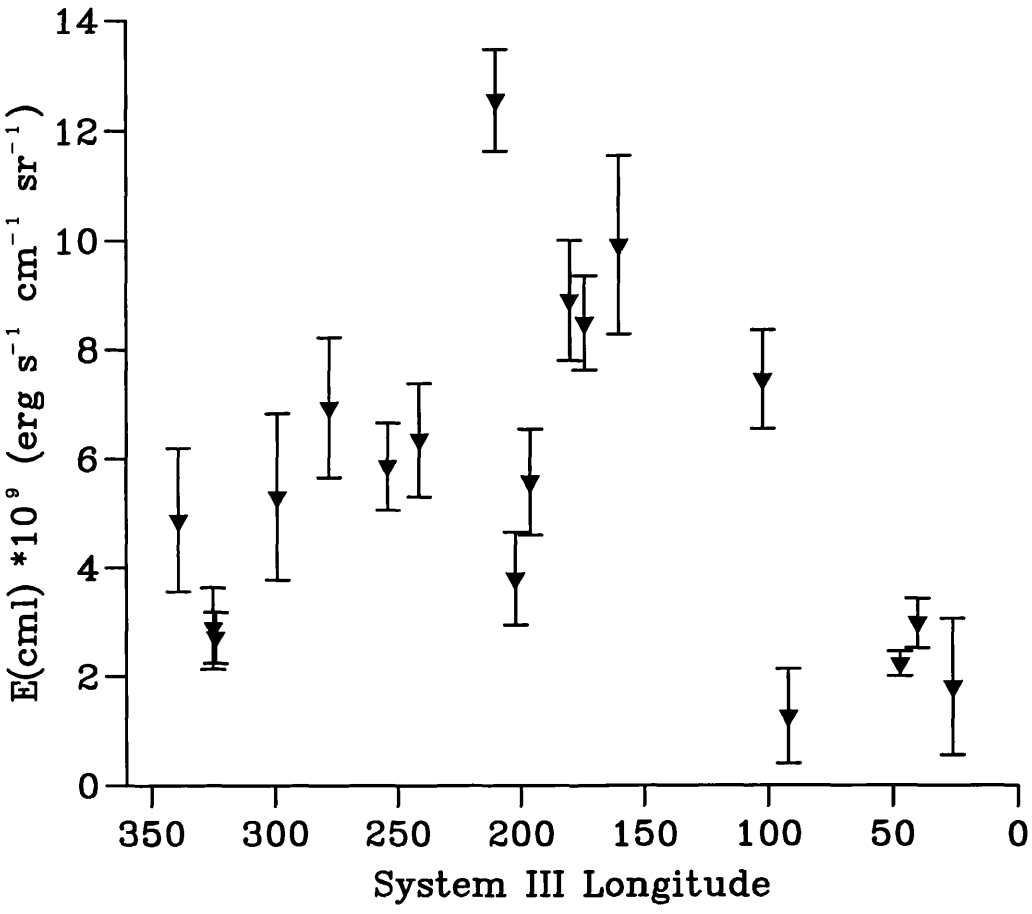

Figure 4.12: Graph of the E(cml) parameter plotted as a function of longitude for the northern auroral region.

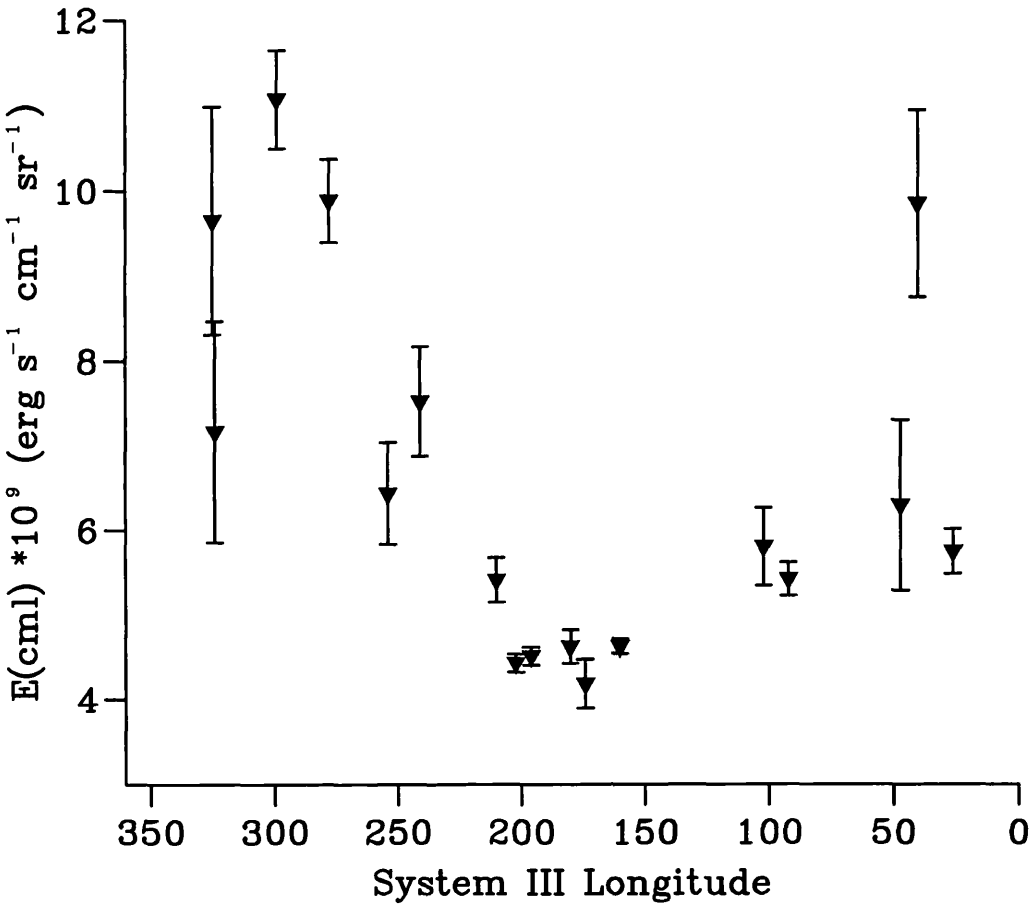

Figure 4.13: Graph of the E(cml) parameter plotted as a function of longitude for the southern auroral region.

effect on the H_3^+ emission. Some of the 2-D spectral images taken with the slit aligned east—west along the equator do show such an asymmetry in the H_3^+ emission lines (see figure 2.9).

The spectra were fitted to obtain values for the temperatures and column densities. These were then converted into total emission as described in the section 4.3. Line of sight corrections were applied and the resultant divided by the local noon time values, since we have evidence of longitudinal variation at the equator. The local noon time values were obtained by interpolating the results of the pole to pole spectra. Tables 4.25 to 4.29 give the results of fitting to the equatorial spectra. Figures 4.14 to 4.18 show graphs of the total emission, total emission corrected for the line of sight effect and the line of sight corrected emission normalised by the noon time value, plotted against their estimated longitudes.

Most of the uncorrected/raw emission graphs appear to show slightly enhanced H_3^+ emission on the western limb of the planet (local afternoon on Jupiter). But one graph also shows enhanced emission on the eastern limb of the planet. Overall, the normalised emission curves do not show any systematic effect expected if diurnal heating by the solar EUV flux were having a measurable effect. Variations in the normalised emission values are generally within the uncertainty limits (estimated to be proportional to those from the pole to pole spectra). Although systematic variability is not observed the data does not rule out the possibility of local time effect on Jupiter.

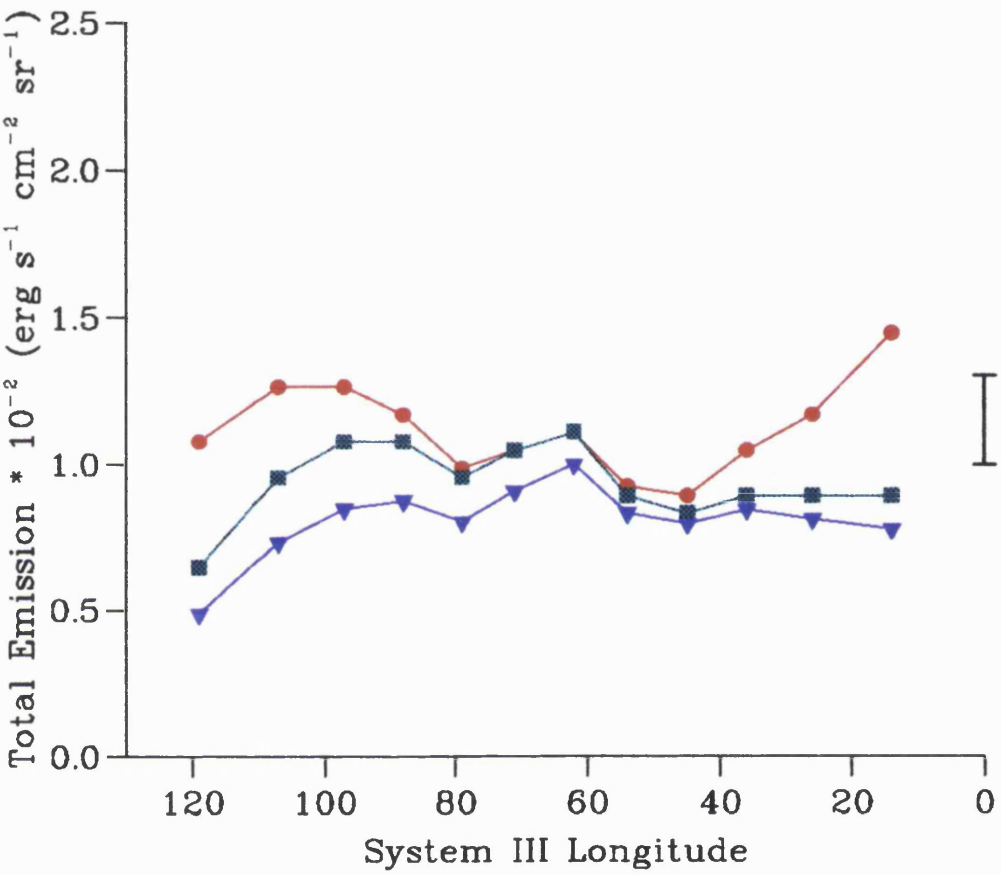

Figure 4.14: Three graphs showing the total emission, corrected for the line of sight effect and normalised to the noon time value. The data were obtained on the 5th of May 1993 at the CML of 67°. Spectra were taken with the slit aligned east—west along the equator. The east (rising) limb is to the left of the graphs. The computed total emission is shown in red, line of sight corrected in green and the blue curve is the total emission normalised to the noon time value and is dimensionless. The black bar to the left of the graph shows an error value which is typical for all the computed total emission.

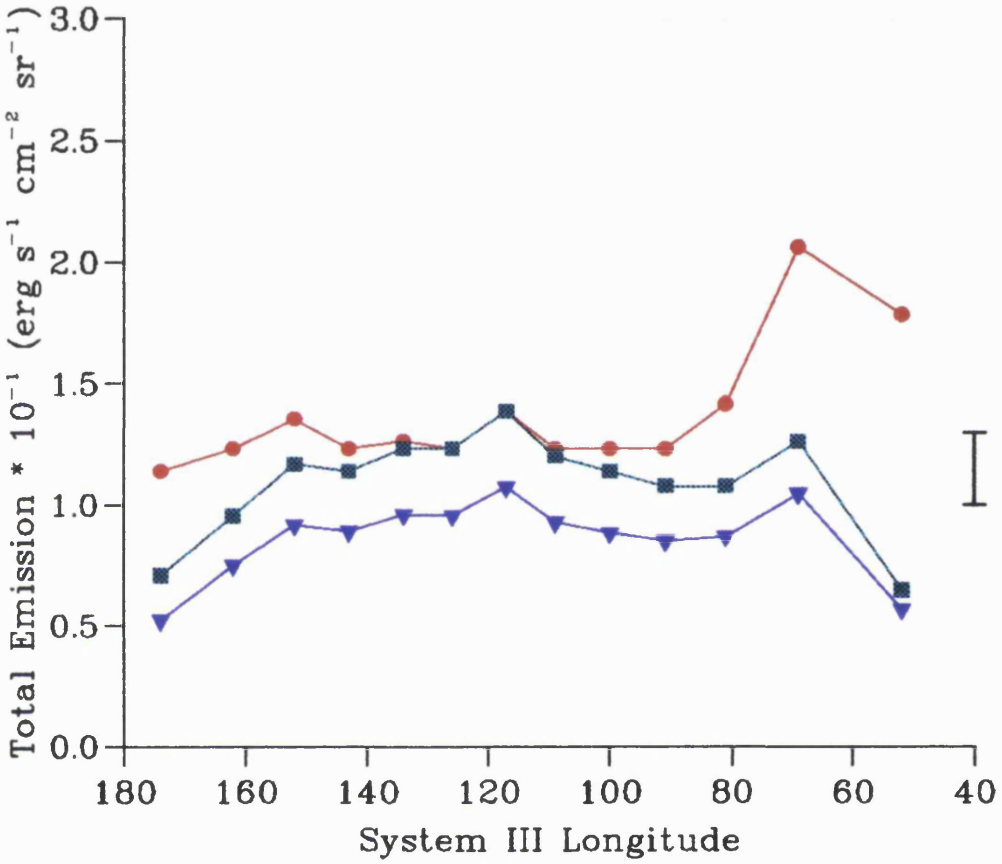

Figure 4.15: Three graphs showing the total emission, corrected for the line of sight effect and normalised to the noon time value. The data were obtained on the 3rd of May 1993 at the CML of 122°. Spectra were taken with the slit aligned east—west along the equator. The east (rising) limb is to the left of the graphs. The computed total emission is shown in red, line of sight corrected in green and the blue curve is the total emission normalised to the noon time value and is dimensionless. The black bar to the left of the graph shows an error value which is typical for all the computed total emission.

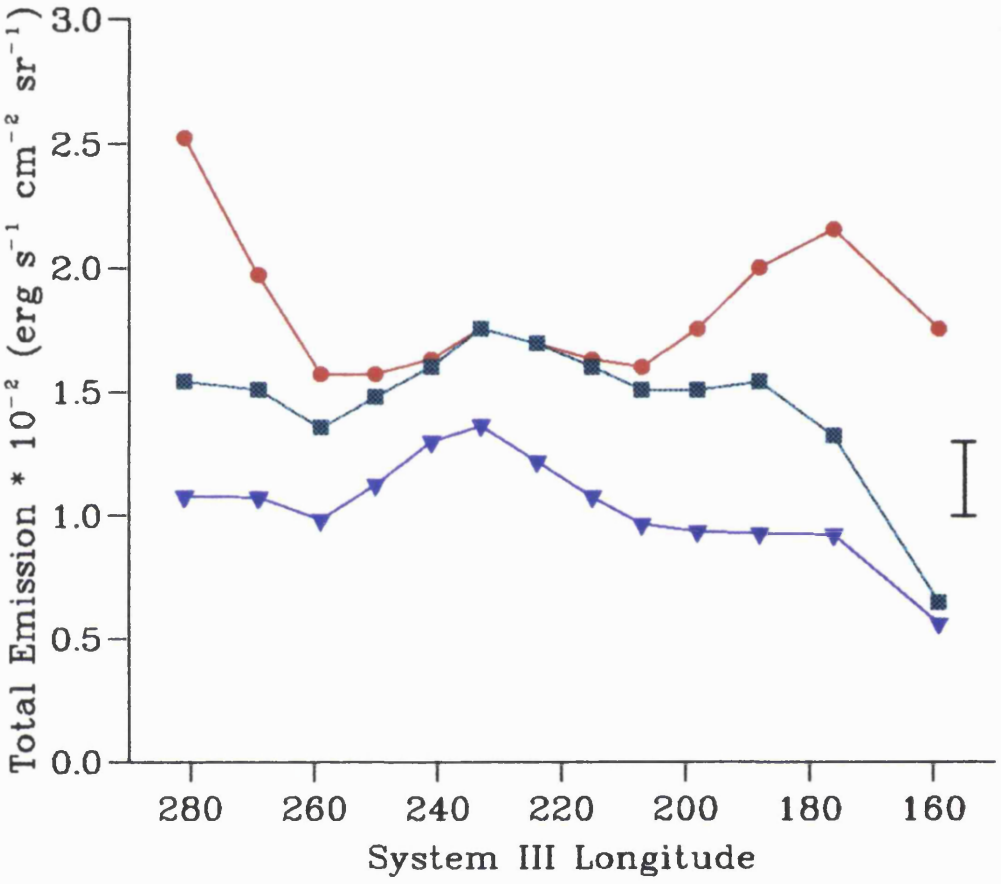

Figure 4.16: Three graphs showing the total emission, corrected for the line of sight effect and normalised to the noon time value. The data were obtained on the 3rd of May 1993 at the CML of 229°. Spectra were taken with the slit aligned east—west along the equator. The east (rising) limb is to the left of the graphs. The computed total emission is shown in red, line of sight corrected in green and the blue curve is the total emission normalised to the noon time value and is dimensionless. The black bar to the left of the graph shows an error value which is typical for all the computed total emission.

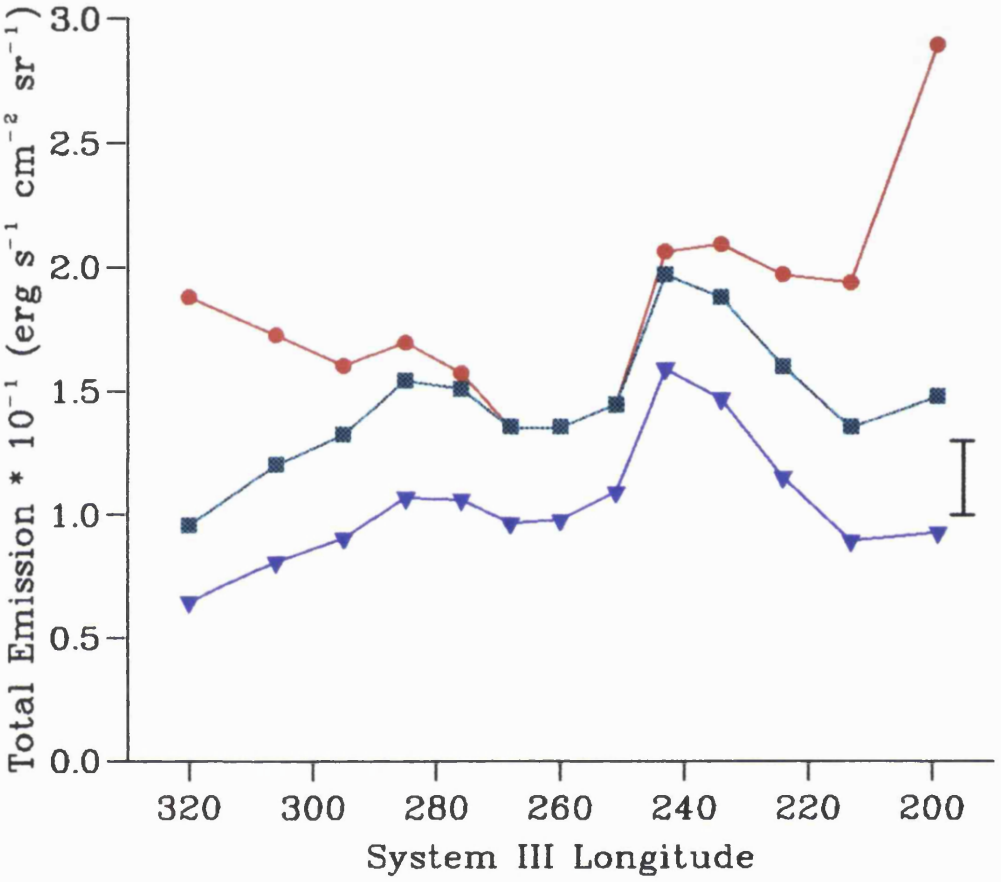

Figure 4.17: Three graphs showing the total emission, corrected for the line of sight effect and normalised to the noon time value. The data were obtained on the 4th of May 1993 at the CML of 260°. Spectra were taken with the slit aligned east—west along the equator. The east (rising) limb is to the left of the graphs. The computed total emission is shown in red, line of sight corrected in green and the blue curve is the total emission normalised to the noon time value and is dimensionless. The black bar to the left of the graph shows an error value which is typical for all the computed total emission.

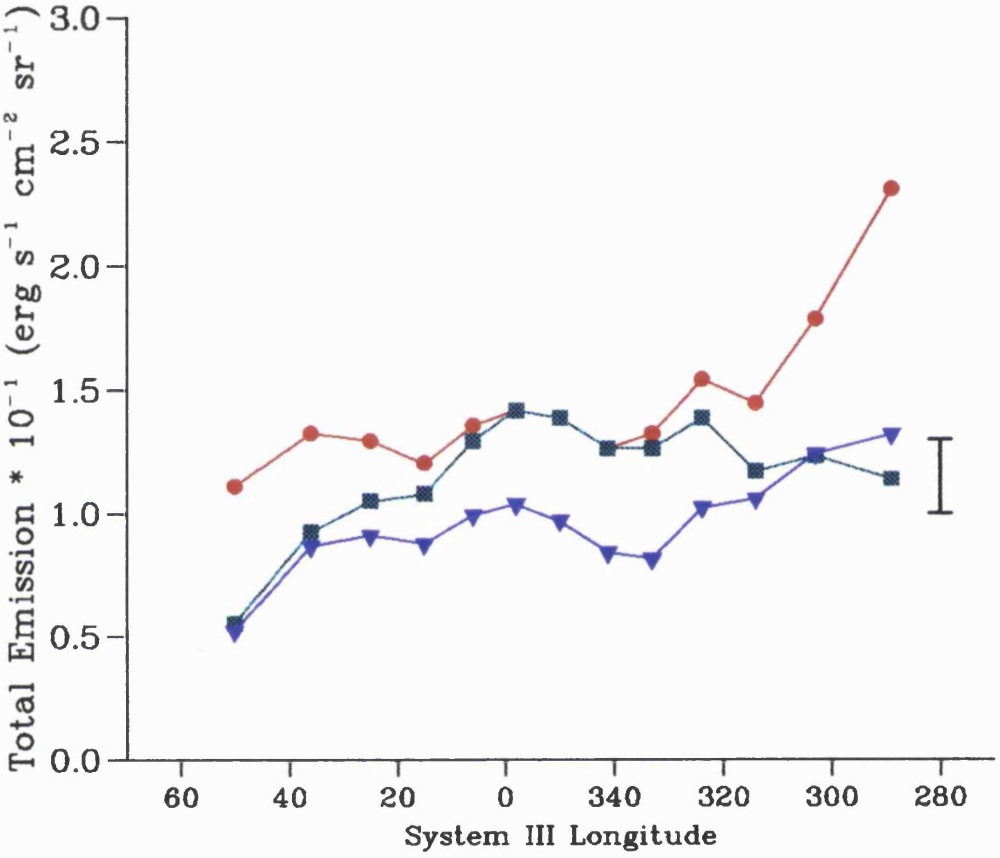

Figure 4.18: Three graphs showing the total emission, corrected for the line of sight effect and normalised to the noon time value. The data were obtained on the 4th of May 1993 at the CML of 350°. Spectra were taken with the slit aligned east—west along the equator. The east (rising) limb is to the left of the graphs. The computed total emission is shown in red, line of sight corrected in green and the blue curve is the total emission normalised to the noon time value and is dimensionless. The black bar to the left of the graph shows an error value which is typical for all the computed total emission.

Row	Lat	T(K)	$N(H_3^+)$	$E(H_3^+)$	L.S.	$N(H_3^+)^*$	$E(H_3^+)^*$	I^*
	km							
22	15800†	728	0.20	0.13	5.0	0.04	0.03	.014
21	5479†	963± 38	0.83±0.15	2.04	5.0	0.17	0.41	.195
20	66N	740± 22	9.68±1.74	7.16	2.3	4.25	3.11	.886
19	48N	741± 34	1.19±0.27	0.89	1.5	0.81	0.60	.108
18	36N	804± 52	0.56±0.18	0.60	1.2	0.46	0.49	.066
17	26N	737± 52	0.71±0.28	0.52	1.1	0.64	0.47	.057
16	16N	775± 58	0.49±0.20	0.45	1.0	0.47	0.43	.052
15	8N	745± 71	0.51±0.28	0.39	1.0	0.50	0.39	.045
14	0	709± 71	0.59±0.34	0.34	1.0	0.59	0.34	.035
13	8S	868±117	0.25±0.15	0.38	1.0	0.25	0.38	.042
12	16S	814± 78	0.39±0.19	0.46	1.0	0.37	0.44	.048
11	26S	842± 68	0.42±0.16	0.57	1.1	0.38	0.51	.059
10	36S	735± 33	1.19±0.32	0.84	1.2	0.97	0.68	.096
9	48S	831± 25	1.64±0.26	2.14	1.5	1.11	1.45	.228
8	66S	920± 32	11.93±0.29	24.45	2.3	5.24	10.63	2.388
7	4540†	684± 28	12.05±0.45	6.03	5.0	2.41	1.21	.704
6	14728†	775±152	0.21±0.18	0.18	5.0	0.04	0.04	.020

Table 4.5: Results of fitting 3.45 μm spectra with the slit aligned pole to pole. The data were obtained on the 4^{th} May 1993 at the CML of 40°. Column densities are given in units of 10^{12} cm^{-2} and total emissions in units of 10^{-1} erg s^{-1} sr^{-1} cm^{-2}.

Row	Lat	T(K)	$N(H_3^+)$	$E(H_3^+)$	L.S.	$N(H_3^+)^*$	$E(H_3^+)^*$	I^*
	km							
22	15966†	749	0.14	0.12	5.0	0.03	0.02	.015
21	5624†	798± 32	0.86±0.17	0.94	5.0	0.17	0.19	.104
20	66N	754± 23	3.81±0.57	3.04	2.3	1.66	1.32	.387
19	48N	651± 26	2.71±0.65	0.98	1.5	1.83	0.66	.131
18	36N	677± 44	1.17±0.47	0.54	1.2	0.95	0.44	.069
17	26N	837± 88	0.35±0.17	0.48	1.1	0.32	0.43	.054
16	16N	782± 70	0.44±0.21	0.44	1.0	0.42	0.42	.049
15	8N	806±100	0.34±0.22	0.37	1.0	0.34	0.37	.042
14	0	735± 84	0.48±0.31	0.34	1.0	0.48	0.34	.041
13	8S	795± 99	0.37±0.23	0.38	1.0	0.37	0.38	.043
12	16S	744± 71	0.64±0.34	0.48	1.0	0.61	0.46	.053
11	26S	651± 36	1.58±0.54	0.56	1.1	1.43	0.51	.076
10	36S	713± 32	1.56±0.37	1.01	1.2	1.27	0.82	.114
9	48S	757± 23	2.78±0.44	2.22	1.5	1.88	1.50	.281
8	66S	825± 25	10.35±1.55	12.93	2.3	4.50	5.62	1.478
7	5624†	667± 20	16.39±2.95	7.05	5.0	3.28	1.41	.829
6	15966†	756± 76	0.32±0.18	0.26	5.0	0.06	0.05	.034

Table 4.6: Results of fitting 3.45 μm spectra with the slit aligned pole to pole. The data were obtained on the 5^{th} May 1993 at the CML of 47°. Column densities are given in units of 10^{12} cm^{-2} and total emissions in units of 10^{-1} erg s^{-1} sr^{-1} cm^{-2}.

Row	Lat	T(K)	$N(H_3^+)$	$E(H_3^+)$	L.S.	$N(H_3^+)^*$	$E(H_3^+)^*$	I*
	km							
22	20785†	841±219	0.15±0.14	0.21	5.0	0.03	0.04	.023
21	10484†	1053± 79	0.44±0.12	1.59	5.0	0.09	0.32	.111
20	183†	822± 20	16.69±1.84	20.02	5.0	3.34	4.00	2.281
19	56N	639± 19	9.26±1.67	3.16	1.8	5.23	1.78	.402
18	42N	763±111	0.64±0.30	0.54	1.3	0.48	0.40	.064
17	30N	823±108	0.31±0.20	0.36	1.2	0.27	0.31	.041
16	21N	761±110	0.37±0.28	0.32	1.1	0.35	0.30	.034
15	12N	976±195	0.16±0.13	0.39	1.0	0.16	0.38	.038
14	4N	761± 96	0.47±0.31	0.40	1.0	0.47	0.40	.041
13	4S	813± 98	0.37±0.23	0.42	1.0	0.37	0.42	.042
12	12S	764± 65	0.61±0.28	0.52	1.0	0.60	0.51	.055
11	21S	741± 56	0.74±0.32	0.54	1.1	0.69	0.50	.061
10	30S	752± 41	1.00±0.30	0.79	1.2	0.86	0.68	.089
9	42S	803± 32	1.38±0.28	1.51	1.3	1.03	1.13	.166
8	56S	943± 28	2.48±0.35	5.57	1.8	1.40	3.14	.510
7	183†	786± 24	13.54±1.76	13.27	5.0	2.71	2.65	1.530
6	10484†	764± 96	0.39±0.26	0.34	5.0	0.08	0.07	.046

Table 4.7: Results of fitting 3.45 μm spectra with the slit aligned pole to pole. The data were obtained on the 3rd May 1993 at the CML of 102°. Column densities are given in units of 10^{12} cm^{-2} and total emissions in units of 10^{-1} erg s^{-1} sr^{-1} cm^{-2}.

Row	Lat	T(K)	$N(H_3^+)$	$E(H_3^+)$	L.S.	$N(H_3^+)^*$	$E(H_3^+)^*$	I*
	km							
22	15966†	999	0.07	0.23	5.0	0.01	0.05	.019
21	5624†	903± 46	0.56±0.13	1.05	5.0	0.11	0.21	.103
20	66N	854± 26	9.62±1.25	14.24	2.3	4.18	6.19	1.532
19	48N	749± 22	7.49±1.20	7.87	1.5	5.06	5.32	.686
18	36N	744± 34	1.43±0.36	1.09	1.2	1.16	0.89	.123
17	26N	749± 52	0.74±0.28	0.59	1.1	0.67	0.53	.064
16	16N	758± 68	0.57±0.28	0.46	1.0	0.55	0.44	.053
15	8N	827± 91	0.35±0.20	0.45	1.0	0.35	0.45	.048
14	0	786± 82	0.46±0.25	0.44	1.0	0.46	0.44	.050
13	8S	920±120	0.24±0.14	0.49	1.0	0.24	0.49	.050
12	16S	773± 70	0.58±0.28	0.53	1.0	0.56	0.51	.064
11	26S	736± 48	0.88±0.31	0.61	1.1	0.79	0.55	.068
10	36S	732± 33	1.20±0.31	0.83	1.2	0.98	0.68	.101
9	48S	768± 31	1.66±0.35	1.44	1.5	1.12	0.97	.173
8	66S	918± 37	2.61±0.42	5.36	2.3	1.13	2.33	.563
7	5624†	780± 23	8.81±1.41	8.46	5.0	1.76	1.69	.981
6	15966†	635±146	0.75±0.48	0.23	5.0	0.15	0.05	.033

Table 4.8: Results of fitting 3.45 μm spectra with the slit aligned pole to pole. The data were obtained on the 5^{th} May 1993 at the CML of 174°. Column densities are given in units of 10^{12} cm^{-2} and total emissions in units of 10^{-1} erg s^{-1} sr^{-1} cm^{-2}.

Row	Lat	T(K)	$N(H_3^+)$	$E(H_3^+)$	L.S.	$N(H_3^+)^*$	$E(H_3^+)^*$	I^*
	km							
22	20785†	885	0.28	0.46	5.0	0.06	0.09	.047
21	10484†	976± 39	1.21±0.11	3.16	5.0	0.24	0.63	.291
20	183†	861± 26	14.27±2.00	21.42	5.0	2.85	4.28	2.323
19	56N	764± 23	4.75±0.62	4.04	1.8	2.68	2.28	.483
18	42N	741± 34	1.34±0.35	0.98	1.3	1.00	0.73	.114
17	30N	816± 74	0.49±0.23	0.57	1.2	0.42	0.49	.065
16	21N	847± 93	0.35±0.19	0.48	1.1	0.33	0.45	.054
15	12N	967	0.19	0.47	1.0	0.19	0.46	.046
14	4N	1025	0.18	0.56	1.0	0.18	0.56	.047
13	4S	890±116	0.27±0.16	0.47	1.0	0.27	0.47	.050
12	12S	948±104	0.26±0.12	0.59	1.0	0.25	0.58	.054
11	21S	805± 56	0.59±0.22	0.65	1.1	0.55	0.61	.080
10	30S	835± 46	0.75±0.20	1.00	1.2	0.64	0.86	.110
9	42S	840± 34	1.16±0.22	1.55	1.3	0.87	1.16	.176
8	56S	1017± 46	2.13±0.38	4.47	1.8	1.20	2.53	.614
7	183†	792± 24	8.21±1.23	8.53	5.0	1.64	1.71	.964

Table 4.9: Results of fitting 3.45 μm spectra with the slit aligned pole to pole. The data were obtained on the 3rd May 1993 at the CML of 180°. Column densities are given in units of 10^{12} cm^{-2} and total emissions in units of 10^{-1} erg s^{-1} sr^{-1} cm^{-2}.

Row	Lat	T(K)	$N(H_3^+)$	$E(H_3^+)$	L.S.	$N(H_3^+)^*$	$E(H_3^+)^*$	I^*
	km							
22	20785†	826±74	0.15	0.25	5.0	0.03	0.05	.031
21	10484†	1022±51	0.46±0.09	1.47	5.0	0.09	0.29	.117
20	183†	941±24	9.00±0.90	19.87	5.0	1.80	3.97	1.942
19	56N	807±19	2.64±0.42	2.90	1.8	1.49	1.63	.336
18	42N	819±28	1.15±0.21	1.37	1.3	0.86	1.02	.151
17	30N	789±52	0.69±0.25	0.69	1.2	0.59	0.59	.082
16	21N	772±66	0.60±0.28	0.55	1.1	0.56	0.51	.061
15	12N	782±74	0.53±0.28	0.50	1.0	0.52	0.49	.059
14	4N	814±79	0.39±0.18	0.46	1.0	0.39	0.46	.053
13	4S	830±78	0.42±0.20	0.54	1.0	0.42	0.54	.060
12	12S	952±86	0.28±0.11	0.67	1.0	0.27	0.65	.064
11	21S	814±53	0.60±0.19	0.70	1.1	0.56	0.65	.080
10	30S	809±44	0.72±0.21	0.59	1.2	0.62	0.51	.093
9	42S	832±33	0.99±0.21	1.31	1.3	0.74	0.98	.152
8	56S	998±40	1.44±0.23	6.73	1.8	0.81	3.79	.397
7	183†	856±26	8.94±1.16	13.41	5.0	1.79	2.68	1.490
6	10484†	732	0.26	0.19	5.0	0.05	0.04	.023

Table 4.10: Results of fitting 3.45 μm spectra with the slit aligned pole to pole. The data were obtained on the 3rd May 1993 at the CML of 210°. Column densities are given in units of 10^{12} cm^{-2} and total emissions in units of 10^{-1} erg s^{-1} sr^{-1} cm^{-2}.

Row	Lat	T(K)	$N(H_3^+)$	$E(H_3^+)$	L.S.	$N(H_3^+)^*$	$E(H_3^+)^*$	I*
	km							
22	14728†	826±74	0.31±0.14	0.38	5.0	0.06	0.08	.035
21	4540†	936±38	2.44±0.39	5.36	5.0	0.49	1.07	.462
20	64N	840±30	9.91±1.59	13.38	2.3	4.35	5.87	1.465
19	47N	767±23	2.10±0.38	1.84	1.5	1.42	1.25	.200
18	35N	736±30	1.32±0.30	0.97	1.2	1.07	0.79	.116
17	25N	746±41	0.75±0.24	0.58	1.1	0.68	0.52	.068
16	16N	828±66	0.40±0.16	0.52	1.0	0.38	0.50	.052
15	8N	798±73	0.41±0.19	0.45	1.0	0.41	0.45	.048
14	0	710±50	0.67±0.27	0.40	1.0	0.67	0.40	.046
13	8S	740±70	0.52±0.28	0.38	1.0	0.51	0.38	.040
12	16S	746±56	0.55±0.24	0.43	1.0	0.53	0.41	.050
11	25S	736±52	0.73±0.28	0.52	1.1	0.66	0.47	.058
10	35S	680±30	1.50±0.43	0.68	1.2	1.22	0.55	.084
9	47S	806±32	1.28±0.26	1.41	1.5	0.87	0.95	.164
8	64S	962±38	7.57±1.14	18.53	2.3	3.32	8.13	1.802
7	4540†	605±24	21.60±5.62	5.18	5.0	4.32	1.04	.712
6	14728†	686	0.18	0.09	5.0	0.04	0.02	.015

Table 4.11: Results of fitting 3.45 μm spectra with the slit aligned pole to pole. The data were obtained on the 4^{th} May 1993 at the CML of 241°. Column densities are given in units of 10^{12} cm^{-2} and total emissions in units of 10^{-1} erg s^{-1} sr^{-1} cm^{-2}.

Row	Lat	T(K)	$N(H_3^+)$	$E(H_3^+)$	L.S.	$N(H_3^+)^*$	$E(H_3^+)^*$	I^*
	km							
22	20785†	1037	0.07	0.24	5.0	0.01	0.05	.021
21	10484†	994±50	0.53±0.11	1.53	5.0	0.11	0.31	.134
20	183†	841±21	13.08±1.44	17.66	5.0	2.62	3.53	1.972
19	56N	767±23	2.12±0.36	1.86	1.8	1.20	1.05	.223
18	42N	751±30	1.41±0.30	1.10	1.4	1.05	0.82	.134
17	30N	741±41	1.05±0.35	0.77	1.2	0.90	0.66	.089
16	21N	884±80	0.36±0.03	0.56	1.1	0.34	0.52	.060
15	12N	760±72	0.52±0.28	0.44	1.0	0.51	0.43	.049
14	4N	853±98	0.33±0.18	0.49	1.0	0.33	0.49	.048
13	4S	756±84	0.49±0.30	0.40	1.0	0.49	0.40	.050
12	12S	819±82	0.41±0.20	0.84	1.0	0.40	0.82	.053
11	21S	730±51	0.81±0.32	0.55	1.1	0.76	0.51	.067
10	30S	737±48	0.95±0.34	0.67	1.2	0.82	0.58	.086
9	42S	805±36	1.08±0.25	1.19	1.3	0.81	0.89	.141
8	56S	993±50	2.37±0.50	6.69	1.8	1.34	3.77	.649
7	183†	762±23	17.07±2.73	14.51	5.0	3.41	2.90	1.802
6	10484†	772	0.23	0.20	5.0	0.05	0.04	.024

Table 4.12: Results of fitting 3.45 μm spectra with the slit aligned pole to pole. The data were obtained on the 3rd May 1993 at the CML of 254°. Column densities are given in units of 10^{12} cm^{-2} and total emissions in units of 10^{-1} erg s^{-1} sr^{-1} cm^{-2}.

Row	Lat	T(K)	$N(H_3^+)$	$E(H_3^+)$	L.S.	$N(H_3^+)^*$	$E(H_3^+)^*$	I^*
	km							
22	20785†	996	0.04	0.11	5.0	0.00	0.02	.011
21	10484†	924±120	0.21±0.12	0.44	5.0	0.04	0.09	.042
20	183†	878± 31	4.07±0.65	6.70	5.0	0.81	1.34	.763
19	56N	639± 22	5.92±1.36	2.01	1.8	3.34	1.13	.282
18	42N	699± 35	1.77±0.50	0.96	1.3	1.32	0.72	.124
17	30N	808± 64	0.56±0.24	0.65	1.2	0.48	0.56	.072
16	21N	774± 58	0.59±0.24	0.53	1.1	0.55	0.49	.064
15	12N	756± 62	0.64±0.28	0.54	1.0	0.62	0.53	.059
14	4N	812± 90	0.42±0.23	0.48	1.0	0.42	0.48	.052
13	4S	744± 74	0.54±0.30	0.41	1.0	0.54	0.41	.050
12	12S	755± 83	0.49±0.30	0.40	1.0	0.48	0.39	.052
11	21S	833± 92	0.42±0.22	0.54	1.1	0.39	0.50	.060
10	30S	766± 54	0.66±0.24	0.57	1.2	0.57	0.49	.070
9	42S	757± 38	1.21±0.33	1.01	1.3	0.90	0.75	.126
8	56S	891± 36	1.96±0.33	3.43	1.8	1.10	1.93	.380
7	183†	766± 23	23.41±3.98	22.38	5.0	4.68	4.48	2.542
6	10484†	584± 41	2.89±1.39	0.55	5.0	0.58	0.11	.072

Table 4.13: Results of fitting 3.45 μm spectra with the slit aligned pole to pole. The data were obtained on the 3rd May 1993 at the CML of 324°. Column densities are given in units of 10^{12} cm^{-2} and total emissions in units of 10^{-1} erg s^{-1} sr^{-1} cm^{-2}.

Row	Lat	T(K)	$N(H_3^+)$	$E(H_3^+)$	L.S.	$N(H_3^+)^*$	$E(H_3^+)^*$	I^*
	km							
22	15800†	784±126	0.20±0.16	0.19	5.0	0.04	0.04	.023
21	5479†	918± 41	1.16±0.23	2.38	5.0	0.23	0.48	.226
20	66N	818± 39	10.49±1.68	12.59	5.0	2.10	2.52	1.448
19	48N	752± 60	1.74±0.37	1.40	1.7	1.01	0.81	.170
18	36N	720± 68	1.29±0.32	0.82	1.3	0.97	0.62	.101
17	26N	733± 30	0.82±0.28	0.57	1.2	0.71	0.49	.064
16	16N	783± 29	0.55±0.23	0.54	1.1	0.51	0.50	.058
15	8N	790± 64	0.49±0.23	0.50	1.0	0.48	0.49	.052
14	0N	875± 46	0.28±0.15	0.46	1.0	0.28	0.46	.044
13	8S	731±144	0.61±0.29	0.42	1.0	0.61	0.42	.046
12	16S	834± 12	0.38±0.16	0.50	1.0	0.37	0.49	.055
11	26S	695± 45	1.02±0.37	0.53	1.1	0.95	0.49	.063
10	36S	712± 36	1.24±0.37	0.75	1.2	1.07	0.65	.083
9	48S	814± 32	1.40±0.27	1.60	1.3	1.06	1.21	.180
8	66S	961± 38	7.45±1.27	14.89	1.7	4.31	8.61	1.683
7	5479†	707± 24	23.84±4.77	14.07	5.0	4.77	2.81	1.674
6	15800†	751± 72	0.37±0.20	0.29	5.0	0.07	0.06	.034

Table 4.14: Results of fitting 3.45 μm spectra with the slit aligned pole to pole. The data were obtained on the 4^{th} May 1993 at the CML of 325°. Column densities are given in units of 10^{12} cm^{-2} and total emissions in units of 10^{-1} erg s^{-1} sr^{-1} cm^{-2}.

Row	Lat	T(K)	$N(H_3^+)$	$E(H_3^+)$	L.S.	$N(H_3^+)^*$	$E(H_3^+)^*$	I*
	km							
20	453†	994±283	1.28±1.19	3.70	5.0	0.26	0.74	.705
8	56S	903± 46	8.13±1.71	15.47	1.8	4.54	8.64	2.144
7	453†	1009± 80	0.90±0.29	2.76	5.0	0.18	0.55	.307

Table 4.15: Results of fitting 4.0 μm spectra with the slit aligned pole to pole. The data were obtained on the 5th May 1993 at the CML of 26°. Column densities are given in units of 10^{12} cm^{-2} and total emissions in units of 10^{-1} erg s^{-1} sr^{-1} cm^{-2}.

Row	Lat	T(K)	$N(H_3^+)$	$E(H_3^+)$	L.S.	$N(H_3^+)^*$	$E(H_3^+)^*$	I*
	km							
20	453†	970±140	1.38±0.81	3.59	5.0	0.28	0.72	.557
8	56S	978± 49	3.87±0.81	14.92	1.8	2.16	8.34	1.463
7	453†	864± 48	4.16±1.12	6.45	5.0	0.83	1.29	.851

Table 4.16: Results of fitting 4.0 μm spectra with the slit aligned pole to pole. The data were obtained on the 5th May 1993 at the CML of 92°. Column densities are given in units of 10^{12} cm^{-2} and total emissions in units of 10^{-1} erg s^{-1} sr^{-1} cm^{-2}.

Row	Lat	T(K)	$N(H_3^+)$	$E(H_3^+)$	L.S.	$N(H_3^+)^*$	$E(H_3^+)^*$	I*
	km							
21	10484†	904± 64	0.75±0.23	1.44	5.0	0.15	0.29	.203
20	183†	903± 36	14.25±2.28	27.13	5.0	2.85	5.43	3.574
19	56N	961±216	2.23±1.87	5.59	1.8	1.26	3.15	1.066
8	56S	970±296	1.07±1.03	2.80	1.8	0.60	1.58	.634
7	183†	1019± 51	3.44±0.65	10.98	5.0	0.69	2.20	1.196

Table 4.17: Results of fitting 4.0 μm spectra with the slit aligned pole to pole. The data were obtained on the 3rd May 1993 at the CML of 160°. Column densities are given in units of 10^{12} cm^{-2} and total emissions in units of 10^{-1} erg s^{-1} sr^{-1} cm^{-2}.

Row	Lat	T(k)	$N(H_3^+)$	$E(H_3^+)$	L.S.	$N(H_3^+)^*$	$E(H_3^+)^*$	I*
	km							
21	10484†	918±82	0.52±0.21	1.08	5.0	0.10	0.22	.138
20	183†	917±32	8.00±1.20	16.33	5.0	1.60	3.27	2.033
19	56N	1089	0.93	3.86	1.2	0.52	2.18	.752
7	183†	974±48	4.60±0.92	12.19	5.0	0.92	2.44	1.476

Table 4.18: Results of fitting 4.0 μm spectra with the slit aligned pole to pole. The data were obtained on the 3rd May 1993 at the CML of 196°. Column densities are given in units of 10^{12} cm^{-2} and total emissions in units of 10^{-1} erg s^{-1} sr^{-1} cm^{-2}.

Row	Lat	T(K)	$N(H_3^+)$	$E(H_3^+)$	L.S.	$N(H_3^+)^*$	$E(H_3^+)^*$	I*
	km							
21	10795†	974±151	0.37±0.23	0.98	5.0	0.07	0.20	.122
20	453†	904± 45	5.75±1.09	11.00	5.0	1.15	2.20	1.481
8	56S	981±128	1.97±1.04	5.39	1.8	1.10	3.01	.941
7	453†	989± 54	3.03±0.64	8.55	5.0	0.61	1.71	1.037

Table 4.19: Results of fitting 4.0 μm spectra with the slit aligned pole to pole. The data were obtained on the 5th May 1993 at the CML of 202°. Column densities are given in units of 10^{12} cm^{-2} and total emissions in units of 10^{-1} erg s^{-1} sr^{-1} cm^{-2}.

Row	Lat	T(K)	$N(H_3^+)$	$E(H_3^+)$	L.S.	$N(H_3^+)^*$	$E(H_3^+)^*$	I*
	km							
21	10484†	953±72	0.69±0.21	1.68	5.0	0.14	0.34	.214
20	183†	986±50	7.42±1.56	20.70	5.0	1.48	4.14	2.461
8	56S	919±69	5.05±1.67	10.40	1.8	2.85	5.86	1.568
7	183†	1016±56	6.77±1.42	21.34	5.0	1.35	4.27	2.444

Table 4.20: Results of fitting 4.0 μm spectra with the slit aligned pole to pole. The data were obtained on the 3rd May 1993 at the CML of 278°. Column densities are given in units of 10^{12} cm^{-2} and total emissions in units of 10^{-1} erg s^{-1} sr^{-1} cm^{-2}.

Row	Lat	T(K)	$N(H_3^+)$	$E(H_3^+)$	L.S.	$N(H_3^+)^*$	$E(H_3^+)^*$	I*
	km							
21	5497†	924±37	3.03±0.52	6.39	5.0	0.61	1.28	.852
20	66N	1041±99	3.01±1.11	10.48	2.4	1.24	4.30	1.338
8	66S	964±38	10.57±1.80	26.81	2.4	4.34	11.00	3.136
7	5497†	1043±78	2.34±0.68	8.19	5.0	0.47	1.64	.936

Table 4.21: Results of fitting 4.0 μm spectra with the slit aligned pole to pole. The data were obtained on the 4^{th} May 1993 at the CML of 299°. Column densities are given in units of 10^{12} cm^{-2} and total emissions in units of 10^{-1} erg s^{-1} sr^{-1} cm^{-2}.

Row	Lat	T(K)	$N(H_3^+)$	$E(H_3^+)$	L.S.	$N(H_3^+)^*$	$E(H_3^+)^*$	I*
	km							
21	5479†	931±47	1.45±0.32	3.17	5.0	0.29	0.63	.401
20	66N	1035±78	3.61±1.12	12.28	2.4	1.48	5.04	1.445
8	66S	938±38	10.50±1.16	23.64	2.4	4.31	9.71	3.007
7	5479†	1038±58	2.31±0.51	7.94	5.0	0.46	1.59	.861

Table 4.22: Results of fitting 4.0 μm spectra with the slit aligned pole to pole. The data were obtained on the 5^{th} May 1993 at the CML of 339°. Column densities are given in units of 10^{12} cm^{-2} and total emissions in units of 10^{-1} erg s^{-1} sr^{-1} cm^{-2}.

Table 4.23: Tables of fitted temperatures and column densities obtained by combining rows sampling the regions described.

Fitted Temperatures for the Combined 3.45 μm Spectra										
	Longitude									
Region	40	47	102	174	180	210	241	254	324	325
1	781± 24	740±22	805± 20	826±24	861± 26	928±28	854± 30	840±27	814± 28	824±25
2	762± 42	741±48	750± 64	724±40	793± 52	794±36	748± 34	770±34	715± 36	707±32
3	726± 67	729±52	799± 72	810±73	955±110	834±62	773± 48	806±72	748± 52	792±57
4	786± 44	684±31	769± 31	735±30	827± 33	824±37	687± 31	772±38	769± 42	746±30
5	868± 26	767±23	823± 24	822±25	879± 26	883±26	863± 30	826±24	770± 27	837±26

Fitted column densities for the combined 3.45 μm spectra given in units of 10^{21} mols cm^{-1}										
	Longitude									
Region	40	47	102	174	180	210	241	254	324	325
1	31.8± 4.8	20.7± 3.1	68.1± 8.2	51.3± 6.7	58.4± 7.0	35.6± 3.9	43.2± 6.9	47.5± 5.7	23.4± 4.0	40.3± 6.0
2	5.7± 1.7	5.8± 2.2	4.8± 2.2	9.8± 2.8	6.1± 2.1	7.7± 1.8	8.2± 2.0	8.5± 2.0	10.5± 3.0	10.1± 2.6
3	5.0± 2.5	4.9± 2.6	4.9± 2.3	5.1± 2.3	1.9± 1.0	5.2± 1.9	5.8± 2.2	4.9± 2.3	7.2± 2.9	5.5± 2.1
4	5.7± 1.7	12.3± 3.6	9.8± 2.1	12.5± 2.7	7.8± 1.6	7.0± 1.5	10.1± 2.8	8.2± 2.2	7.2± 2.1	11.6± 2.4
5	62.2± 8.7	74.2±11.1	47.5± 5.7	34.4± 5.2	27.5± 3.3	31.5± 3.8	48.8± 7.8	51.7± 6.7	82.7±14.9	72.6±10.9

Fitted Temperatures for the Combined 4.0 μm Spectra								
	Longitude							
Region	26	92	160	196	202	278	299	339
1	982±172	927±148	903± 36	917± 32	909± 46	985± 44	987± 64	1009± 69
5	915± 42	933± 61	1023± 51	978± 44	988± 64	981± 49	984± 44	961± 38

Fitted column densities for the combined 4.0 μm spectra given in units of units of 10^{21} mols cm^{-1}								
	Longitude							
Region	26	92	160	196	202	278	299	339
1	6.6±4.4	5.9±3.9	52.1±8.4	27.3±4.6	19.3±4.2	25.0±4.5	18.9±5.3	15.9±4.1
5	28.5±5.7	24.6±6.6	14.3±2.9	16.7±3.0	15.7±4.6	36.2±7.2	40.0±6.8	40.1±6.4

Table 4.24: Table of fitted temperatures and column densities obtained by combining rows sampling the regions described.

Row	Lon	T(K)	$N(H_3^+)$	$E(H_3^+)$	L.S.	$N(H_3^+)^*$	$E(H_3^+)^*$	I^*
	km							
21	137	1546±580	0.04±0.03		2.8	0.01		.026
20	119	826± 87	0.28±0.15	0.35	1.6	0.17	0.21	.040
19	107	706± 50	0.75±0.32	0.41	1.3	0.57	0.31	.049
18	97	647± 38	1.14±0.46	0.41	1.2	0.98	0.35	.049
17	88	727± 62	0.57±0.28	0.38	1.1	0.53	0.35	.043
16	79	867±113	0.22±0.14	0.32	1.0	0.21	0.31	.041
15	71	877±123	0.21±0.14	0.34	1.0	0.21	0.34	.038
14	62	874±105	0.22±0.13	0.36	1.0	0.22	0.36	.036
13	54	931±186	0.14±0.11	0.30	1.0	0.14	0.29	.031
12	45	885±155	0.17±0.13	0.29	1.1	0.16	0.27	.030
11	36	875±144	0.20±0.15	0.34	1.2	0.17	0.29	.034
10	26	793±104	0.36±0.25	0.38	1.3	0.27	0.29	.042
9	14	683± 58	0.97±0.49	0.47	1.6	0.59	0.29	.059
8	356	720± 62	0.76±0.38	0.49	2.8	0.27	0.17	.064

Table 4.25: Results of fitting 3.45 μm spectra with the slit aligned east–west along the equator. The data were obtained on the 5^{th} May 1993 at the CML of 67°. Column densities are given in units of 10^{12} cm^{-2} and total emissions in units of 10^{-1} erg s^{-1} sr^{-1} cm^{-2}.

Row	Lon	T(K)	$N(H_3^+)$	$E(H_3^+)$	L.S.	$N(H_3^+)^*$	$E(H_3^+)^*$	I^*
	km							
19	174	947±185	0.16±0.13	0.37	1.6	0.10	0.23	.040
18	162	866±138	0.26±0.19	0.40	1.3	0.20	0.31	.046
17	152	940±150	0.19±0.13	0.44	1.2	0.16	0.38	.039
16	143	990±194	0.14±0.11	0.40	1.1	0.13	0.37	.037
15	134	900±153	0.22±0.16	0.41	1.0	0.21	0.40	.039
14	126	972±175	0.16±0.12	0.40	1.0	0.16	0.40	.042
13	117	1027±226	0.14±0.11	0.45	1.0	0.14	0.45	.034
12	109	996±214	0.14±0.11	0.40	1.0	0.14	0.39	.032
11	100	983±226	0.15±0.13	0.40	1.1	0.14	0.37	.036
10	91	940±174	0.18±0.14	0.40	1.2	0.16	0.35	.036
9	81	937±140	0.21±0.13	0.46	1.3	0.16	0.35	.038
8	69	1162±262	0.13±0.09	0.67	1.6	0.08	0.41	.040
7	52	982±192	0.21±0.16	0.58	2.8	0.08	0.21	.045

Table 4.26: Results of fitting 3.45 μm spectra with the slit aligned east–west along the equator. The data were obtained on the 3rd May 1993 at the CML of 122°. Column densities are given in units of 10^{12} cm^{-2} and total emissions in units of 10^{-1} erg s^{-1} sr^{-1} cm^{-2}.

Row	Lon	T(K)	$N(H_3^+)$	$E(H_3^+)$	L.S.	$N(H_3^+)^*$	$E(H_3^+)^*$	I^*
	km							
20	159	1920±1507	0.04±0.03		2.8	0.01		.030
19	281	1316± 263	0.10±0.06	0.82	1.6	0.06	0.50	.050
18	269	1132± 164	0.13±0.07	0.64	1.3	0.10	0.49	.050
17	259	852± 102	0.34±0.19	0.51	1.2	0.29	0.44	.054
16	250	830± 92	0.39±0.22	0.51	1.1	0.36	0.48	.054
15	241	975± 142	0.20±0.12	0.53	1.0	0.20	0.52	.049
14	233	1113± 212	0.13±0.09	0.57	1.0	0.13	0.57	.043
13	224	980± 167	0.20±0.14	0.55	1.0	0.20	0.55	.052
12	215	862± 99	0.34±0.18	0.53	1.0	0.33	0.52	.054
11	207	842± 102	0.39±0.23	0.52	1.1	0.36	0.49	.054
10	198	897± 112	0.32±0.26	0.57	1.2	0.28	0.49	.062
9	188	1009± 156	0.22±0.14	0.65	1.3	0.17	0.50	.062
8	176	1048± 178	0.20±0.13	0.70	1.6	0.12	0.43	.057
7	159	913± 172	0.28±0.22	0.57	2.8	0.10	0.21	.058

Table 4.27: Results of fitting 3.45 μm spectra with the slit aligned east–west along the equator. The data were obtained on the 3rd May 1993 at the CML of 229°. Column densities are given in units of 10^{12} cm^{-2} and total emissions in units of 10^{-1} erg s^{-1} sr^{-1} cm^{-2}.

Row	Lon	T(K)	$N(H_3^+)$	$E(H_3^+)$	L.S.	$N(H_3^+)^*$	$E(H_3^+)^*$	I*
	km							
20	320	1143±120	0.13±0.08	0.61	2.0	0.07	0.31	.042
19	306	943±108	0.25±0.13	0.56	1.4	0.17	0.39	.054
18	295	803± 72	0.48±0.23	0.52	1.2	0.39	0.43	.052
17	285	889± 94	0.31±0.15	0.55	1.1	0.28	0.50	.053
16	276	871± 92	0.32±0.16	0.51	1.0	0.31	0.49	.051
15	268	726± 76	0.67±0.40	0.44	1.0	0.66	0.44	.050
14	260	841± 88	0.33±0.17	0.44	1.0	0.33	0.44	.046
13	251	807± 89	0.43±0.25	0.47	1.0	0.43	0.47	.052
12	243	1092±175	0.17±0.10	0.67	1.0	0.16	0.64	.053
11	234	1040±146	0.20±0.11	0.68	1.1	0.18	0.61	.059
10	244	938±122	0.29±0.17	0.64	1.2	0.24	0.52	.058
9	213	912±119	0.3±10.18	0.63	1.4	0.22	0.44	.062
8	199	1095±181	0.22±0.13	0.94	2.0	0.11	0.48	.077
7	863†	977±176	0.18±0.13	0.48	5.0	0.04	0.10	.043

Table 4.28: Results of fitting 3.45 μm spectra with the slit aligned east–west along the equator. The data were obtained on the 4^{th} May 1993 at the CML of 260°. Column densities are given in units of 10^{12} cm^{-2} and total emissions in units of 10^{-1} erg s^{-1} sr^{-1} cm^{-2}.

Row	Lon	T(K)	$N(H_3^+)$	$E(H_3^+)$	L.S.	$N(H_3^+)^*$	$E(H_3^+)^*$	I*
	km							
21	863†	1231±468	0.05±0.05	0.32	5.0	0.01	0.06	.027
20	50	843±102	0.26±0.15	0.36	2.0	0.13	0.18	.047
19	36	811± 77	0.37±0.18	0.43	1.4	0.26	0.30	.051
18	25	785± 86	0.43±0.24	0.42	1.2	0.35	0.34	.051
17	15	705± 67	0.71±0.39	0.39	1.1	0.64	0.35	.048
16	6	722± 69	0.67±0.37	0.44	1.0	0.64	0.42	.051
15	358	688± 55	0.91±0.45	0.46	1.0	0.90	0.46	.060
14	350	741± 74	0.60±0.34	0.45	1.0	0.60	0.45	.052
13	341	650± 58	1.16±0.66	0.41	1.0	1.15	0.41	.049
12	333	725± 72	0.65±0.36	0.43	1.0	0.62	0.41	.050
11	324	893±125	0.28±0.18	0.50	1.1	0.25	0.45	.050
10	314	680± 74	0.98±0.64	0.47	1.2	0.80	0.38	.053
9	303	755± 76	0.70±0.39	0.58	1.4	0.48	0.40	.067
8	289	750± 72	0.97±0.51	0.75	2.0	0.48	0.37	.083
7	863†	823±156	0.21±0.19	0.26	5.0	0.04	0.05	.029

Table 4.29: Results of fitting 3.45 μm spectra with the slit aligned east–west along the equator. The data were obtained on the 4^{th} May 1993 at the CML of 350°. Column densities are given in units of 10^{12} cm^{-2} and total emissions in units of 10^{-1} erg s^{-1} sr^{-1} cm^{-2}.

Chapter 5

Summary and Discussion

The results obtained from imaging and spectroscopy are broadly in agreement with each other. The locations of auroral H_3^+ maxima and minima determined by either analyses of the ProtoCam images or by spectroscopic mapping of the total emission are roughly the same. Where the information provided by the two methods differ are in the detailed structure of the aurorae, for which the spectroscopy cannot resolve, and the low latitude distribution of the H_3^+ emission, the small variation of which the camera is not sensitive enough to pick up on.

In this chapter we will follow the pattern used in the previous two and discuss, separately, the results obtained for the northern and southern aurorae, and emission on the body of the planet.

5.1 The Jovian Northern Aurora

We find average temperature and column density to be about 800 K and 9×10^{12} cm^{-2} respectively. Both the images and the spectra tell us that a large amount of emission occurs preferentially over a narrow range of longitudes, around $\lambda_{III} = 150°$. Images of the aurora show that this is taking place at high magnetic shells, the southern boundary of which may be as high as magnetic shell = 30 footprint (Connerney 1991, 1993). Spectroscopic mapping of the H_3^+ emission appears to confirm this, although there is a large degree of

uncertainty about the location of the emission at this high latitude.

We also see, in the images, two distinct emission structures, suggesting two dominant mechanisms depositing energy in the northern auroral region. The large patch of emission seen in the images at around $\lambda_{III} = 150°$, does not seem to have a particular structure, in contrast to the rest of the aurora where we see discrete bright spots of emission located along a possible oval. The unstructured emission is consistent with energy deposition through particle precipitation via loss cone and angular diffusion, while the discrete bright spots are typical of Joule heating and particle precipitation along field-aligned currents (Gérard *et al* 1993).

The local magnetic field plays a large part in the control of particle precipitation flux, which means that the emission structure should give us information about the geometry of the field. It is, therefore, curious to find the H_3^+ emission to be relatively bright in the region of highest surface magnetic field strength, according to the O_6 model (Connerney 1991, 1993).

Particle precipitation modelling by Prangé and Elkhamsi (1991) indicates that maximum precipitation should take place between $\lambda_{III} = 220°$–$250°$ for electrons and between $\lambda_{III} = 270°$ and $300°$ for ions. These do not correlate with the results we have obtained here. We are at a loss to explain the presence of bright emission at $\lambda_{III} = 150°$.

The emission minimum around $\lambda_{III} = 180°$, also does not correlate with the surface field strength. If field-aligned currents are assumed to be absent and particle precipitation is the only mechanism in effect in this region, then the emission brightness minimum strongly suggests that this is the area of strongest surface field strength. Longitude 180° is just past the O_6 (Connerney 1991, 1993) field strength maximum and therefore, according to the particle precipitation model of Prangé and Elkhamsi (1991), should see the H_3^+ emission beginning to brighten up as the "windshield wiper" effect begins to make its presence felt. It is interesting to note that both of these anomalous features are out of phase with the magnetic field geometry by roughly 30° and that moving the location of the field by this amount we can achieve some measure of agreement between the model and data.

We would like to point out that our results here is in agreement with the latest UV images obtained by Gérard *et al* (1994) using the Hubble Space Telescope, in which they also observed a large area of diffuse emission at around $\lambda_{III} = 150°$ and bright, discrete emission arc between $\lambda_{III} = 180°$ and 240° located along an oval consistent with the magnetic shell = 30 R_J footprint. Their images also show a local minimum near to but not quite at 180° longitude.

5.2 The Southern Auroral Region

Average fitted temperature and column density are roughly in line with those found in the north (800 K and 9×10^{12} cm^{-2} respectively). Bright auroral emission is found to occur over a large longitude range. The spectroscopic mapping of the total emission suggests that the emission is located around the Io torus footprint or the auroral boundary. This in contrast with images of the southern aurora, which indicate that the emission comes from an area, south of the magnetic shell = 30 footprint, beginning at $\lambda_{III} = 50°$ and extending westward to $\lambda_{III} = 300°$; at which point the viewing geometry of the aurora makes it hard to determine if this continues further or not. However, from spectroscopy we can say that this emission area does extend further to about $\lambda_{III} = 250°$. The apparent disagreement between the spectroscopic map and the images may be due to uncertainty in estimating the latitudinal positions of the spectra, rather than any real physical differences.

Between $\lambda_{III} = 150°$ and 200°, both the imaging and spectroscopy tell us that the southern aurora is at a minimum in brightness. The possible auroral oval seen in the corrected images suggests that field-aligned currents does have an effect in this region. However, its dimness compare to discrete emissions in the north implies that the effect is nowhere near as great.

There is a possibility that the emission is located in an oval that does not appear to correlate with the footprints of either of the magnetic shells plotted on the images. This could be due to the oval mapping some other magnetic ovals at distances larger than 30 R_J from the planet. It could also be due uncertainties in magnetic field model at the surface of the planet. The poor viewing geometry of the southern aurora at all longitudes, as

compare with the northern aurora around CML 180°, means that it is difficult to confirm the geometry as such.

5.3 Total Auroral Emission

The E(cml) parameter introduced in chapter 4 has enabled us to compute the total emission for both aurorae. We find that total auroral power output is about 5×10^{12} W sr^{-1} for both the north and the south. This is comparable to the total power output estimated for the U.V. aurorae (Strobel and Atreya 1983). This has shown that the H_3^+ ion is an important component in the energy balance of the jovian atmosphere.

5.4 H_3^+ Emission on the Body of the Planet

The H_3^+ emission outside of the aurorae is shown to vary in both longitude and latitude. Although the intensity is much less than that in the aurorae (about 10% of auroral emission) we were able to determined that the H_3^+ emission minimum best correlate with the magnetic dip equator. The region of emission minimum is largest in an area located around $\lambda_{III} = 100°$ and 10° north of the rotational equator. The O_6 model predicts the magnetic field to be highly distorted at this location compare to elsewhere outside of the auroral zones. This is also the region where the brightness of non-auroral H Lyman-α emission is enhanced (H Lyman-α bulge). These suggest that there is a relationship between the two emission sources and the geometry of the magnetic field.

Until now, it has been assumed that solar EUV radiation is the principle mechanism for the production of H_3^+ away from the auroral regions. The radiation is unaffected by the magnetic field and should results in a flat, pole to pole emission profile. That this is not the case clearly suggests solar EUV alone is insufficient to account for H_3^+ emission on the body of the planet. If we assume that the H_3^+ intensity in the region of emission minimum is due solely to the incident solar EUV flux, then outside of this emission minimum, contribution to the non-auroral H_3^+ emission is at least 25% of this value. We tentatively, examine the possibility of low latitude particle precipitation as a possible energy source to explain the

observed H_3^+ emission distribution.

The altitude at which an impacting particle deposit its energy is very much dependent on the incident angle (the angle between the path of the incoming particles and the plane of the atmosphere) on arrival at the top of the atmosphere. Prangé *et al* (1995) modelled the anisotropic effect of precipitating particles in order to explain the auroral Lyman-α and H_2 bands. Although primarily concerned with auroral precipitation, Prangé *et al* did compute, as a check of their model, the penetration depth of mono-energetic (10 keV) primary electrons for varying degrees of inclination from the vertical. They found that the altitude of peak excitation rate rises by about 200 km for inclination angles varying from 1° to 88°. For field-aligned electrons, the dip angles of magnetic field lines may have a major influence on the incident angle of an impacting electron. We propose that, at the magnetic dip equator, particles hitting the atmosphere will have small or grazing incident angles. Energy deposition may, therefore, occur mainly high up in the ionosphere, above the H_3^+ peak. Production of H_3^+ will be largely unaffected by the precipitating particles, leaving solar EUV as the main H_3^+ formation mechanism. At larger dip angles, particles will incident at larger angles and energy deposition may take place at correspondingly lower altitudes. The effect on the production of H_3^+ will thus increase with increasing magnetic dip angles. This is a simplistic view of the mechanism and neglects other factors such as the energy spectrum of the precipitating flux, pitch angles of the particles and the population of the incident particles. All will be important concerning the altitude of energy deposition. However, large distortion of the magnetic field around $\lambda_{III} = 100°$, where the magnetic dip equator is at its northern most latitude range, may serve to encourage the deposition of energy high up in the atmosphere, enhancing the H Lyman-α emission but leaving the H_3^+ relatively unaffected.

The introduction of the E(cml) parameter (see chapter 4) was an attempt at determining the longitudinal structure of the auroral H_3^+ emission without being concerned with latitudinal variation.

Plotting the calculated total emission values as a function of longitudes we find that, in the north, the H_3^+ emission peaks around 150° longitude. This drops to a minimum

around 0° longitude. The E(cml) plot for the southern aurora shows that H_3^+ emission has a broad maximum between 250° and 50° longitude. The E(cml) plot drops to a minimum between 150° and 200° longitude. Once again the results is in agreement with analyses using images as well as the mapping of the total emission parameter.

This E(cml) parameter proved to be very useful to the interpretation of results obtained during the SL9 campaign in July 1994 (Miller *et al* 1995). It showed that, during the impact week, H_3^+ emission was enhanced in the north only at longitudes where H_3^+ emission was already exhibiting a maximum prior to the impact. In the south, H_3^+ emission was depressed in the auroral region only at longitudes either side of the emission minimum. At 150° the H_3^+ emission remained at roughly the same, pre-impact intensity.

5.5 Summary

This work has demonstrated that combining H_3^+ spectroscopy with imaging provides parameters that give useful input into models of the jovian ionosphere, and test models of the magnetic field. The emission is highly longitude as well as latitude dependent. This occurs not only in the aurora, where energy deposition is strongly modulated by the magnetic field, but also on the body of the planet where we see evidence of magnetic field dependent H_3^+ emission. The northern emission maximum and minimum occur in places where we cannot account for by the geometry of the magnetic field. Non-auroral H_3^+ is shown to correlate well with magnetic field dip angles for which we tentatively propose a simple mechanism to account for it. However, there may be many other factors which we have not considered. More work is needed to explain this correlation of H_3^+ emission with magnetic field dip angles, and anti-correlation with the non-auroral H Lyman-α emission.

5.6 Future Work

We have shown that H_3^+ can be usefully employed to monitor the physical conditions in the jovian ionosphere. The possibility that the emission is closely correlated with the magnetic field presents us with an intriguing opportunity to constrain magnetic field models and to

also discriminate between energy mechanisms. That solar EUV is insufficient to explain the observed flux of H_3^+ emission is proof that more is going on than was previously thought.

At the present time, we can not locate precisely the latitudinal positions of either the northern or southern aurora, due to the low spatial resolution of our data. We hope that with the new CGS4 detector array, with its greater spatial resolution, we may be able to answer this question.

The ProtoCam images used in this work required them to be fitted to a disk of Jupiter. This, to some extent, is subjective and is dependent on the person performing the task. The new NSFCAM developed for the NASA IRTF can obtain the whole planet in one image, thereby eliminating the uncertainty in locating the planetary limb. Latest images showed that this camera is capable of resolving the aurorae in favourable observing conditions. We hope to obtain more of these kind of images so that the auroral structures can be determined more accurately and correlate them with those in the U.V.

We have shown that the imaging technique can be used to distinguish between diffuse and discrete auroral emissions, giving information on the different magnetospheric processes. This kind of information is particularly important when modelling the magnetosphere. We wish to expand on this work in order to give greater input into magnetospheric models. Our analysis also suggests that H_3^+ emission is occurring to high altitudes which seemed to be confirmed by the latest NSFCAM images. Unfortunately our line of sight correction method appears to be a bit crude where the high altitude emission is concerned and may have over compensated for the limb brightening. We would like to improve on the correction model to take this into account.

Bibliography

Abouelainine, A., Mangeney, A., Drossart, P., *Numerical Simulation of the Dissipation of a Thermal Disturbance in a Jovian Atmosphere*, Proc. of the European SL–9/Jupiter Workshop, 269-274, 1995

Achilleos, N., Miller, S., Dinelli, B. M., Lam, H. A., Tennyson, J., Jagod, M. F., Geballe, T. R., Trafton, L. T., Joseph, R. D., Ballester, G. E., *Post-SL9 Impact Brightness Imbalance in the jovian Aurorae*, European SL-9/Jupiter Workshop, Conference Proceedings, **52**, 375–380, 1995

Acuña, M. H., Behannon, K. W., Connerney, J. E. P., *Jupiter's Magnetic Field and Magnetosphere*, In Physics of the Jovian Magnetosphere, Ed Dessler, A. J., Cam. Plan. Sci. Series, Cambridge University Press, Cambridge, 1–49, 1983

Acuña, M. H., and Ness, N. F., *The Main Magnetic Field of Jupiter*, J. Geophys. Res., **81**, 2917–2922, 1976

Atreya, S. K., *Atmospheres and Ionospheres of the Outer Planets and Their Satellites*, Springer-Verlag, Berlin, 1986

Atreya, S. K., Kerr, R. B., Upson, W. L., II, Festou, M. C., Donahue, T. M., Barker, E. S., Cochran, W. D., Bertaux, J. L., *Copernicus Measurement of the Jovian Lyman-alpha Emission and its Aeronomical Significance*, Astrophys. J., **262**, 377–387, 1982

Atreya, S. K., Barker, E. S., Yung, Y. L., Donahue, T. M., *Search for Jovian Auroral Hot Spots*, Astrophys. J. Let., **218**, L83–L87, 1977

Atreya, S. K., Donahue, T. M. and Festou, M. C., *Jupiter: Structure and Composition of the Upper Atmosphere*, Astrophys. J., **247**, L43–L47, 1981

Atreya, S. K., Donahue, T. M., *Model Ionosphere of Jupiter*, In Jupiter, Ed. Gehrels, T., University Arizona Press, 304–317, 1976

Atreya, S. K., Donahue, T. M., McElroy, M. B., *Jupiter's Ionosphere: Prospects for Pioneer 10*, Science, **184**, 154–156, 1974

Avni, Y., *Energy Spectra of X-ray Cluster of Galaxies*, Astrophys. J., **210**, 624–646, 1976

Bailey, J., *CGS4 Data Reduction Using Figaro*, UKIRT Observer Note 9.1, S.E.R.C Joint Astronomy Center, 1991

Ballester, G. E., Miller, S., Tennyson, T., Trafton, L. M., Geballe, T. R., *Latitudinal Temperature Variations of Jovian H_3^+*, Icarus, **107**, 189–194, 1994

Baron, R. L., Owen, T., Satoh, T., Connerney, J. E. P., Harrington, J., *The Jovian H_3^+ Aurora: Time Variability and Solar Wind Parameters.*, Bull. Am. Astron. Soc, **25**, 1053, 1993

Baron, R. L., Joseph, R. D., Owen, T., Tennyson, J., Miller, S., Ballester, G. E., *Imaging Jupiter's Aurorae from H_3^+ Emissions in the 3–4μmBand*, Nature, **353**, 539–542, 1991

Belcher, J. W., *The Low-Energy Plasma in the Jovian Magnetosphere*, In Physics of the Jovian Magnetosphere, Ed. Dessler, A. J., Cam. Plan. Sci. Series, Cambridge University Press, Cambridge, 68–105, 1983

Belton, M. J. S., West, R. A., Rahe, J., Ed., *Time Variable Phenomena in the Jovian System*, NASA, Washington D.C., 183–195, 1989

Bevington, P. R., *Data Reduction and Error Analysis for the Physical Sciences*, McGraw-Hill, 1969

Bigg, E. K., *Influence of the Satellite Io on Jupiter's Decametric Emission*, Nature, **203**, 1008–1010, 1964

Black, J. H., van Dishoeck, E. F., Willner, S. P., Woods, R. C., *Interstellar Absorption Lines Towards NGC 2264 and AFGL 2591 - Abundances of H_2. H_3^+ and CO*, Astrophys. J., **358**, 459–467, 1990

Broadfoot, A. L., Belton, M. J., Takacs, P. Z., Sandel, B. R., Shemansky, D. E., Holberg, J. B., Ajello, J. M., Atreya, S. K., Donahue, T. M., Moos, H. W., *Extreme Ultraviolet Observations from Voyager 1 Encounter with Jupiter*, Science, **204**, 979–982, 1979

Brown, R. A., *Optical Line Emission from Io*, In Exploration of the Planetary System, Ed. Woszczyk, A., Iwaniszewska, C., Reidel, D. Publishing Co., 527–531, 1974

Bryant, D. A., *Space Plasma Physics, I: Basic Processes in the Solar System*, In Plasma Physics: An Introductory Course, Ed. Dendy, R., Cam. Plan. Sci. Series, Cambridge University Press, Cambridge, 209–232, 1993

Burke, B. F., and Franklin, K. L., *Observations of a Variable Radio Source Associated with the Planet Jupiter*, J. Geophys. Res., **60**, 13–217, 1955

Caldwell, J., Turgeon, B., Hua, X.-M., *Hubble Space Telescope Imaging of the North Polar Aurora on Jupiter*, Science, **257**, 1512–1515, 1992

Caldwell, J., Tokunaga, A. J., Gillett, F. C., *Possible Infrared Aurorae on Jupiter*, Icarus, **41**, 667–675, 1980

Carr, T. D. and Desch, M. D., *Recent Decametric and Hectometric Observations of Jupiter*, In Jupiter, Ed. Gehrels, T, University Arizona Press, Tucson, 693–795, 1976

Carr, T. D., Desch, M. D., and Alexander, J. K., *Phenomenology of Magnetospheric Radio Emissions*, In Physics of the Jovian Magnetosphere, Ed. Dessler, A. J., Cam. Plan. Sci. Series, Cambridge University Press, Cambridge, 226–284, 1983

Cash, W., *Generation of Confidence Intervals for Model Parameters in X-ray Astronomy*, Astron. & Astrophys., **52**, 307–308, 1976

Chamberlain, J. W. and Hunten, D. M., *Theory of Planetary Atmospheres*, Academic Press, San Diego, 1987

Christoffersen, R. E., Hagstrom, S., and Prosser, F., J. Chem. Phys., **40**, 236, 1964

Clarke, J. T., Gladstone, G. R., Jaffel, L. B., *Jupiter's Dayglow H Ly α Emission Line Profile*, Geophys. Res. Let., **18 no. 11**, 1935–1938, 1991

Clarke, J. T., Caldwell, J., Skinner, T. E., Yelle, R. V., *The Aurora and Airglow of Jupiter*, In Time-Variable Phenomenon in the Jovian System, Ed. Belton, M. J. S., West, R. A., Rahe, J., NASA, Washington D.C., 211–228, 1989

Clarke, J. T., Feldman, P. D., Moos, H. W., *IUE monitoring of the Spatial Distribution of the H Ly-alpha Emission from Jupiter.*, Astrophys. J. Let., **245**, L127–129, 1981

Cline, D. and Lesser, P. M. S., *Error Estimation in Non-Linear Least Squares Analysis of Data*, Nuclear Instrument and Methods, **82**, 291–293, 1970

De Bergh, C., Lecacheux, J., Combes, M., Maillard, J. P., *New Infrared Spectra of the Jovian Planets from 12000 to 4000 per cm by Fourier Transform Spectroscopy. III - First-overtone Pressure-induced H2 absorption in the Atmosphere of Jupiter and Saturn*, Astron. Astrophys., **35 no. 3**, 333–337, 1974

Connerney, J. E. P., Baron, R., Satoh, T., Owen, T., *Images of Excited H_3^+ at the Foot of the Io Flux Tube in Jupiter's Atmosphere*, Science, **262**, 1035–1038, 1993

Connerney, J. E. P., *Magnetic Fields of the Outer Planets*, J. Geophys. Res., **98 no. E10**, 18659–18679, 1993

Connerney, J. E. P., *Doing More with Jupiter's Magnetic Field*, In Planetary Radio Emissions III, Ed Rucker, H. O., Bauer, S. J., Kaiser, M. L., Proc. of 3rd Int. Workshop Held at Graz (Austria), Verlag der Österreichischen Akademie der Wissenschaften, Vienna, 13–33, 1991

Connerney, J. E. P., Acuña, M. H., Ness, N. F., *Voyager 1 Assessment of Jupiter's Planetary Magnetic Field*, J. Geophys. Res., **86**, 3623–3627, 1982

Daly, P. N., and Beard, S. M., *CGS4DR—v1.6-0 User's Guide*, Starlink User Note 27.1, S.E.R.C. Rutherford Appleton Laboratory, 1992

Desch, M. D., Carr, T. D. Levy, J., *Observations of Jupiter at 26.3 MHz using a Large Array*, Icarus, **25**, 12–17, 1975

Dessler, A. J., Ed., *Physics of the Jovian Magnetosphere*, Cam. Plan. Sci. Series, Cambridge University Press, Cambridge, 1983

Dessler, A. J., and Hill, T. W., *Jovian Longitudinal Control of Io Related Radio Emissions*, Astrophys. J., **227**, 664–675, 1979

Dessler, A. J. and Vasyliunas, V. M., *The Magnetic Anomaly Model of the Jovian Magnetosphere: Predictions for Voyager*, Geophys. Res. Let., **6**, 37–40, 1979

Dessler, A. J and Chamberlain, J. W., *Jovian Longitudinal Asymmetry in Io-related and Europa-related Auroral Hot Spots*, Astrophys. J., **239**, 974–981, 1979

Dinelli, B. M., Achilleos, N., Lam, H. A., Tennyson, J., Miller, S., Jagod, M. F., Oka, T., Geballe, T. R., *Infrared Spectroscopic Studies of the Impact of Fragment C of SL-9*, European SL-9/Jupiter Workshop, Conference Proceedings, **52**, 245–249, 1995

Dinelli, B. M., Miller, S., Tennyson, J., *A Spectroscopically Determined Potential Energy Surface for H_3^+*, J. Mol. Spectrosc., **163**, 71–79, 1994

Dols, V., Gérard, J. C., Paresce, F., Prangé, R., Vidal-Madjar, A., *Ultraviolet Imaging of the Jovian Aurora with the Hubble Space Telescope*, Geophys. Res. Let., **19 no. 18**, 1803–1806, 1992

Drossart, P., Bézard, B., Atreya, S. K., Bishop, J., Waite Jr., J. H., Boice, D., *Thermal Profiles in the Auroral Regions of Jupiter*, J. Geophys. Res., **98 no. E10**, 18803–18811, 1993

Drossart, p, Prangé, R., Maillard, J. C., *Morphology of Infrared H_3^+ Emissions in the Auroral Regions of Jupiter*, Icarus, **97**, 10–25, 1992

Drossart, P., Maillard, J. P., J.Caldwell, J., Kim, S. J., Watson, J. K. G., Majewski, W. A., Tennyson, J., Miller, S., Atreya, S. K., Clarke, J. T., Waite Jr., J. H. and Wagener, R., *Detection of H_3^+ on Jupiter*, Nature, **340**, 539–541, 1989

Drossart, P., Bézard, B., Atreya, S., Lacy, J., Serabyn, E., Tokunaga, A., Encrenaz, T., *Enhanced Acetylene Emission Near the North Pole of Jupiter*, Icarus, **66**, 610–618, 1986

Drossart, P., Encrenaz, T., Combes, M., Kunde, V., Hanel, R., *An Estimate of the PH3, CH3D, and GeH4 Abundances on Jupiter from the Voyager IRIS data at 4.5 Microns*, Icarus, **49**, 416–426, 1982

Flower, D., *Molecular Collisions in the Interstellar Medium*, Cam. Astrophys. Series, Cambridge University Press, **17**, 1990

Geballe, T. R., and Oka, T., *An Infrared Spectroscopic Search for the Molecular Ion H_3^+*, Astrophys. J., **342**, 855–859, 1989

Gérard, J. C., Dols, V., Prangé, R., Paresce, F., *The Morphology of the North Jovian Ultraviolet Aurora Observed with the Hubble Space Telescope*, Planet. Space Sci., **42 no. 11**, 905–917, 1994

Gérard, J. C., Dols, V., Paresce, F., Prangé, R., *Morphology and Time Variation of the Jovian Far UV Aurora: Hubble Space Telescope Observations*, J. Geophys. Res., **98 no. E10**, 18793–13801, 1993

Goldreich, P. and Lynden-Bell, D., *Io, a Jovian Unipolar Inductor*, Astrophys. J., **156**, 59–78, 1969

Goldstein, M. L. and Eviatar, A., *An Emission Mechanism for the Io-Independent Jovian Decameter Radiation*, Astrophys. J., **230**, 261–273, 1979

Hamilton, D. C., Gloeckler, G., Krimigis, S. M., Bostrom, C. O., Armstrong, T. P., *et al*, *Detection of Energetic Hydrogen Molecules in Jupiter's Magnetosphere by Voyager 2: Evidence for an Ionospheric Plasma Source*, Geophys. Res. Let., **7**, 813–816, 1980

Herbert, F., Sandel, B. R., and Broadfoot, A. L., *Observations of the Jovian UV Aurora by Voyager*, J. Geophys. Res., **92**, 3141–3154, 1987

Herzberg, G., Trans. Roy. Soc. Can., **5**, 3, 1967

Hirschfelder, J. O., J. Chem. Phys., **6**, 1938

Hunten, D. M., *Atmospheres and Ionospheres*, In Jupiter, Ed. Gehrels, T., University Arizona Press, Tucson, 22–31, 1976

Jaffel, L. B., Clarke, J. T., Prangé, R., Gladstone, G. R., Vidal-Madjar, A., *The Lyman Alpha Bulge of Jupiter: Effects of Non-Thermal Velocity Field*, Geophys. Res. Let., **20 no. 8**, 747–750, 1993

Kao, L., Oka, T., Miller, S., Tennyson, T., *A Table of Astronomically Important Ro-Vibrational Transitions for the H_3^+ Molecular Ion*, Astrophys. J. Suppl., **77**, 317–329, 1991

Kim, S. J., Drossart, P., Caldwell, J., Maillard, J. P., Herbst, T., Shure, M., *Images of Aurorae on Jupiter from H_3^+ Emission at 4 Microns*, Nature, **353**, 536–539, 1991

Kim, Y. H., Kim, S. J., Stuewe, J. A., Caldwell, J., Herbst,, T. M., *Jovian Auroral Ovals Inferred from Infrared H_3^+ Images*, Icarus, **112**, 326–336, 1994

Kim, Y. H., Fox, J. L. and Porter, H. S., *Densities and Vibrational Distribution of H_3^+ in the Jovian Auroral Ionosphere*, J. Geophys. Res., **97 no. E4**, 6093–6101, 1992

Kim, Y. H. and J. L. Fox, *The Jovian Ionospheric E Region*, Geophys. Res. Let., **18 no. 2**, 123–126, 1991

Kim, S. J., Caldwell, J., Rivolo, A. R., Wagener, R., Orton, G. S., *Infrared Polar Brightening on Jupiter. III - Spectrometry from the Voyager 1 IRIS Experiment*, Icarus, **64**, 233–248, 1985

Kupo, I., Mekler, Y., and Eviatar, A., *Detection of Ionised Sulphur in the Jovian Magnetosphere*, Astrophys. J. Let., **205**, L51–l53, 1976

Lampton, M., Margon, B., Bower, S., *Parameter Estimation in X-ray Astronomy*, Astrophys. J., **208**, 177–190, 1976

Leblanc, Y., *On the Arc Structure of the DAM Jupiter Emission*, J. Geophys. Res., **86**, 8546–8568, 1981

Lequeux, J., and Roueff, E., *Interstellar Molecules*, Phys. Rep.: Rev. Sec. of Phys. Let., **200 no. 5**, 241–299 , 1991

Lellouch, E., Encrenaz, T., Drossart, P., Combes, F., *The Observability of HCN on Jupiter in the Millimeter Range*, Astron. & Astrophys., **135 no. 2**, 365–370, 1984

Lester, D. F., L. M. Trafton, T. F. Ramseyer and N. I. Gaffney, *Discovery of a Second Narrow Absorption Feature in the Near-Infrared Spectrum of Io*, Icarus, **98**, 134–140, 1992

Maillard, J. P., Drossart, P., Watson, J. K. G., Kim, S. J., and Caldwell, J., H_3^+ *Fundamental Band in Jupiter's Auroral Zones at High Resolution from 2400 to 2900 Inverse Centimeters*, Astrophys. J., **363**, L37–L41, 1990

Marten, A., De Bergh, C., Owen, T., Gautier, D., Maillard, J. P., Drossart, P., Lutz, B. I., Orton, G. S., *Four Micron High-Resolution Spectra of Jupiter in the North Equatorial Belt:* H_3^+ *Emissions and the* $^{12}C/^{13}C$ *Ratio*, Planet. Space Sci., **42 no. 5**, 391–399, 1994

McConnell, J. C., T. Majeed, H_3^+ *in the Jovian Ionosphere*, J. Geophys. Res., **92**, 8570–8578, 1987

McConnell, J. C., Sandel, B. R., Broadfoot, A. L., *Airglow from Jupiter's Nightside and Crescent - Ultraviolet Spectrometer Observations from Voyager 2*, Icarus, **43**, 128–142, 1980

McGrath, M. A., *An Unusual Change in the Jovian Ly α Bulge*, Geophys. Res. Let., **18 no. 11**, 1931–1934, 1991

Meyer, W., Botschwina, P., Burton, P., J. Chem. Phys., **84**, 891, 1989

Miller, S., Achilleos, N., Dinelli, B. M., Lam, H. A., Tennyson, J., Jagod, M.-F., Geballe, T. R., Trafton, L. M., Joseph, R. D., Ballester, G. E., Baines, K., Brooke, T. Y., Orton, G., *The Effect of the Impact of Comet Shoemaker Levy-9 on Jupiter's Aurorae*, Geophys. Res. Let., **22 no. 12**, 1629–1632, 1995

Miller, S., Lam, H. A., Tennyson, J., *What Astronomy has Learned from Observations of* H_3^+, Can. J. Phys., **72 no. 11&12**, 760–771, 1994

Miller, S., Lam, H. A., Tennyson, J., Ridgeway, S. and Joseph, R. D., *Spectroscopy of* H_3^+ *in the Jovian Atmosphere*, Bull. Am. Astron. Soc., **23**, 1136, 1991

Miller, S., Tennyson, J., Joseph, R. D., *Infrared Emissions of* H_3^+ *in the Atmosphere of Jupiter in the 2.1 and 4.0 micron region*, Astrophys. J., **360**, L55–L58, 1990

Miller, S., Tennyson, J., *Hot Band Transition Frequencies and Line Strengths in* H_3^+*: First Principles Calculations*, J. Mol. Spectrosc., **136**, 223–240, 1989

Miller, S., Tennyson, J., *Calculated Rotational and Rovibrational Transitions in the Spectrum of* H_3^+, Astrophys. J., **335**, 486–490, 1988

Nishida, A. and Y. Wattanabe, *Joule Heating of the Jovian Ionosphere by Corotation Enforcement Currents*, J. Geophys. Res., **86**, 9445–9952, 1981

Oka, T. and Geballe, T. R., *Observations of the 4 Micron Fundamental Band of* H_3^+ *in Jupiter*, Astrophys. J. Let., **351**, L53–L56, 1990

Oka, T., *A search for Interstellar H_3^+*, R. Soc. Phil. Trans. Series A, **303 no. 1480**, 543–549, 1981

Piddington, J. H. and Drake, J. F., *Electrodynamic Effects of Jupiter's Satellite Io*, Nature, **217**, 935–937, 1968

Prangé, R., Rego, D., Gérard, J. C., *Auroral Lyman α and H_2 Bands from the Giant Planets 2: Effect of the Anisotropy of the Precipitating Particles on the Interpretation of the "Color Ratio"*, J. Geophys. Res., **100 no. E4**, 7513–7521, 1995

Prangé, R., *The UV and IR Jovian Aurorae*, Adv. Space Res., **12 no. 8**, (8)379–(8)389, 1992

Prangé, R., *Jovian UV Aurorae, IR Aurora, and Particle Precipitations: A Common Origin?*, Astron. & Astrophys. Let., **251**, L15–L18, 1991

Prangé, R., Elkhamsi, M., *Modeling the Precipitation Flux in the Jovian Auroral Zones, 1. The Model and Its Application to the UV Auroral Emissions*, J. Geophys. Res., **96 no. A12**, 21371–21389, 1991

Press, W. H., Flannery, B. P., Teukolsky, S. A. and Vetterling, W. T., *Numerical Recipes: The Art of Scientific Computing*, Cambridge University Press, 1986

Ridgeway, S. T., Larson, H. P., and Fink, U., *The Infrared Spectrum of Jupiter*, In Jupiter, Ed. Gehrels, T., University of Arizona Press, Tucson, 384–417, 1976

Roble, R. G., et al., *Joule Heating in the Mesosphere and Thermosphere During the July 13, 1982 Solar Proton Event*, J. Geophys., Res., **92**, 6083–6090, 1987

Sandel, B. R., Broadfoot, A. L., Strobel, D. F., *Discovery of a Longitudinal Asymmetry in the H Lyman-alpha brightness of Jupiter*, Geophys. Res. Let., **7**, 5–8, 1980

Sandel, B. R., Shemansky, D. E., Broadfoot, A. L., Bertaux, J. L., Blamont, J. E., Belton, M. J. S., Ajello, J. M., Holberg, J. B., Atreya, S. K., Donahue, T. M., *Extreme Ultraviolet Observations from Voyager Encounter with Jupiter*, Science, **206**, 962–966, 1979

Satoh, T., Baron, R. L. and Connerney, J. E. P., *Detailed Structure of H_3^+ Aurora on Jupiter*, Bull. Am. Astron. Soc., **25**, 1053, 1993

Shardt, A. W. and Goertz, C. K., *High-Energy Particles*, In Physics of the Jovian Magnetosphere, Ed. Dessler, A. J., Cam. Plan. Sci. Series, Cambridge University Press, Cambridge, 157–196, 1983

Shemansky, D. E., *Particle Excitation, Airglow and H2 Vibrational Disequilibrium in the Atmosphere of Jupiter*, Final Technical Report University of Southern California, Los Angeles, 1984

Schulz, R., Encrenaz, T., Stüwe, J. A., Wiedermann, G., *Monitoring of Near-IR Emission Features at the NTT and Detection of the Northern Counterparts*, European SL-9/Jupiter Workshop, Conference Proceedings, **52**, 363–368, 1995

Smith, E. J, Davis, L. Jr., and Jones, D. E., *Jupiter's Magnetic Field and Magnetosphere*, In Jupiter, Ed. Gehrels, T., University Arizona Press, Tucson, 788–829, 1976

Smoluchowski, R., *Origin and Structure of Jupiter and its Satellites*, In Jupiter, Ed. Gehrels, T., University Arizona Press, Tucson, 3–21, 1976

Strobel, D. F., *Energetics, Luminosity and Spectroscopy of Io's Torus*, In Time Variable Phenomena in the Jovian System, Ed. Belton, M. J. S., West, R. A., Rahe, J., NASA, Washington D.C., 183–195, 1989

Strobel, D. F. and Atreya, S. K., *Ionosphere*, In Physics of the Jovian Magnetosphere, Ed. Dessler, A. J., Cam. Plan. Sci. Series, Cambridge University Press, Cambridge, 51–67, 1983

Tennyson, J., *Spectroscopy of H_3^+: Planets, Chaos and the Universe*, Rep. Prog. Phys., **57**, 421–476, 1995

Thomson, J. J., *Further Experiments on Positive Rays*, Phil. Mag., **24**, 209–253, 1912

Trafton, L. M., Gérard, J. C., Munhoven, G., Waite Jr., J. H., *High-Resolution Spectra of Jupiter's Northern Auroral Ultraviolet Emission with the Hubble Space Telescope*, Astro. Phys. J, **421**, 816–827, 1994

Trafton, L. M., Lester, D. F., and Thompson, K. L., *Unidentified Emission Lines in Jupiter's Northern and Southern 2-micron Aurorae*, Astrophys. J., **343**, L37, 1989

Waite Jr., J. H., Cravens, T. E., Kozyra, J. U., Nagy, A. F., Atreya, S. K. and Chen, R. H., *Electron Precipitation and Related Aeronomy of the Jovian Thermosphere and Ionosphere*, J. Geophys, Res., **88**, 6143–6163, 1983

Wright, G. S., Mountain, C. M., Bridger, A., Daly, P. N., Griffin, J. L., Ramsay, S. K., *The CGS4 Experience - Two Years Later*, Edinburgh Astron. Preprint, 1993

Zhan, J. and Dessler, A. J., *A Magnetospheric Model of the Jovian North and South Polar Infrared Hot Spot (paper presented at Symposium on Magnetosphere of the Outer Planets)*, Am. Astron. Soc., Annapolis, Md., 1990

Appendix A

In-House Program Suite

A.1 Image Arithmetic

NAME

`add/subtract/multiply/divide`

SYNTAX

`program [file1] [file2] [file3]`

DESCRIPTION

Adds/Subtracts/Multiply/Divide two images to make a new image. If **[c]** is given in place of **[file2]** the program prompts the user to input a number constant. This is added to/subtracted from/multiplied by/divided into the data values contained in the image file given by the file-name **file1**. The new image is written out to the file name given by **file3**. If this name is not given then the program prompts for the name.

A.2 Viewing Images and Spectra

NAME

`view_image`

SYNTAX

`view_image [image-name]`

DESCRIPTION

Plots colour shaded picture of an image for inspection and hardcopy purposes. A graphics windows is opened in which contour plots of the image is shown. The user is prompted for a number of options to do with how the image should be displayed. Pressing the return key without typing any other key automatically selects the default value. This feature does not apply when the program ask for shading limits. The user has to input the extreme shading values in the window that the program was started in. Once the image has been plotted the user has the options of redrawing the image with different shading limits by pressing the key '**r**'(for redraw) or end the program by pressing the key '**q**'(for quit) in the active graphics window.

NAME

`view_spectrum`

SYNTAX

`view_spectrum [file-name]`

DESCRIPTION

A graphics window is opened in which histograms of the data values is displayed. The user has the options of viewing the data either along the rows or columns of the image array. The later is intended to help in the tracing of a spectrum across an image. The program asks for rows or columns to be selected using the mouse and then display these rows or columns as histograms of the data values. The user is then presented with a number of options which maybe selected by using the mouse or typing in the appropriate letter in the active graphics window.

A.3 Image Manipulation

NAME

`rotate`

SYNTAX

`rotate [file-name] [new-name]`

DESCRIPTION

Performs a number of relatively simple transformation to an image. The options are to either rotate the image clockwise or anti–clockwise by 90°, or mirror the image in the horizontal or vertical direction. A graphics window is opened in which a shaded contour plot of the image is displayed. The user is given a number of options as to how the image is to be transformed. Once the option is selected the program then proceeds to operate on the image and then display a shaded contour plot of the transformed image so that the user can verify that the transformation is the correct one.

NAME

`trim_image`

SYNTAX

`trim_image [x1] [y1] [x2] [y2] [image-name] [new-image]`

DESCRIPTION

Trims away unwanted sections of an image. **x1,y1** are the pixel coordinate of the lower left hand corner of the desired section. **x2,y2** are the pixel coordinate of the upper right hand corner of the desired section. The program retains only that part of the image inside the rectangle defined by **x1,y1** and **x2,y2**. The trimmed image replaces the original image if given the same name.

NAME

prepare_mask

SYNTAX

prepare_mask [image-file] [mask-file]

DESCRIPTION

Interactively flags bad pixels in image data and creates a mask file for use by the **correct_badpix** program. The program asks the user whether an existing mask file is to be modified if a name is not given for '**mask-file**'. If such a file exists the full path name must be given, else '**none**' is typed. Bad pixels are flagged by pointing using the mouse and type the character '**b**.' Clicking one of the mouse buttons enlarges the area under view. A small window in the top right hand corner opens to show the enlarged area. The bad pixels maybe flagged in this window by pointing and clicking using the mouse. To redraw the image putting in newly flagged pixels, '**r**' is typed while the cursor is in the graphics window. To correct any wrongly flagged pixel '**c**' is typed while pointing at it with the cursor. To end the program '**q**' is typed in the active graphics window. The grid of bad pixel flags is output to file '**mask.asc**.'

NAME

`correct_badpix`

SYNTAX

`correct_badpix [file-name] [new-name] [mask-file]`

DESCRIPTION

Replaces bad pixels in an image by an average value of the surrounding 3x3 grid of pixels. Using the mask file the program attempts to smooth over the flagged pixels. The mask file is created through the use of the previous command (**prepare_mask**). Given the position the program uses a 3x3 grid of pixels surrounding the bad one. It selects the unflagged pixels from the grid to work out an average value and assign the number to the flagged pixel.

A.4 Wavelength Calibration

NAME

`wavecal`

SYNTAX

`wavecal [file-name]`

DESCRIPTION

Performs wavelength calibration on a 2-D spectral image. The program asks the user to type in the reference wavelengths. End the input by typing in the number 999.999. The program then displays a shaded contour plot of the image and prompts the user to select a row to use for the wavelength calibration. A graph of the data is displayed and the program prompts for pairs of points (to be indicated using the mouse) defining the sides of the reference lines. Once all the reference lines have been identified the calibration is displayed and the choices are given to calibrate other rows or end the program there. At least four rows spanning the required region must have been used for the wavelength calibration before the program can interpolates the dispersions to other rows. The program ends by writing out the calculated wavelength scale to a file called '**wave.dat.**'

A.5 Interpolation

NAME

`extend_spectrum`

SYNTAX

`extend_spectrum [file-name] [new-name]`

DESCRIPTION

Extracts a spectrum from one part of an image and copies it into other parts of the same image. A shaded contour image of the data is displayed and the user asked to indicate rows in the image containing the spectrum. The user is then required to select the region into which the spectrum is to be copied by defining a pair of rows bracketing the desired region. An option is available to edit out spectral features. If this is selected then the user is required to give pairs of points bracketing the features to be edited out. The data points in between are discarded and replaced by a linear interpolation. The user may then go on to fit a second order polynomial to the remaining points. This option should not be used if the spectrum also contains instrumental functions which might be erased if such a fit is applied.

A.6 Black Body

NAME

`black_body`

SYNTAX

`black_body [file-name] [new-name]`

DESCRIPTION

Divide a blackbody function into a spectral image. A wavelength calibration (obtained through the use of **wavecal**) must be supplied by the user. The wavelength range must corresponds to that of the standard star. The program asks that a temperature be selected for the black body. The program also requires that the user defines a reference wavelength to which flux at other wavelength be normalised.

A.7 Fitting

NAME

`extract_background`

SYNTAX

`extract_background [file-name] [new-name]`

DESCRIPTION

Create a continuum file from a given image to use as an estimate of the continuum in the fitting. The program puts up a shaded contour plot of the given image and then prompt for rows to extract the continuum from. Select the rows by pointing and then clicking with the mouse. A graph of the data is display and features maybe *edited* out by indicating pairs of points bracketing the features. The data values between the two selected points are then discarded and replaced by a linear interpolation. A fourth order polynomial is fitted to the remaining data points and the results displayed. The user may go back and re-edit the spectrum if fitted polynomial does not accurately follow the continuum. To go on and extract the continuum from other rows position the pointer outside of the frame containing the graph and click using the mouse. A new image is created which maybe convolved with a normalised image of a standard to incorporate atmospheric absorption features into the continuum.

NAME

`prepare_weighting`

SYNTAX

`prepare_weighting [file-name] [weighting-file]`

DESCRIPTION

Assign arbitrary values to data points in a spectrum. Maybe used by the cgs4_fit program to weight the individual points in a spectrum when fitting. **file-name** is the name of the file containing a 1-D spectrum extracted from the relevant 2-D image (see **cgs4_fit**). A spectrum of the data is displayed in a graphics windows in which the program asks for pair of points between which the data points are to be set to a particular value. The user is then asked to give values to the desired points. The value 999.999 assigned to any point causes the fitting program to ignore it. Any other value sets the program to weight the data point by that value in the fit. This program is usually used to select irrelevant regions of the spectrum and tell the fitting program to ignore it in the fitting. Can save a significant amount of time if a large number of spectra are to be fitted.

NAME

`efit`

SYNTAX

`efit <return>`

DESCRIPTION

Change the files that the **cgs4_fit** program uses when fitting spectra. The first three lines give the names of files containing Einstein A–coefficients, energy levels and wavelength calibration. The next three indicate optional files that the program may use during the fitting. Lines 7 and 8 contain informations about the spectral image to be used. Line 9 directs the program where to look for the data set relevant to the fitting (an example of which can be seen in figure A.3).

NAME

cgs4_fit

SYNTAX

cgs4_fit [file-name]

DESCRIPTION

Extract a 1-D spectrum from a 2-D image and fit a theoretical H_3^+ spectrum to it. The program may perform either weighted or unweighted least squares fitting. An editor is started as part of the program so that various data values can be changed during the running of the program. Any of the model parameters maybe be fixed when fitting to a particular spectrum by changing the flag associated with it from 0 to 1. All changes must be saved before the program accepts the new values.

A shaded contour image of the data is displayed in a separate graphics window. The required row is selected by pointing the cursor at the desired area of the image and click one of the mouse buttons. End the selection process by typing '**q**' or '**Q**' while the cursor is positioned inside the graphics window. If the file containing estimates of the background is not available then the program asks for a data row to use as an estimate of the continuum level. Graph showing the fitted spectrum replaces the shaded contour image of the data. Options is then given to a) save the fitted spectrum to a file, b) estimate the range of uncertainties of the fitted parameters (only the temperature and column density are subjected to this), c) select other rows to fit or d) end the program. The initial and fitted values of the model parameters is written to a file called '**file-name.out.**'

A.8 Image Analysis

NAME

`mkpict[x]`

SYNTAX

```
mkpict
> [image-name] [xoffset] [yoffset]
> [image-name] [xoffset] [yoffset]
> q
```

DESCRIPTION

Program to plot the images given in "image-name" using colour shadings to represent the pixel intensity. The user is asked to specify a number of images each with their own "xoffset,yoffset" pairs of coordinates in arc seconds, relative to the center of the planet. The "xoffset, yoffset" must be the position of the center of the image. Each image file name must begin on a separate line. To end with entering image names give "q" as a file-name. The program goes on to ask what overall size of the image is to be. This is used to either enlarge a small part of the image or to view several images side by side and reposition them to put together a larger picture. It then asks the user to specify the pixel size, whether limb brightening correction is to be applied and whether the images are to be plotted quickly, resulting in poorer image quality, or slowly to achieve higher image quality. The program then asks where the user wish to place the center of the planet. This is specified in pixel coordinates, the lower left corner being the origin. The size of the overall pixel grid depends on the size of the overall image (in arc seconds) that the user specified to the program. Pressing return without typing any other character tells the program to accept the default coordinates and proceed to assign the images in the grid.

To plot the colour shaded image the user is asked to supply the lower and upper shading limits. Pressing the return key without typing any other character to accept the default values. Once the image has been displayed in a separate graphics window the user is offered a number of options. Type the option character while the cursor is in the graphics window to select that option.

If a grid of longitude and latitude is desired the program asks the user to give the name of a file containing the planetary parameters. Press return without typing any other character to accept the default file name if one is given. The program also asks for files containing the longitudes and latitudes to plot on the image. Each longitude to plot must be on a separate line file. The same applies to the latitude file.

If the feature option is selected the user will once again need to supply the name of the file containing th planetary parameters and also the name of the file containing the feature(s) coordinates this time in terms of longitude and latitude pairs (see A.2 for file format).

If other options are selected the user is prompted for answers according to the chosen option.

To get a quick description of the options type '**h**' while the cursor is in the graphics window. Additionally the user can examine the pixel value by pointing and clicking with the mouse.

The postscript file created when the hard copy output option is selected is given the file name '**POST**' by the program. To keep the postscript file rename the '**POST**' file to another name. The '**POST**' file is over written if the hard copy output option is selected again.

To change the relative positions of the individual image frames in the mosaic the user may edit the file '**file.list**' created by **mkpict** to contain the names of the images and their positions relative to the center of the planet. The changes must be saved before redrawing the picture.

The user may change the options specified on entry to the program by editing the '**data**' file. This file holds the data indicating the size of the picture to be plotted, pixel size, whether limb brightening correction is to be applied and how the picture should be plotted. Changes must be saved before re-plotting the picture.

The colour shading of the picture may be modified by simply specifying different upper and lower limits when re-plotting. A more complex way of changing the shading is to change the colour scale definition directly. The file '**cscale.dat**' created by the program contains a colour scale using the **RGB** scheme. The first line indicates how many points are defined in the scale, this must not exceed 8. The following lines (the number of which must match the number given in the first line) defined the step sizes and intensities of the red, green and blue colours respectively. The relative step sizes define how gradual the change in colour should be and can take any value between 0 and 100. The step size in the last line is ignore but is included for completeness and ease of array handling. The next three numbers define the relative colour intensities and can take any values between 0 and 100%. Table A.1 gives an example of my definition of the 'black body' colour scale.

	8			# Number of defined points in the colour
80.0	0.0	0.0	0.0	# scale.
15.0	0.0	0.0	0.0	#
30.0	10.0	0.0	0.0	#
30.0	50.0	10.0	0.0	# Step size, intensities of the red, green,
30.0	80.0	20.0	0.0	# blue colours.
20.0	100.0	40.0	0.0	#
30.0	100.0	80.0	0.0	#
20.0	100.0	100.0	20.0	#

Table A.1: Example of a colour scale defined using the **RGB** scheme. The colours go from black through orange to yellow.

1		# Number of features to plot.
16		# Number of points defined for this feature.
6.1901245	-68.10884094	#
29.18005180	-67.76689911	#
52.37763977	-66.69635010	#
72.45014191	-65.37580109	#
89.18093872	-65.16767120	#
104.6948624	-66.75817108	#
121.6789780	-69.94780731	# Longitude Latitude of point.
143.8666077	-73.98096466	#
176.4247894	-77.46322632	#
218.0062561	-78.51404572	#
255.0700226	-77.02860260	#
283.2577209	-74.48732758	#
305.9600525	-71.87845612	#
325.9905090	-69.77377319	#
345.4329834	-68.53733063	#
366.1901245	-68.10884094	#

Table A.2: Example of file containing coordinates defining features on the surface of Jupiter. This file defined points on the northern and southern footprint of the last closed field line (L=30 shell).

AIFFIL=h3paif3.533	#	Einstein A-coefficients.
LEVELS=h3plevels	#	Energies of the H_3^+ levels.
BAKFIL=jred_22_dbs_bak	#	Continuum estimate.
ERRFIL=none	#	Error file.
WGTFIL=jred_22_dbs_wt	#	Weightings of data points.
CML=102	#	The CML of the 2-D spectrum.
FILNUM=22	#	Observation file number.
DATFIL=jred_22_dbs.data	#	Relevant data.
WAVFIL=cgs4_3533_wave.dat	#	Wavelength calibration file.
FILE=jred_22_dbs	#	The 2-D spectrum.
ASCDIR=$HOME/03may93	#	Directory where the 2-D spectrum is located.
PARDIR=.	#	Directory where the h3paif3.533 and h3plevels are located.
FITMOD=ls	#	Method of fitting.
LSCORR=y	#	Apply limb brightening correction?

Table A.3: Example showing the format of the file used by efit.